Functional pulmonary MRI with ultra-fast steady-state free precession

INAUGURALDISSERTATION

zur

Erlangung der Würde eines Doktors der Philosophie

vorgelegt der

Philosophisch-Naturwissenschaftlichen Fakultät

der Universität Basel

von

Orso Andrea Pusterla

aus Breggia TI

Basel, 2018

Genehmigt von der Philosophisch-Naturwissenschaftlichen Fakultät
auf Antrag von

Prof. Dr. Bernd Krusche
Fakultätsverantwortlicher

Prof. Dr. Oliver Bieri
Dissertationsleiter

Prof. Dr. Matthias Stuber
Korreferent

Basel, den 22. Mai 2018

Prof. Dr. Martin Spiess
Dekan

"*I am just a child who has never grown up.*
I still keep asking these 'how' and 'why' questions.
Occasionally, I find an answer."
Stephen Hawking, physicist, Jan. 8 1942 – Mar. 14 2018

To my family and my dear friends.

Abstract

To date, computed tomography and nuclear medicine techniques are still the reference standard for lung imaging, but radiation exposure is a major concern; especially in case of longitudinal examinations and in children. Therefore, radiation-free imaging is an urgent necessity. Pulmonary magnetic resonance imaging (MRI) is radiation-free, but poses challenges since the low proton density and the presence of strong mesoscopic susceptibility variations considerably reduce the detectable MR signal. As a result, the lung typically appears as a "black hole" with conventional MRI techniques. Recently, ultra-fast balanced steady-state free precession (ufSSFP) methods were proposed for ameliorated lung morphological imaging. In this thesis, ufSSFP is employed to develop and improve several pulmonary functional imaging methods, which can be used in clinical settings using standard MR scanners and equipment.

At every breath, the lung expands and contracts, and at every heartbeat, the blood is pumped through the arteries to reach the lung parenchyma. This creates signal modulations associated with pulmonary blood perfusion and ventilation that are detectable by MRI. The second chapter of this thesis focuses on the optimization of time-resolved two-dimensional (2D) ufSSFP for perfusion-weighted and ventilation-weighted imaging of the lung. Subsequently, in the third chapter, three-dimensional (3D) multi-volumetric ufSSFP breath-hold imaging is used to develop a lung model and retrieve the measure α, a novel ventilation-weighted quantitative parameter.

Oxygen-enhanced MRI exploits the paramagnetic properties of oxygen dissolved in the blood, acting as a weak T_1-shortening contrast agent. When breathing pure oxygen, it reaches only ventilated alveoli of the parenchyma and dissolves only in functional and perfused regions. How ufSSFP imaging in combination with a lung model can be used to calculate robust 3D oxygen enhancement maps is described in the fourth chapter. In addition, in the fifth chapter, 2D inversion recovery ufSSFP imaging is employed to map the T_1 and T_2 relaxation times of the lung, the change of the relaxation times after hyperoxic conditions, as well as the physiological oxygen wash-in and wash-out time (related to the time needed to shorten T_1 after oxygen breathing).

The objective of the last chapter of this thesis is the application of 3D ufSSFP imaging before and after intravenous gadolinium-based contrast agent administration for the investigation of signal enhancement ratio (SER) mapping: a rapid technique to visualize perfusion-related diseases of the lung parenchyma.

The techniques presented in this thesis using optimized ufSSFP pulse sequences demonstrated potential to reveal new insights on pulmonary function as well as quantification, and might become part of the future standard for the evaluation and follow-up of several lung pathologies.

List of publications

Journal papers

- **Pusterla O***, Bauman G*, Bieri O. *Ultra-fast Steady-State Free Precession Pulse Sequence for Fourier Decomposition Pulmonary MRI.* Magn Reson Med, 2015, 75:1647-53. *Equally contributed to this work.

- **Pusterla O**, Bauman G, Wielpütz MO, Nyilas S, Latzin P, Heussel CP, Bieri O. *Rapid 3D in vivo ^{1}H human lung respiratory imaging at 1.5 T using ultra-fast balanced steady-state free precession.* Magn Reson Med, 2017, 78:1059–1069.

- Bauman G, Santini F, **Pusterla O**, Bieri O. *Pulmonary relaxometry with inversion recovery ultra-fast steady-state free precession at 1.5T*. Magn Reson Med, 2017, 77(1):74-82.

- Nyilas S, Bauman G, Sommer G, Stranzinger E, **Pusterla O**, Frey U, Korten I, Singer F, Casaulta C, Bieri O, Latzin P. *Novel Magnetic Resonance Technique for Functional Imaging Of Cystic Fibrosis Lung Disease*. Eur Respir J 2017, 50 (6) 1701464.

- **Pusterla O**, Bauman G, Bieri O. *Three-dimensional oxygen-enhanced MRI of the human lung at 1.5T with ultra-fast balanced steady-state free precession.* Magn Reson Med, 2018, 79:246–255.

- **Pusterla O***, Bauman G*, Santini F, Bieri O. *Dynamic and steady-state oxygen-dependent lung relaxometry using inversion recovery ultra-fast steady-state free precession imaging at 1.5 T.* Magn Reson Med, 2018, 79:839–845. *Equally contributed to this work.

- **Pusterla O***, Sommer G*, Wiese M, Lardinois D, Tamm M, Bremerich J, Santini F, Bauman G, Bieri O. *Signal enhancement ratio imaging of the lung parenchyma with ultra-fast steady-state free precession MRI at 1.5T.* J Magn Reson Imaging, 2018, DOI: 10.1002/jmri.25928 (Epub ahead of print). *Equally contributed to this work.

- Nyilas S, Bauman G, Sommer G, **Pusterla O**, Singer F, Heyer C, Schlegtendal A, Benzrath S, Casaulta C, Bieri O, Koerner- Rettberg C, Latzin P. *Pattern of Airway pathology in PCD: Assessment with MRI and lung function.* Article submitted to White Ann Am Thorac Soc, Feb 2018.

- Bauman G, **Pusterla O**, Bieri O. *Functional lung imaging with partially-spoiled ultra-fast steady-state free precession.* Article submitted to Magn Reson Med, March 2018.

- Nyilas S, Bauman G, **Pusterla O**, Stranzinger E, Ramsey K, Singer F, Yammine S, Casaulta C, Bieri O, Latzin P. *Ventilation and perfusion assessed by functional MRI in children with CF: reproducibility in comparison to lung function.* Article submitted to J Cyst Fibros, March 2018.

Patent application

- **Pusterla O**, Bauman G, Bieri O. Assessment of the lung parenchyma by means of magnetic resonance images (U.S. patent application 2018/0055414, issued Mar. 1, 2018).

Conference proceedings (peer-reviewed)

- **Pusterla O**, Bauman G, Sommer G, Bieri O. *How volume affects the pulmonary MRI signal: Investigations with 3D ultra-fast balanced Steady-State Free Precession.* Proceedings of the 23rd Annual Meeting of the ISMRM, Toronto, Canada, 2015:1481. Traditional poster.

- **Pusterla O**, Bauman G, Sommer G, Jud C, Cattin PC, Bieri O. *Three- dimensional oxygen-enhanced human lung MRI using ultra-fast balanced steady-state free precession.* Proceedings of the 23rd Annual Meeting of the ISMRM, Toronto, Canada, 2015:3978. Electronic poster.

- **Pusterla O**, Santini F, Heule R, Bieri O. T_2*-Snapshots imaging with simultaneous multislice TESS acquisition.* Proceedings of the 23rd Annual Meeting of the ISMRM, Toronto, Canada, 2015:0441. Talk.

- Bauman G, **Pusterla O**, Bieri O. *Ultra-Fast Steady-State Free Precession Pulse Sequence for Pulmonary Fourier Decomposition MRI*. Proceedings of the 23rd Annual Meeting of the ISMRM, Toronto, Canada, 2015:1456. Traditional poster.

- **Pusterla O**, Bauman G, Bieri O. *Balanced SSFP pulmonary signal enhancement after contrast agent injection.* Proceedings of the 24th annual meeting of the ISMRM, Singapore. 2016:2916. Electronic poster (ISMRM merit award – magna cum laude).

- **Pusterla O**, Bauman G, Wielpütz MO, Heussel CP, Bieri O. *Fast 3D quantitative ^{1}H ventilation imaging of the human lung at 1.5T with SSFP.* Proceedings of the 24th annual meeting of the ISMRM, Singapore. 2016:2917. Electronic poster (ISMRM merit award – magna cum laude).

- Bauman G, Nyilas S, **Pusterla O**, Heyer C, Koerner-Rettberg C, Latzin P, Bieri O. *Pulmonary Fourier Decomposition MRI Compared to Multiple Breath Washout and Spirometry: A Preliminary Study in Primary Ciliary Dyskinesia*. Proceedings of the 24th annual meeting of the ISMRM, Singapore. 2016:2924. Electronic poster.

- Weigel M, **Pusterla O**, Gloor M, Bieri O. *Towards Tissue Characterization of the Spinal Cord: High-Resolution* T_1 *Relaxometry with Precise B1+-Mapping of the Spinal Cord at 3T*. Proceedings of the 24th annual meeting of the ISMRM, Singapore. 2016:4411. Electronic poster.

- **Pusterla O**, Bauman G, Nyilas S, Madörin P, Jung B, Ith M, Stranzinger E, Frey U, Latzin P, Bieri O. *Respiratory α-Mapping of Cystic Fibrosis at 1.5T.* Proceedings of the 25th annual meeting of the ISMRM, Honolulu, HI, USA. 2017:0118. Talk at power pitch session (ISMRM merit award – summa cum laude).

- **Pusterla O**, Sommer G, Wiese M, Lardinois D, Tamm M, Bremerich J, Santini F, Bauman G, Bieri O. *Ultra-Fast Balanced SSFP Signal Enhancement Ratio Mapping of the Human Lung Parenchyma at 1.5T.* Proceedings of the 25th annual meeting of the ISMRM, Honolulu, HI, USA. 2017:4906. Electronic poster.

- **Pusterla O**, Bauman G, Bieri O. *Free-Breathing Multi-Slice Ultra-Fast SSFP Acquisitions for Multi-Volumetric Morphological and Functional Lung Imaging.* Proceedings of the 25th annual meeting of the ISMRM, Honolulu, HI, USA. 2017:4907. Electronic poster.

- Bauman G, Santini F, **Pusterla O**, Bieri O. *Oxygen-Enhanced Pulmonary Relaxometry Using Ultra-Fast Steady-State Free Precession Imaging*. Proceedings of the 25th annual meeting of the ISMRM, Honolulu, HI, USA. 2017:1187. Talk.

- Bauman G, Nyilas S, **Pusterla O**, Haas T, Ith M, Jung B, Casaulta C, Sommer G, Stranzinger E, Frey U, Latzin P, Bieri O. *Functional Lung MRI Using Matrix Pencil Decomposition and N2 Multiple-Breath Washout Measurements in Cystic Fibrosis*. Proceedings of the 25th annual meeting of the ISMRM, Honolulu, HI, USA. 2017:0827. Talk.

- Sommer G, **Pusterla O**, Wiese M, Santini F, Lardinois D, Bremerich J, Bauman G, Bieri O. *Assessment of contrast-enhancement in the lung parenchyma using 3D ultra-fast steady-state free precession MRI*. Proceedings of the European Congress of Radiology (ECR), Vienna, Austria, 2017; B-1083. Talk.

- Nyilas S, Bauman G, Sommer G, **Pusterla O**, Singer F, Bieri O, Heyer C, Koerner-Rettberg C, Latzin P. *Functional magnetic resonance imaging compared to lung function in primary ciliary dyskinesia*. Proceedings of the European Congress of Radiology (ECR), Vienna, Austria, 2017; B-0156. Talk.

- Sommer G, **Pusterla O**, Wiese M, Lardinois D, Tamm M, Bremerich J, Santini F, Bauman G, Bieri O. *Pulmonary signal enhancement ratio mapping at 1.5T using 3D ultra-fast balanced steady-state free precession MRI*. Proceedings of the Swiss Congress of Radiology (SCR), Bern, 2017; SS115. Talk.

- Nyilas S, Bauman G, Sommer G, Stranzinger E, **Pusterla O**, Frey U, Korten I, Singer F, Casaulta C, Bieri O, Latzin P. *Novel magnetic resonance technique for functional imaging of cystic fibrosis lung disease*. Proceedings of the Swiss Congress of Radiology (SCR), Bern, 2017; P064. Talk.

- **Pusterla O**, Andermatt S, Bauman G, Nyilas S, Madörin P, Haas T, Pezold S, Santini F, Latzin P, Cattin P, Bieri O. *Deep Learning Lung Segmentation in Paediatric Patients.* Proceedings of the 26th annual meeting of the ISMRM, Paris, France. 2018:4355. Traditional poster.

- Bauman G, **Pusterla O**, Bieri O. *Functional lung imaging with partially spoiled ultra-fast steady-state free precession at 1.5T and 3T.* Proceedings of the 26th annual meeting of the ISMRM, Paris, France. 2018:4346. Electronic poster.

- Bauman G, Nyilas S, **Pusterla O**, Stranzinger E, Ramsey K, Singer F, Yammine S, Casaulta C, Latzin P, Bieri O. *Repeatability of ventilation and perfusion impairment assessed with matrix pencil decomposition MRI and lung function in children with cystic fibrosis.* Proceedings of the 26th annual meeting of the ISMRM, Paris, France. 2018:1078. Talk.

- Bauman G, Nyilas S, **Pusterla O**, Stranzinger E, Ramsey K, Singer F, Yammine S, Casaulta C, Latzin P, Bieri O. *Repeatability of ventilation and perfusion impairment assessed with matrix pencil decomposition MRI and lung function in children with cystic fibrosis*. Proceedings of the Swiss Congress of Radiology (SCR), Lausanne, 2018; P135. Talk.

Contents

1 Introduction **1**

1.1 An improved respiratory medicine thanks to lung MRI **3**

1.2 The human lung **6**

1.2.1 Anatomy 6

1.2.2 Pulmonary circulatory system 10

1.3 Physiology of the lung **11**

1.3.1 Ventilation and gas diffusion 11

1.3.2 Perfusion 11

1.3.3 Regional distribution of pulmonary ventilation and perfusion 12

1.3.4 Ventilation-perfusion ratio in the lung 12

1.4 Pulmonary disorders **13**

1.5 What do we wish to measure? **14**

1.6 The challenges of lung MRI **15**

1.7 What lung MRI offers **16**

1.7.1 Morphological imaging 16

1.7.1.1 Clinical protocols 16

1.7.1.2 Ultra-short echo time 17

1.7.2 Pulmonary relaxometry 18

1.7.3 Functional imaging 19

1.7.3.1 Dynamic contrast-enhanced MRI 19

1.7.3.2 Oxygen-enhanced MRI 19

1.7.3.3 Fourier decomposition MRI 20

1.8 Imaging with balanced steady-state free precession **21**

1.9 Balanced-SSFP with minimal TR: ultra-fast SSFP **24**

1.10 Aim of the thesis **25**

1.11 Outline of the thesis **27**

2 Ultra-fast steady-state free precession pulse sequence for Fourier decomposition pulmonary MRI 29

2.1 Introduction 31

2.2 Methods 32

2.2.1 Adaptation and optimization of ufSSFP for FD-MRI 32

2.2.2 MRI data acquisitions 33

2.2.3 Image post-processing and analysis 34

2.3 Results 34

2.4 Discussion 39

2.5 Conclusion 40

3 Rapid three-dimensional in vivo ^{1}H human lung respiratory imaging at 1.5T using ultra-fast balanced steady-state free precession 41

3.1 Introduction 43

3.2 Theory 44

3.2.1 The adapted sponge model and the respiratory α-index 44

3.2.2 The respiratory α-index: theoretical formulation and interpretation 45

3.3 Methods 48

3.3.1 MRI data acquisition 48

3.3.2 The adapted sponge model 48

3.3.3 Respiratory α-mapping 49

3.3.4 Reproducibility 50

3.4 Results 50

3.4.1 Validation of the adapted sponge model 50

3.4.2 Respiratory α-mapping in healthy subjects 52

3.4.3 Respiratory α-mapping in patients 55

3.5 Discussion 58

3.6 Conclusions 61

A3 Respiratory α-mapping of cystic fibrosis at 1.5T 63

A3.1 Purpose 64

A3.2 Materials and methods 64

A3.2.1 Theory 64

A3.2.2 Subjects and measurement protocol 65
A3.2.3 Image post-processing and analysis 66
A3.3 Results 67
A3.4 Discussion 68

4 Three-dimensional oxygen-enhanced MRI of the human lung at 1.5T with ultra-fast balanced steady-state free precession 69
4.1 Introduction 71
4.2 Methods 72
4.2.1 Oxygen-related signal enhancement for balanced SSFP 72
4.2.2 Respiratory-related signal modulation in bSSFP - The sponge model 73
4.2.3 Calculation of oxygen-enhancement maps from the sponge model 73
4.2.4 Imaging 74
4.2.5 Flip angle optimization 74
4.2.6 Signal intensity variability at functional residual capacity 74
4.2.7 OE-MRI using the sponge model 75
4.3 Results 78
4.3.1 Flip angle optimization 78
4.3.2 Signal intensity variability at functional residual capacity 79
4.3.3 OE-MRI using the sponge model 80
4.4 Discussion 85
4.5 Conclusions 86

5 Dynamic and steady-state oxygen-dependent lung relaxometry using inversion recovery ultra-fast SSFP imaging at 1.5T 87
5.1 Introduction 89
5.2 Methods 90
5.2.1 Pulmonary relaxometry with IR-ufSSFP 90
5.2.2 Imaging procedure 90
5.2.3 Generation of the parameter maps 92
5.2.4 T_1-related oxygen wash-in and wash-out time constants 92
5.2.5 Image analysis 93
5.3 Results 93

5.4 Discussion **97**

5.5 Conclusion **99**

6 Signal enhancement ratio imaging of the lung parenchyma with ultra-fast steady-state free precession MRI at 1.5T **101**

6.1 Introduction **103**

6.2 Methods **104**

6.2.1 Study subjects 104

6.2.2 MR imaging 105

6.2.3 SPECT/CT 105

6.2.4 MR image post-processing 106

6.2.5 Visual and quantitative data analysis 107

6.3 Results **109**

6.3.1 Signal enhancement in the control group 109

6.3.2 Signal enhancement in pathologic lung tissue 115

6.4 Discussion **119**

6.5 Conclusion **121**

7 Summary and outlook **123**

7.1 Summary **125**

7.2 Future work **128**

7.2.1 Implementation of new acquisition schemes 128

7.2.2 Clinical evaluation and validation 129

7.2.3 Quantification and automatization 130

7.3 Conclusion **131**

References **133**

Acknowledgments **149**

Curriculum Vitae **153**

CHAPTER 1

Introduction

1.1 An improved respiratory medicine thanks to lung MRI

Pulmonary diseases are among the leading causes of morbidity and mortality worldwide [1, 2]. The lung has a delicate structure and limited regenerative capacity [3], and consequently, early diagnosis, illness quantification, and follow-up examinations play a pivotal role in patient management as well as interventions to avoid life-long alterations [2, 4, 5].

A medical examination combined with lung stethoscope auscultation is the first and simplest diagnostic method to evaluate morpho-functional alterations of the thorax [6]. Pulmonary function tests (PFTs) such as spirometry, plethysmography, and multiple-breath washout measurements provide a global measure of the lung disease severity and progression [7]. The strength of the PFTs relies on their low costs and the standardization of normative results (e.g., gender, body size, age) [8]. However, PTFs are highly effort-dependent and can therefore not be performed in young children (e.g., < 5 years old), creating a diagnostic gap within this age group [9]. Furthermore, the diagnostic value of PFTs and stethoscope auscultation is limited as they are not able to give any insight on exact morphological alterations and do not provide quantification of regional lung function or pathophysiological mechanisms [10, 11]. In addition, these techniques are often not sensitive enough to detect the disease in its early stages [12–14], limiting opportunities for personalized and targeted interventions which are the cornerstones for a successful modern respiratory medicine.

To overcome these limitations, several imaging modalities have been developed for the non-invasive assessment of lung morphology and function. Currently, the clinical gold standard methods for morphological investigations are chest X-ray and three-dimensional (3D) computed tomography (CT) [15, 16]. X-ray examinations offer planar images with a low radiation dose delivered to the body, while CT, at the cost of higher radiation, allows electron density weighted 3D imaging up to an isotropic resolution of about 0.3 mm.

For functional measurements of the lung, nuclear medicine modalities are regarded as a clinical gold standard: single-photon emission computed tomography (SPECT) for pulmonary perfusion and ventilation assessment, planar scintigraphy for ventilation, and positron emission tomography (PET) for metabolic tissue imaging [5, 16–20]. These techniques are based on radioactive nuclides intravenously injected or inhaled (e.g., macroaggregates or aerosols labelled with ^{99m}Tc, ^{81m}Kr, ^{133}Xe, ^{18}F), have a relatively low spatial and temporal resolution, and difficulties to obtain quantitative outcomes [21]. Figure 1.1 shows representative imagines of the chest obtained with X-ray, CT, and SPECT/CT.

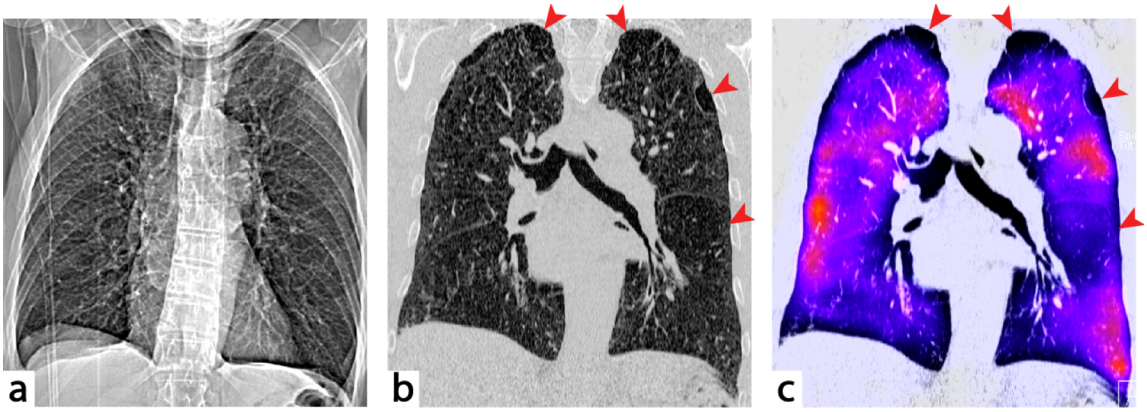

Figure 1.1. X-ray (a), CT (b), and SPECT/CT (c) in a patient with chronic obstructive pulmonary disease (COPD). Emphysema and bullae are indicated by the arrowheads.

Even though nuclear medicine and CT scientists have invested continuously significant effort in reducing radiation doses, any exposure to ionizing particles is still of concern [22–24]; especially for children and pregnant women. Furthermore, for patients who require frequent follow-up examinations for monitoring the disease progression and the response to therapeutic procedures (e.g., pharmacological treatments and targeted physiotherapy), the cumulative radiation dose would be a hazard [25].

A viable solution is offered by magnetic resonance imaging (MRI), which does not involve any harmful ionizing-radiation but employs strong electromagnetic fields and radiofrequency pulses. MRI is categorized as safe and is unlikely to have biological effects or to be genotoxic [26, 27]. For this reason, MRI is well suited for long-term structural as well as functional monitoring of lung pathologies [4, 28–33]. It has the potential to accelerate targeted interventions, thus preventing severe pulmonary disease exacerbation and permanent alterations (e.g., atelectasis) that might impair the life of patients and adversely affect the growth and development of the lung in children.

In contrast to CT where the measured signal intensity is proportional to electron density, in proton MRI, the signal is generated by the density and magnetic properties of hydrogen nuclei (^{1}H) in the tissues, i.e., spin-spin (T_2) or spin-lattice (T_1) relaxation times. These parameters lead to a large variety of contrasts, theoretically improving the distinctions of various soft tissues compared to CT. Furthermore, with MRI, higher spatial and temporal resolutions are reached compared to nuclear medicine imaging techniques, offering quantitative insights on rapid functional changes and physiology [4, 28–33].

Until recently, however, the application of proton MRI to study lung anatomy and function was limited due to technical imaging difficulties arising from the unique biophysical characteristics of the lung [28, 29, 34]. The pulmonary parenchyma is primarily composed of blood vessels and alveoli, creating a sponge-like structure, mainly filled with air, and thus characterized by a proton density that is 5 to 20 times lower compared to other human organs. Furthermore, the sponge-like structure of the parenchyma contains macroscopic and microscopic air cavities (e.g., bronchial tree and alveoli) as well as dense regions of lung tissue and vessels. These air-tissue and air-water interfaces create high susceptibility differences which lead to intravoxel phase dispersion of spins and a rapid MR signal decay, challenging MRI. Lung imaging is further complicated by the continuous respiratory and cardiac motion, blood flow, and pulsation; impairing image quality. For these reasons, the lung typically appears as a "black hole" with conventional proton MRI [28] as evident from Figure 1.2a. As a result, non-proton based MRI with inhaled hyperpolarized gaseous tracers (e.g., ^{3}He, ^{129}Xe, ^{19}F) was proposed and has demonstrated the ability to measure various pulmonary functional biomarkers [11, 35–41]. However, as it requires specific equipment and trained personnel, broad clinical application of hyperpolarized gas MRI is not feasible.

In the last decade, dedicated and optimized pulse sequences have significantly improved proton MRI of the lung [4, 28, 29], which nowadays is broadly available. Recently, rapid acquisition techniques with very short echo time (TE) or repetition time (TR), such as ultra-short echo time (UTE) and ultra-fast steady-state free precession (ufSSFP) pulse sequences have shown promise to tackle present limitations of imaging the pulmonary parenchyma and lung structures [42–47]. The speed of these techniques is further driven by optimized data acquisition trajectories combined with multichannel phased array coils for parallel imaging [48–50]. Specifically, a short echo time for UTE or a short repetition time for ufSSFP, combined with parallel imaging and specific acquisition trajectories, reduces the acquisition time while increasing the detected spin signal, mitigating motion-related artifacts, and allowing for higher temporal and spatial resolution. Representative UTE and ufSSFP images are shown in Figure 1.2.

Nowadays, thanks to the continuous commitment of scientists and advances in pulmonary MRI, various methods have been developed to explore the lung morphology, the tissue characteristics, and function [4, 28–33, 40, 41, 46, 47, 51]. Importantly, to date, these novel MR methods are investigated in patients, allowing for new insights on pathophysiological processes and targeted therapy, as well as longitudinal monitoring of the disease and treatments outcome [14, 33, 47, 52–56]. Lung MRI is laying fundamental building blocks for a successful modern respiratory medicine.

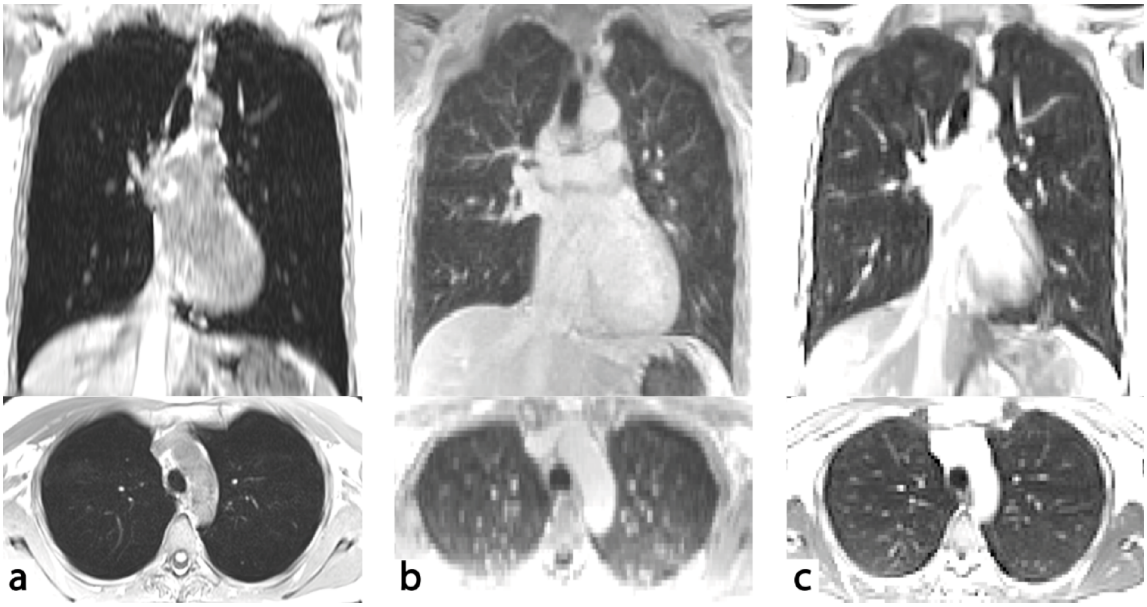

Figure 1.2. MRI of a healthy subject. In (a), a gradient echo sequence with long TE is used for imaging resulting in a very weak pulmonary tissue signal such that the lung appears as a "black hole". UTE [43] (b) and ufSSFP [45] (c) imaging allow capturing the signal of the pulmonary tissue.

1.2 The human lung

1.2.1 Anatomy

The respiratory apparatus comprises all the organs involved in breathing, and its cardinal function is to ensure a balanced blood oxygenation and removal of carbon dioxide (CO_2) produced by the cellular respiration [8, 57–59]. The respiratory system, as exemplarily shown in Figure 1.3, is divided into an upper and lower tract. The upper tract includes the nose, nasal passage, sinuses, pharynx, and a portion of the larynx above the vocal cords; the lower tract include the larynx (below the vocal cords), trachea, bronchi, bronchioles, terminal bronchioles, respiratory bronchioles, alveolar ducts, and alveolar sacs. Alveolar sacs contain a collection of alveoli, densely surrounded by blood capillaries in which the gas exchange takes place by diffusion. The lower respiratory tract is lined with the respiratory epithelium. This ciliated epithelium, covered by mucus secreted by mucous glands and by the bronchial walls, removes endogenous particles (e.g., dust, bacteria) from the lung thanks to the movement of the cilia.

Humans have two lungs that are embedded in the thorax. The lung comprises bronchi, bronchioles, terminal bronchioles, respiratory bronchioles, alveolar ducts, alveoli, blood vessels, and

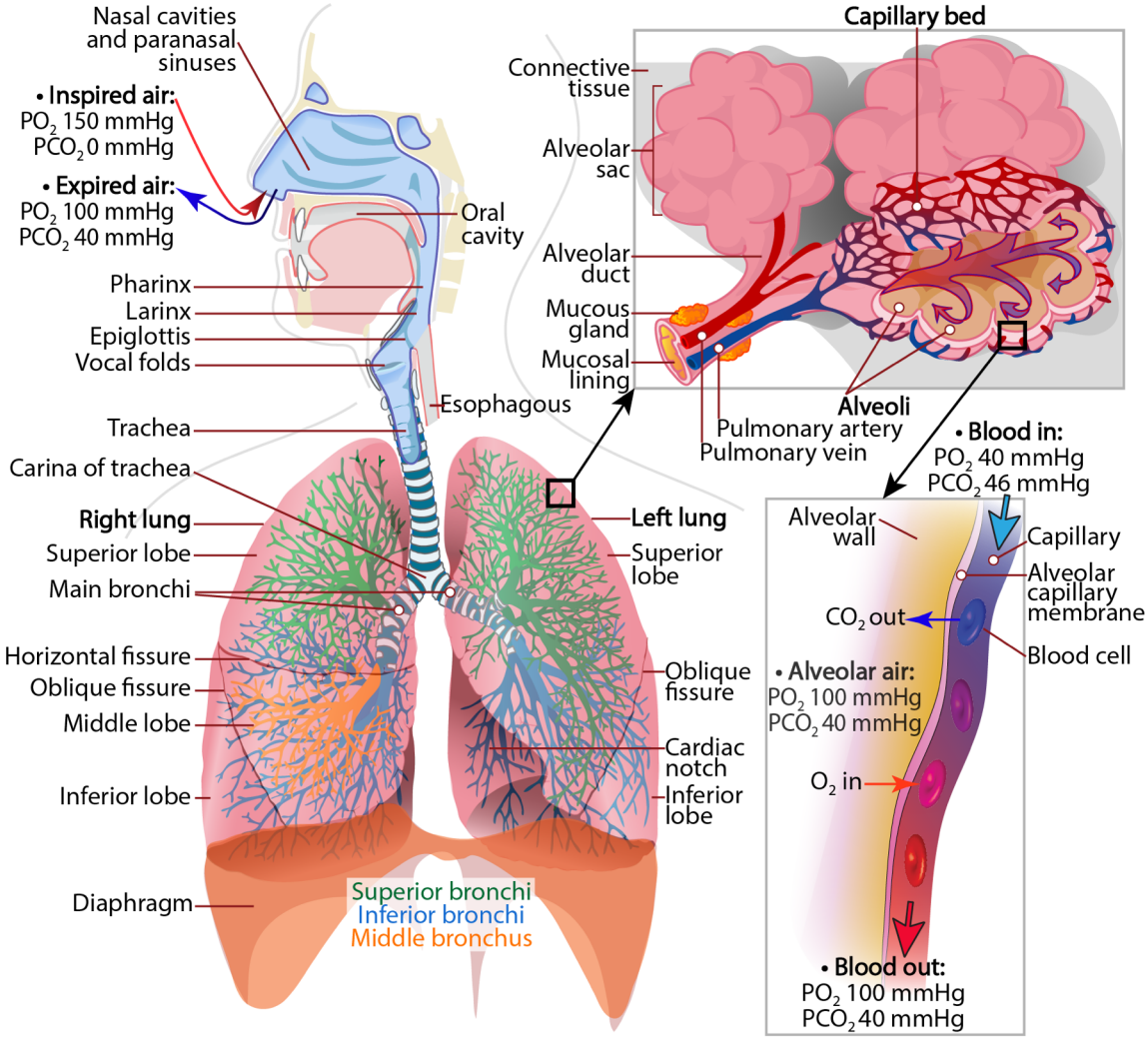

Figure 1.3. Left: schematic of the respiratory system. Top right: acinus region and a cutaway of the alveoli. Bottom right: gas exchange by diffusion through the alveolar-capillary membrane. To note the different partial pressures of O_2 and CO_2 in the inspired / expired air (top left), in the alveolar air, and arterial / venous capillaries (bottom right). Adapted from [60] (licensed under Creative Commons).

pulmonary interstitium. The pulmonary interstitium is a collection of connective tissues within the lung that includes the alveolar epithelium, pulmonary capillary endothelium, basement membrane, perivascular and perilymphatic tissues. The lung parenchyma consists of mixed structures involved in the gas transfer, such as respiratory bronchioles, alveolar ducts, alveoli, blood vessels, and pulmonary interstitium.

Both lungs are covered by a visceral pleura; the interstitium between the visceral pleurae and the parietal pleura attached to the thoracic cavity is filled with lubricant serous fluids to increase the sliding of the lung inside the thorax during respiration. The visceral pleura covers the lungs

and divides the right lung into three lobes, and the left lung into two lobes. The pleural separations between the lobes are known as fissures (see Fig. 1.3). The lobes are supplied by secondary bronchi. The lobes are further divided into segments defined as the lung regions supplied by any tertiary bronchus. The right lung is divided into 10 segments, and the left into 8-9 segments (i.e., depending on the subject, two segments might result fused together). The segments are subdivided into pulmonary lobules, defined as the most distal lung units served by the respiratory bronchioles.

The tracheobronchial tree is an intricate system that transports gases from the trachea to the alveoli, as illustrated in Figure 1.4. It is divided into 23 generations of dichotomous branching, from the trachea (generation 0) to the alveolar sacs (generation 23). The initial 16 generations, (bronchi to terminal bronchioles) form the conducting zone of the airways that transport gases from and to the exterior. The remaining 7 generations (respiratory bronchioles to alveolar sacs) form the respiratory zone, where the gas exchange takes place [57, 59, 61–63].

The tree structure of the lung allows increasing the number of the alveoli considerably and therefore the gas exchange surface (cf. Fig. 1.4). The human lung has almost 300-500 million alveoli, which make the lung appear like a sponge. The total area of the alveolar wall is about 70-140 m^2 (similarly to the size of a tennis court). The alveoli have a diameter of about 0.1-0.3 mm (Fig. 1.4d) and are densely surrounded by capillaries of ca. 7-10 µm in diameter (Fig. 1.4e). The capillaries have a similar size to a red blood cell, ca. 6-8 µm (cf. Fig 1.4e). Alveolar air and capillary blood are separated only by the alveolar epithelium and capillary endothelium, which form a 0.5 µm thin wall (known as alveolar-capillary membrane) that allows the gas exchanges (cf. Fig. 1.4e).

The lung tissue has a total mass of about 500 g, and its density is about 0.25-0.1 g/cm^3, depending on the respiratory phase (i.e., lung volume for a specific inspiratory level). In contrast, other human tissues and organs have a density of about 1 g/cm^3.

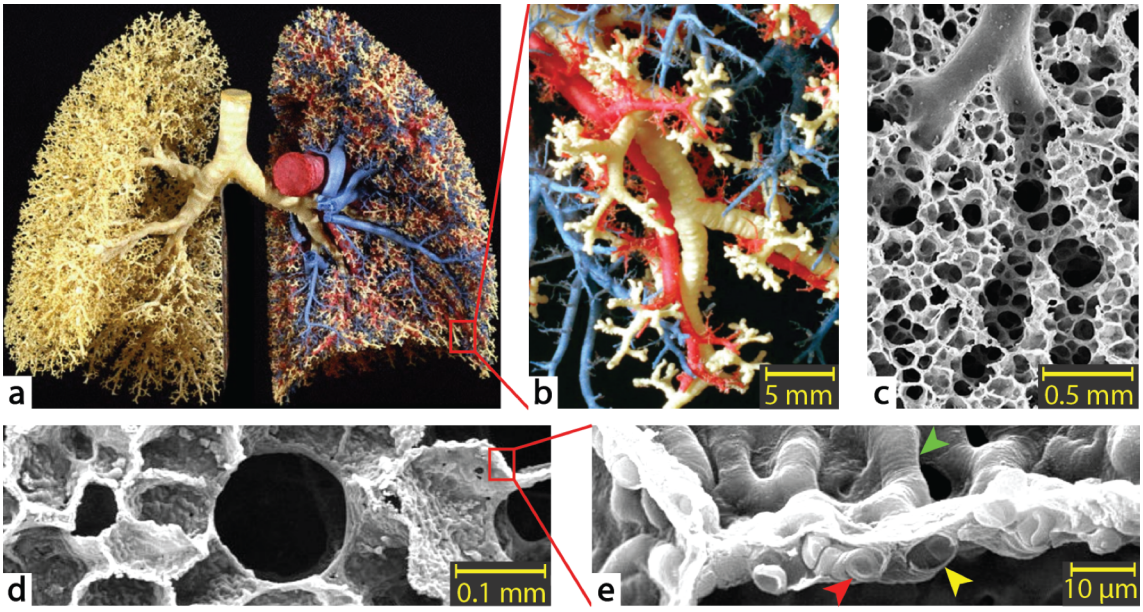

	Name of branches	Generation	# of tubes	Diameter [mm]	Cross sectional area [cm²]
Conducting zone	Trachea	0	1	15-22	2.5
	Primary bronchi	1	2	10-15	
	Sec. bronchi	2	4	10	
		3	8		
		4	16		
	Bronchioles	5	32		
	Terminal bronchioles	16	$6{\cdot}10^4$	1	100
Respiratory zone	Respiratory bronchioles	17 – 19	$5{\cdot}10^5$	0.6	10^3
	Alveolar ducts	20 – 22			
	Alveolar sacs	23	$8{\cdot}10^6$	0.4	$5{\cdot}10^4$
	Alveoli	–	$3\text{-}5{\cdot}10^8$	0.1-0.3	$7\text{-}14{\cdot}10^6$

f

Figure 1.4. (a) Cast of the human lung revealing the complexity of the bronchial and circulatory system. (b) A close-up of the distal arteries (red) and veins (blue) that are closely attached to the airways (yellow). (c) Electron microscope scan showing small respiratory bronchioles and alveoli. (d) A zoom-in of the alveolar duct surrounded by alveoli. (e) A further zoom-in of the alveolar wall composed primarily by blood capillaries (tubular structures as marked by the green arrowhead); air and blood are separated by the very thin alveolar-capillary membrane (yellow arrowhead), allowing gas diffusion; a red blood cell in a capillary is indicated by the red arrowhead. (f) Schematic of the airway branching according to the model of Weibel [62] and approximate dimensions of the respective structures. (a-e) and (f) are adapted from [63] (licensed under Creative Commons) and [59], respectively.

1.2.2 Pulmonary circulatory system

The blood flow in the lung is supplied by both the pulmonary and bronchial circulation. The pulmonary circulation is responsible for the blood re-oxygenation. The deoxygenated blood in return from the body (systemic circulation), is pumped by the right ventricle into the pulmonary arteries. Similarly to the tracheobronchial tree, the arteries branch off until the respiratory bronchioles. The blood then passes through the dense network of the capillary bed that lies in the wall of the alveoli, where it gets oxygenated, to finally flow back to the left atrium via the pulmonary veins. An illustration of the lung anatomy with a depiction of the main pulmonary vessels is shown in Figure 1.5. The bronchial circulation nourishes the lung tissue. A part of the oxygenated blood from the aorta passes through the bronchial arteries to supply the bronchi and the pulmonary parenchymal connective tissue. The majority of the deoxygenated blood of the bronchial circulation returns directly into the pulmonary vein, and a part returns via the bronchial veins to the circulatory system.

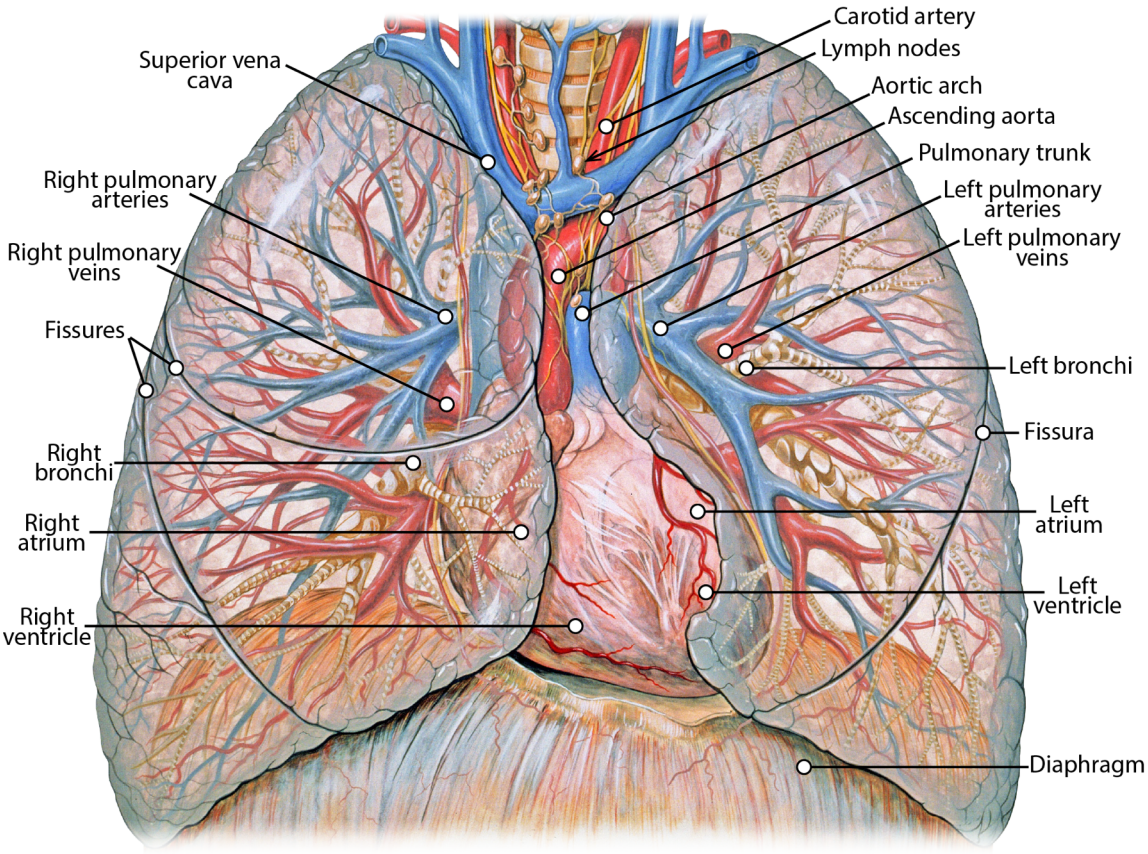

Figure 1.5. Anatomy of the thorax depicting the tangled structure of the pulmonary circulatory system. Adapted from [64] (licensed under Creative Commons).

1.3 Physiology of the lung

1.3.1 Ventilation and gas diffusion

The respiratory tract works as a system of pipes in which air is funneled into the lung. In this tract, the air gets warmed, filtered, and moistened until it reaches the alveoli where the gas exchanges take place by diffusion: the oxygen (O_2) enters the red blood cells in the pulmonary capillaries while the CO_2 exits the blood and enters the alveoli. Diffusion takes place across the alveolar-capillary membrane due to gradients in the partial pressure of gases (Fick's Law), as depicted in Figure 1.3 on the right. The airflow in and out of the lung (inspiration and expiration) is generated by the respiratory muscles (chest wall and diaphragm), which increase and decrease the size of the thoracic cavity. During this process, the lung parenchyma expands and contracts.

The size of the lung depends on many physiological factors, such as height, body weight, gender, age, ethnicity, and health condition. The volume of air in the lung during respiration changes continuously, and consequently, the lung volume is varying as well. Figure 1.6 shows typical lung volumes and capacities for a 70 kg healthy adult male. During quiet breathing, the lung volume at end expiration is about 2400 ml (Functional Residual Capacity, FRC) and 500 ml of air are inspired/expired per breath (Tidal Volume, TV). Assuming that 12 to 15 breaths occur per minute, a total of 6-8 L of air is inspired/expired per minute. At maximal possible inspiration, the volume of the lung reaches 6000 ml (Total Lung Capacity, TLC); at maximal expiration, 1200 ml (Residual Volume, RV). Various parameters regarding lung ventilation can be quantified by pulmonary function tests (PFTs) such as spirometry, plethysmography, and multiple-breath nitrogen washout measurements. Since pulmonary pathologies can alter lung capacities and global values related to ventilation, PFTs are the first clinical measurement for pulmonary investigation.

1.3.2 Perfusion

Alveolar ventilation combined with blood supply in the capillaries of the alveolar wall is required for adequate gas exchange. To this end, the heart pumps continuously blood through the pulmonary artery at a rate of almost 70 ml per heart-beat (at rest, for a 70 kg healthy adult male). Considering a heart rate of 70 beats/min, the cardiac output is about 5 L/min. The blood in the pulmonary artery flows at a velocity of about 70 cm/s, but due to the large capillary bed and vascular resistance, the speed of blood falls rapidly when it passes through the capillaries (<1cm/s). A red blood cell takes about 4 to 5 seconds to travel through the pulmonary circulation, spending about 0.75 seconds in the pulmonary capillaries. The blood volume in the lung (pulmonary circulation) is about 300 ml, amongst which 75 ml are found in the capillaries.

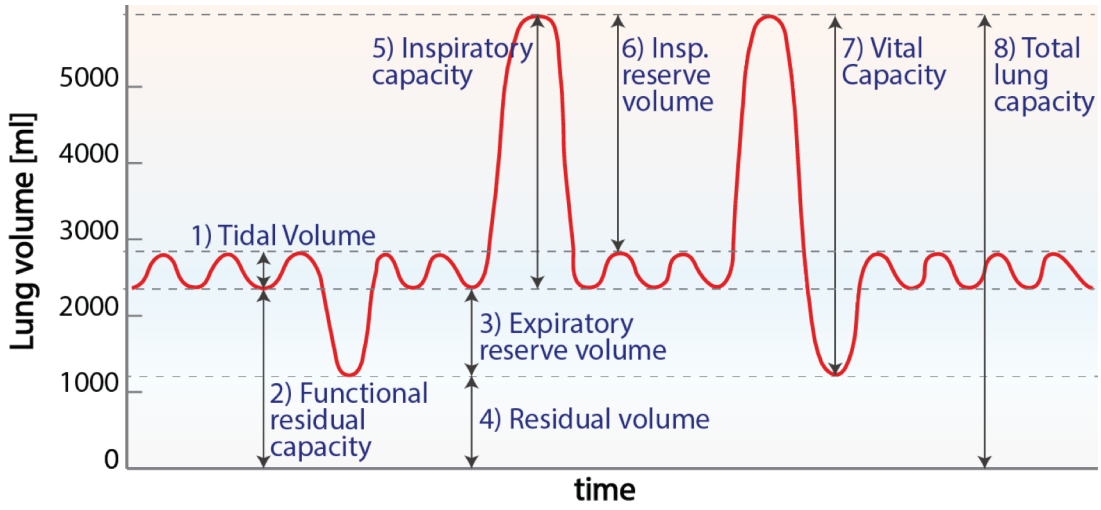

Figure 1.6. Representative breathing pattern indicating typical lung volumes and capacities for an adult male. 1) Tidal volume (TV): air inspired/expired during quiet breathing. 2) Functional residual capacity (FRC): volume of air in the lung at the end of tidal expiration. 3) Expiratory reserve volume (ERV): maximal expired air from the end of tidal expiration. 4) Residual volume (RV): volume of air in the lung after a forced expiratory manoeuver. 5) Inspiratory capacity (IC): maximal volume of air inspired from the end of tidal expiration. 6) Inspiratory reserve volume (IRV): maximal volume of air inspired from the end of tidal inspiration. 7) Vital capacity (VC): maximal amount of air that can be expired after a forced inspiration. 8) Total lung capacity (TLC): volume of air in the lung after maximal inspiration.

1.3.3 Regional distribution of pulmonary ventilation and perfusion

The dorsal (dependent) part of the lung is denser of vessels, capillaries, and parenchyma compared to the ventral part [65, 66]. Furthermore, the supine position conventionally employed for imaging affects the lung density, the ventilation, and the perfusion. When lying on the back, the gravitational force lets the lung collapse under its own weight, compressing the lung structure, particularly in the dorsal part (see Fig. 3.1). Furthermore, the gravitational force acts on the pulmonary blood, which is consequently increased in the posterior lung as well (see Fig 6.4). Therefore, in supine position, compared to the ventral region, the posterior region is denser, more ventilated (cf. Fig. 3.4), and more perfused [66–73].

1.3.4 Ventilation-perfusion ratio in the lung

An adequate balance between ventilation and perfusion is crucial for efficient exchange within the lung. It would be unfavorable to have a region of the lung that is ventilated but not perfused, since in this case no flowing blood could be oxygenated. Or on the contrary, it would be disadvantageous to have a perfused part of the lung which is not ventilated.

The lung ventilation (V', in ml of air per minute and per 100 ml of tissue) to perfusion (Q', in ml of blood per minute and per 100 ml of tissue) ratio (V'/Q') assesses the efficiency of gas exchange and pulmonary perfusion, i.e., the air ventilating the alveoli and the blood flowing in the capillaries. The average ventilation-perfusion ratio in the whole lung at rest is ranging from 0.8 to 1.2. In a healthy lung, due to the natural inhomogeneities of the organ, regional values of V'/Q' can slightly differ from the average [74]. Furthermore, since the ventral-to-dorsal perfusion gradient is greater than the ventilation gradient, dorsal (dependent) lung regions have lower V'/Q' (~0.8) than ventral regions (~1.2). Pulmonary pathologies can substantially alter these values. Hence, methods to measure ventilation, perfusion, and ventilation-perfusion ratio are clinically relevant.

The ventilation-perfusion ratio in the lung is regulated by vasoconstriction and bronchoconstriction. In case of local alveolar hypoxia (reduced ventilation, e.g., caused by obstructions), vasoconstriction occurs in that area, diverting the blood to other ventilated lung regions. This physiological phenomenon is named Euler-Liljestrand mechanism [75]. Similarly, in case of reduced perfusion (e.g., embolism), bronchoconstriction reduces ventilation in the affected area, automatically shifting ventilation away from the poorly perfused regions [58, 76, 77].

The Euler-Liljestrand mechanism is driven by the partial pressures of O_2 and CO_2in the alveoli. In case of ventilation obstructions, in the alveoli PO_2 will drop since less air is entering, and PCO_2 will rise because less CO_2 can be expired. On the contrary, when perfusion is reduced, the alveolar PCO_2 will drop (hypocapnia) because less CO_2 exits the blood, and since less O_2 dissolves into blood, PO_2 will be higher than healthy lung units (alveolar PO_2 is determined by a balance between O_2 delivered by the ventilation and O_2 removal by the blood flow) [57, 58].

1.4 Pulmonary disorders

Many pathologies can change the tissue characteristics and mechanical properties of the lung, affecting its function. Lung pathologies might result in an increase of the lung density, referred to as "*plus-pathologies*", or in a decreased lung density, referred to as "*minus-pathologies*" [4, 15, 30].

Plus-pathologies are characterized by an increase of cellular tissue (nodules, masses, fibrosis), fluid accumulation (mucus, effusion, oedema), or collapse of the existing pulmonary structures (atelectasis). These pathological conditions often have consequences on pulmonary perfusion and ventilation. For example, in subjects with cystic fibrosis, reduced ventilation as caused by mucus plugs frequently occurs, and hypoxia will automatically decrease perfusion (Euler-

Liljestrand mechanism). Similarly, in subjects with lung tumor, direct occlusions of arteries and airways might take place and hamper pulmonary ventilation as well as perfusion.

Minus-pathologies manifest as hyperinflation, enlargement and destruction of air spaces with emphysema, tissue elasticity decline, as well as air-trapping; for instance, in chronic obstructive pulmonary disease (COPD) and asthma. Due to alveolar hypoxia, *minus-pathologies* are also characterized by a reduction in blood volume as caused by hypoxic vasoconstriction as well as chronic inflammations. These factors can lead to airway function decline and tissue remodeling (i.e., bronchoconstriction, bronchial wall thickening, fibrosis). Further extension of the *minus-pathologies* group might include vascular disorders caused by emboli and cardiac diseases (e.g., congestive heart failure), which directly result in reduced lung perfusion and might cause permanent damages of the pulmonary tissue and function.

Representative MR images of subjects with *plus-pathologies* can be found in Chapters 1, 3 and 6 (Figs. 1.7, 1.8, A3.3, 6.9, and 6.11), and with *minus-pathologies* in Chapters 3 and 6 (Figs. 3.6, 6.7, and 6.8).

1.5 What do we wish to measure?

Pulmonary disorders are represented by alterations of tissue structures and functions. To assess these subtle changes, non-invasive, radiation-free, robust, and rapid imaging modalities are required, offering high resolution as well as high sensitivity and specificity for clinical interpretation. For morphological diagnostics, we thus aim for quantitative visualization of biophysical characteristics such as electron density, proton density, the concentration of various metabolites, transversal and longitudinal relaxation times, alveolar size, and characterization of biological cells. For functional assessment of the lung, ideally, we would need quantitative imaging of haemodynamics, ventilation and air-flow dynamics, mechanics of breathing, gas diffusion (i.e., gas exchange), tissue elasticity, and metabolic imaging.

Nowadays, it is possible to image many of these biomarkers. Magnetic resonance imaging is such an imaging modality, which is not only widely available in the clinical setting, but also essentially radiation-free. Over the years various MRI techniques have been developed for the assessment of lung morphology, tissue characteristics (T_1, T_2, T_2^*), perfusion (commonly using contrast agents), ventilation, and the dynamics of breathing [4, 28–33, 40, 41, 46, 47, 51]. Pulmonary MRI, however, is complicated by many factors [28, 29, 34], and there is much room for further methods development.

1.6 The challenges of lung MRI

Pulmonary imaging with MR is complex [28, 29, 34]. First, the lung has a proton density that is 5 to 20 times lower compared to other organs. Since the acquired MR signal is directly proportional to the proton density, lung tissue suffers from a considerably reduced signal-to-noise ratio.

Second, the lung has an extremely short apparent relaxation time (T_2*), since it is exceptionally heterogeneous and contains a multitude of air-tissue and air-blood interfaces. The lung is composed of tissue and blood, which are diamagnetic [78]. But it is also filled with air, which contains oxygen and is paramagnetic. These interfaces cause microscopic susceptibility effects, i.e., intravoxel magnetic field variations and varying field gradients, which perturb the local MR main magnetic field (B_0). The local magnetic field inhomogeneity creates a wide frequency distribution in the voxels and a frequency shift, leading to a broad distribution of Larmor frequencies. As a result, the air-tissue and air-blood interfaces effect a strong dephasing of the net transverse magnetization. The induced fast signal decay challenges lung MRI. The apparent relaxation rate (T_2*) is extremely short, approximately 1-2 ms at 1.5 Tesla (T) [79]. Contrarily, the T_2 relaxation rate originating by spin-spin dephasing is approximately 66 ms for lung tissue at 1.5T and the T_1 relaxation time is relatively long, about 1375 ms [46]; similarly to other tissues of the human body. Importantly, increasing the MR field strength (e.g., from 1.5T to 3T) results in a higher observable MR signal for imaging (and theoretically a higher signal-to-noise ratio). However, higher field strengths come along with generally decreased tissue T_2 relaxation times as well as enhanced susceptibilities effects leading to an even faster T_2* signal decay. Thus, a higher field strength poses additional challenges for lung MR.

Third, MRI can be hampered by organ motion caused by breathing, cardiac and blood pulsation. The respiratory movement has two consequences: imaging has to be performed either with rapid acquisitions that are robust in the presence of breathing motion (e.g., time-resolved, triggered, or self-navigated); or with feasible breath-holding maneuvers (<20 seconds). Moreover, imaging has to be insensitive to cardiac pulsation and blood flow, since these effects can substantially impair the image quality.

1.7 What lung MRI offers

Despite physical and technical complexities, several imaging sequences have been developed and optimized specifically for lung MRI. To address the difficulties given by the extremely fast dephasing of the spins in the lung tissue (T_2* decay), specific gradient echo (GRE) and fast spin-echo (SE) MR sequences with very short echo time (TE) and repetition time (TR) have been proposed [42–47]. The strength of MRI is its versatility in visualizing both morphology and functions in one single examination. In this section, selected methods for lung MRI are described.

1.7.1 Morphological imaging

1.7.1.1 Clinical protocols

In the past years, several comprehensive diagnostic protocols have been suggested for the assessment of a wide range of pulmonary disorders [4, 15, 28–30, 80]. For diagnostic imaging of the chest in less than 15 minutes, standard non-contrast enhanced protocols include:

- T_2-weighted fast spin echo (e.g., half-Fourier acquisition single-shot turbo spin echo, HASTE) [81] in breath-holding for imaging fluids, mucus, infections, blood, thickening of bronchial walls, nodules, masses, and lymph node. Acquisition time 20 seconds, TE of 20-40 ms and TR of 500 ms, coronal orientation, resolution 2.3 × 2.3 × 6 mm^3. Compare; Figure 1.7a.

- T_2-weighted fast spin echo (e.g., PROPELLER or BLADE) [82] respiratory triggered (navigator) in free-breathing for subjects unable to perform breath-holding. Acquisition time 5-8 min, TE of 80-120 ms and TR of 800-2500 ms, transverse orientation, resolution 2 × 2 × 5 mm^3. Compare; Figure 1.7b. Alternatively, T_2-weighted fat saturated short TI inversion recovery (STIR) [83] in multiple breath-holdings. Acquisition time ~4 min, TE 110 of ms and TR of 3500 ms, transverse orientation, resolution 2.1 × 1.6 × 6 mm^3.

- Time-resolved T_2/T_1-weighted balanced SSFP [84] in free-breathing for visualizing vessels, pulmonary emboli, nodules, cardiac dysfunctions, as well as respiratory mechanics (e.g., adhesion of the pleurae). Acquisition time 40 seconds for 120 images, TE of 0.9 ms, TR of 1.8 ms, coronal orientation, resolution 2.4 × 2 × 4 mm^3. Compare; Figure 1.7c.

- 3D T_1-weighted spoiled gradient echo (e.g., volumetric interpolated breath-hold examination, VIBE) [85] in breath-holding for the assessment of chest masses, lymph nodes, nodules, and consolidations. Acquisition time ~20 seconds, TE of 1ms and TR of 2-3ms, transverse orientation, resolution 1.8 × 1.8 × 4 mm^3. Compare; Figures 1.8a and 6.3.

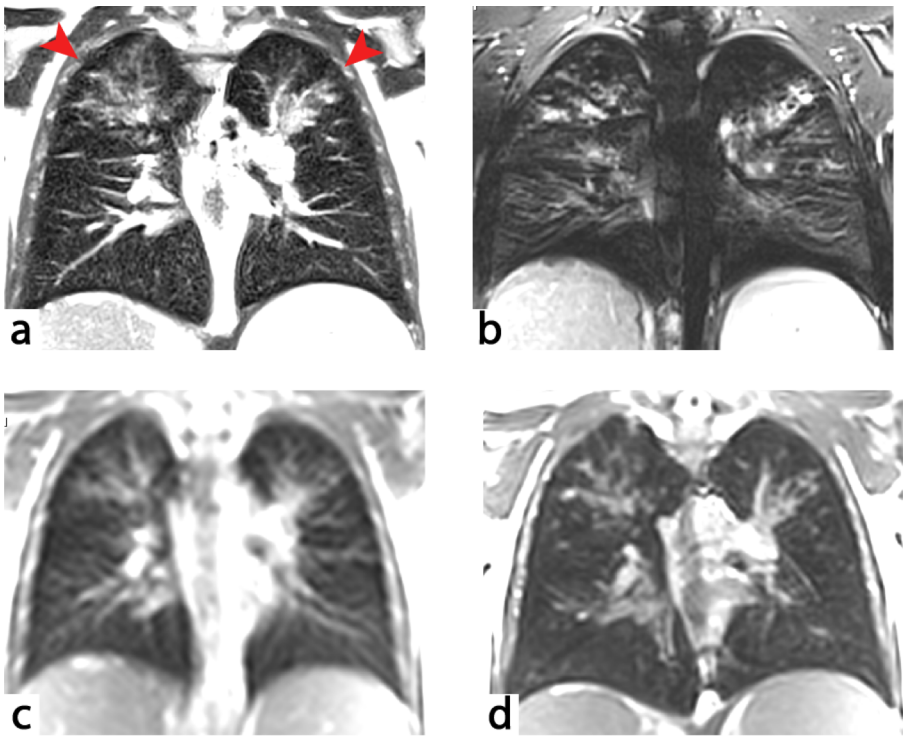

Figure 1.7. HASTE (a), BLADE (b), coronal time-resolved 2D ufSSFP (c), and 3D ufSSFP (d) acquired in a child with cystic fibrosis. Mucus plugs are visible on both the superior lobes of the lung, as exemplarily depicted by the arrowheads in (a). While HASTE, BLADE, and 2D ufSSFP belong to the standard protocols suggested in the literature for lung radiological assessment, 3D ufSSFP was only recently proposed for chest imaging providing volumetric coverage at isotropic resolution [45, 47].

1.7.1.2 Ultra-short echo time

Ultra-short echo time (UTE) imaging is another promising sequence for imaging tissues with rapid T_2* decay. UTE was proposed more than two decades ago for lung parenchyma visualization [86]. Technical difficulties and relatively long scan times limited its integration into the pulmonary protocols of the clinical routine. Nevertheless, UTE has shown promising results in several specific lung studies [55, 87, 88].

The pulse sequence tackles the rapid T_2* decay in the lung with ultra-short TE of about 50-100 µs (TR = 3-8 ms). To reduce motion artifacts and increase acquisition speed, UTE uses non-Cartesian trajectories such as spiral or radial centered-out, accelerated with parallel acquisitions and reconstructions [30, 89, 90]. Furthermore, to minimize the TE, the sampling of the k-space center starts directly after the RF excitation and during the ramp-up of the readout gradient. The TE of UTE refers to the acquisition of the central k-space, while the TE in the outer k-space is lengthened. Due to the acquisition during various TE, the T_2* (and T_2) decay is considerable, which results in a spread of the signal, blurring the image; the resolution of UTE thus differs from the

nominal one. Furthermore, streaking artifacts and blurring are also caused by the complex readout trajectories.

Since the signal of UTE is acquired at diverse echo time, the contrast has a complex behavior, but optically might resemble proton-density and is visually alike to CT imaging. Recent implementations allow for 3D imaging of about 2 × 2 × 5 mm^3 in 16 seconds breath-holding [43] (TE of 0.06 ms and TR of 3.3 ms, see Figs. 1.2b and 1.8b for representative images), or for free-breathing self-navigated imaging with an isotropic resolution of 1 mm in 10-15 minutes' acquisition time [42, 44].

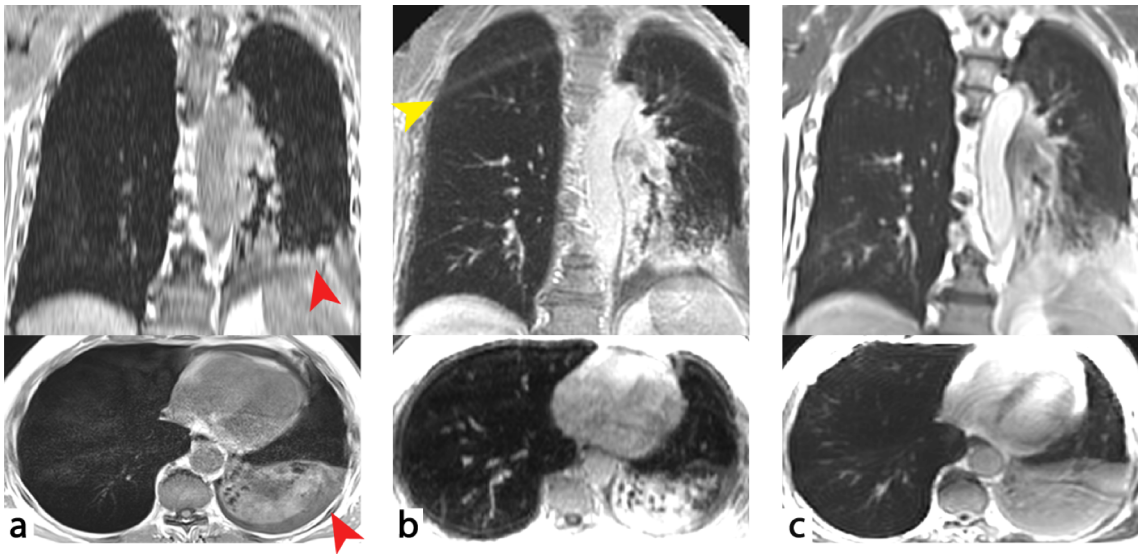

Figure 1.8. VIBE (a), UTE (b), and 3D ufSSFP (c) imaging in a patient with a non-small cell lung cancer (NSCLC) invading the left inferior lobe of the lung, as exemplarily indicated by the red arrowheads in (a). The yellow arrowhead in (b) point to a typical artifact seen with UTE related to the spiral trajectory, especially in case the chest is very large or not perfectly positioned in the center of the field-of-view.

1.7.2 Pulmonary relaxometry

Relaxometry has been investigated as a potential quantitative biomarker for the assessment of several pathologies in the human body [91]. For the lung, a multitude of technique has been proposed. For T_1 quantification, inversion recovery (IR) half-Fourier acquisition single-shot turbo spin echo (IR-HASTE) and snapshot-fast low-angle shot (FLASH) [92, 93]. For simultaneous measurement of T_1 and T_2*, a UTE implementation has been recently introduced for 3D imaging with scan time of about 10 min [94]. Clinical transition of these techniques is still limited by relatively long scan times. For simultaneous quantification of T_1, T_2, as well as proton density, IR-ufSSFP has

recently shown compelling results for rapid and robust 2D acquisition in less than 10 seconds breath-holding for a resolution of 2.4 × 2.4 × 10 mm^3 [46]. Representative quantitative maps obtained with IR-ufSSFP imaging can be found in Chapter 5 (Fig. 5.1).

1.7.3 Functional imaging

The fundamental function of the lung is to ensure blood oxygenation and elimination of carbon dioxide, which is achieved through pulmonary ventilation, gas diffusion, and blood perfusion. Measuring qualitatively and quantitatively these complex physiological processes is a necessity to evaluate the disease progression, prognosis and treatment outcomes. Herewith, chosen MR functional techniques are described.

1.7.3.1 Dynamic contrast-enhanced MRI

Dynamic contrast-enhanced MRI (DCE-MRI) is the standard clinical technique for perfusion imaging, allowing for mapping blood flow (i.e., perfusion, in ml of blood delivered per minute in 100 ml of tissue), volume, and mean transit time [28, 29]. DCE-MRI allows mapping haemodynamics and visualizing perfusion-related impairments. Nevertheless, DCE-MRI also permits an indirect insight into ventilation defects, because of the hypoxic pulmonary vasoconstriction in case of ventilation obstructions.

For DCE-MRI, time-resolved T_1-weighted 3D spoiled gradient echo datasets with short acquisition times (1-2 seconds) are continuously acquired after intravenous contrast agent administration. Imaging is performed in one breath-hold (15-20 seconds) following the injection of a paramagnetic contrast agent bolus (e.g., gadolinium), which shortens T_1 (as well as T_2) of blood and tissues, increasing the detected signal. Three-dimensional time-resolved imaging permits to visualize the passage of the contrast agent in the arterial and venous blood and to calculate haemodynamic parameters. The imaging speed for DCE-MRI is achieved thanks to k-space undersampling, parallel imaging, and echo sharing. Typical measurements parameters are: resolution is 4 × 4 × 5 mm^3, TE of 0.7-1 ms and TR of 1.5-2.5 ms [30]. Representative perfusion maps derived with DCE-MRI are shown in Chapter 3 (Fig. 3.6).

1.7.3.2 Oxygen-enhanced MRI

Oxygen-enhanced (OE) MRI exploits the paramagnetic properties of oxygen which can serve as a weak T_1-shortening contrast agent [95]. When breathed, oxygen reaches only the ventilated alveoli, passes only through the functional alveolar walls (i.e., alveolar and capillary epithelia), and dissolves into blood only in perfused capillaries. If one of the three functions is locally compromised, oxygen does not dissolve into the blood and no regional shortening in T_1 takes place.

By this means, OE-MRI provides functional information related to ventilation, diffusion, and perfusion [96].

Oxygen enhancement maps can be calculated from acquisitions performed in normoxic (air) and hyperoxic (e.g., 100% oxygen) conditions. For semi-quantitative OE-MRI (i.e., relative oxygen enhancement), T_1-weighted sequences such as IR-HASTE, IR-FLASH or UTE are usually employed [56, 93, 97]. For quantitative oxygen enhancement, the shortening in T_1 is commonly calculated from IR-FLASH scans (Look-Locker), UTE or HASTE [98–100]. In the work presented in this thesis, OE-MRI was performed with ufSSFP sequences. Representative images can be found in Chapters 4 and 5 (Figs. 4.7 and 5.2).

OE-MRI was also proposed to measure ventilation with a spoiled gradient echo (SPGR) sequence: since oxygen is paramagnetic, it increases the magnetic susceptibilities at the air-tissue interfaces in the lung, only in ventilated regions. Therefore, a change in T_2^* allows estimating pulmonary ventilation [101].

OE-MRI can be implemented easily for commercial scanners and is inexpensive; furthermore, breathing oxygen for short periods of time has usually no contraindications in several pathologies. However, the shortening of T_1 given by O_2 is weak and difficult to be imaged. In addition, OE-MRI requires scanning in two different oxic conditions, doubling the scan time and hampering the transition to the clinical routine.

1.7.3.3 Fourier decomposition MRI

The signal intensity of the lung during respiration exhibits modulations arising from the parenchyma density changes (compression/expansion) and from the inflow of blood passing through arteries and parenchymal capillaries at every cardiac pulsation. These signal modulations can be captured by time-resolved 2D balanced steady-state free precession (bSSFP) imaging with a TE of 0.9 ms and a TR of 1.9 ms (or shorter) in coronal or sagittal views [102]. Typical in-plane resolution is approximately 3.5 × 3.5 mm^2 for coronal acquisitions, with a slice thickness of 10 mm.

The acquisition time of one image with 2D bSSFP is 118 ms, therefore imaging is performed in the transient phase of the magnetization [103]. An interval time of 180 ms between successive acquisitions is programmed for magnetization recovery (especially of blood), resulting in an acquisition frame rate of 3.33 images / second. For Fourier decomposition (FD) MRI, a series of 200 images is acquired in 1 minute of free-breathing. After specific deformable image registration to a reference image, perfusion-weighted and ventilation-weighted maps are calculated by integration of cardiac (~1 Hz) and respiratory (~0.2 Hz) spectral lines obtained after Fourier analysis

[102]. Specifics about the most recent Matrix Pencil (MP) algorithm employed to calculate perfusion, blood arrival time, and ventilation in FD-MRI are described in Ref. [104].

FD-MRI has been validated in animal studies and initial results in patients showed clinical relevance for ventilation and perfusion imaging [33, 53, 102, 105, 106]. Since the technique does not require any contrast agent, nor gaseous media, and is rapid and quantitative, it has the potential for broad clinical application and longitudinal monitoring of patients. Representative FD-MR images are included in Chapter 2 (Fig. 2.4).

1.8 Imaging with balanced steady-state free precession

Balanced steady-state free precession (bSSFP) sequences belong to a type of fast gradient echo sequences employing short repetition times [107, 108]. The echo is formed after every RF excitation by a dephasing and rephasing gradient pattern along the frequency-encoding axis, as shown in the sequence scheme in Figure 1.9. Within each TR, the gradient moments along all three orthogonal axes are fully rewound, i.e., the total net gradient area and thus the net dephasing (in case of spins not in motion) are zero in each RF cycle. Due to the short TR of bSSFP (TR << $T_2 < T_1$), the longitudinal magnetization of the spins has not sufficient time to relax back to the equilibrium before the application of the next RF pulse, and similarly, the transverse magnetization does not decay to zero. As a result, the continuous application of RF excitations allows generating a dynamic equilibrium, and a steady-state signal is formed. The steady-state condition is reached after a certain number of excitation pulses and can be established rapidly with specific preparation schemes [109].

At on-resonance, in the limit TR << $T_2 < T_1$ and for echoes occurring in the center of TR (i.e., TE = TR/2), the bSSFP signal in case of alternating RF pulses ($\pm\alpha$) is given by:

$$S_{\mathrm{bSSFP}}(\alpha, T_1, T_2, \mathrm{TR}) \approx \frac{M_0 \cdot \sin\alpha}{1 + \cos\alpha + (1 - \cos\alpha)(T_1/T_2)} \cdot e^{-\frac{\mathrm{TR}}{2 \cdot T_2}}, \tag{1.1}$$

where M_0 is the equilibrium magnetization (proton density), and α is the flip angle.
The optimal flip angle for bSSFP maximal signal intensity can be derived from the previous Eq. (1.1) as

$$\alpha_{\mathrm{opt}} = \cos^{-1}\left(\frac{T_1/T_2 - 1}{T_1/T_2 + 1}\right), \tag{1.2}$$

which leads a maximal signal amplitude of

$$S_{\mathrm{bSSFP,max}} = S_{\mathrm{bSSFP}}|_{\alpha = \alpha_{\mathrm{opt}}} = \frac{1}{2} M_0 \sqrt{\frac{T_2}{T_1}} \cdot e^{-\frac{\mathrm{TR}}{2 \cdot T_2}} . \quad (1.3)$$

From Eq. (1.3), it is clear that the signal of bSSFP is proportional to T_2/T_1. Furthermore, it can be noted that the signal of bSSFP at TE = TR/2 is T_2-weighted (i.e., $e^{-\frac{\mathrm{TR}}{2 \cdot T_2}}$), similarly to spin-echo sequences, and it is not T_2*-weighted (i.e., $e^{-\frac{\mathrm{TR}}{2 \cdot T_2^*}}$) as common gradient echo sequences [108–111]. As a result, especially for the lung tissue which is governed by a very short T_2*, bSSFP can achieve a higher signal than spoiled gradient echo sequences. Balanced SSFP sequences offer the highest possible signal-to-noise ratio (SNR) per unit time of all known sequences and in addition are rather insensitive to motion and flow effects [108]. However, as a consequence of the balanced gradients, the signal of bSSFP is strongly sensitive to off-resonance effects (bandings), caused by susceptibility variations, imperfections of the main magnetic field (B_0) or chemical shift. Shimming can mitigate inhomogeneities of B_0, but the susceptibility effects are inevitable. An efficient way to eliminate off-resonance effects is the use of a very short TR, e.g., <3-6 ms for typical imaging targets [108].

Balanced SSFP is suited for imaging tissues with different T_2/T_1 ratios: the signal will appear very bright for blood, vessels, liquids, and fat, and darker for muscle and other tissues. The rationale to use bSSFP for lung MRI is quite evident. Balanced SSFP provides fast acquisitions, is robust in the presence of motion, has the highest SNR per unit time amongst all sequences and a strong signal from blood and vessels. These factors make bSSFP a perfect candidate for imaging an organ with reduced proton density such as the lung, in free-breathing or with rapid breath-holding maneuvers. Nevertheless, the application of bSSFP for lung imaging has been hindered by technical challenges. Namely, the shortest achievable TR with conventional bSSFP sequences at commercial scanners is limited to about 2 ms, still causing residual off-resonance related banding artifacts and signal voids in the lung (cf. Fig. 1.9). An even shorter TR is thus desirable for successful lung bSSFP imaging.

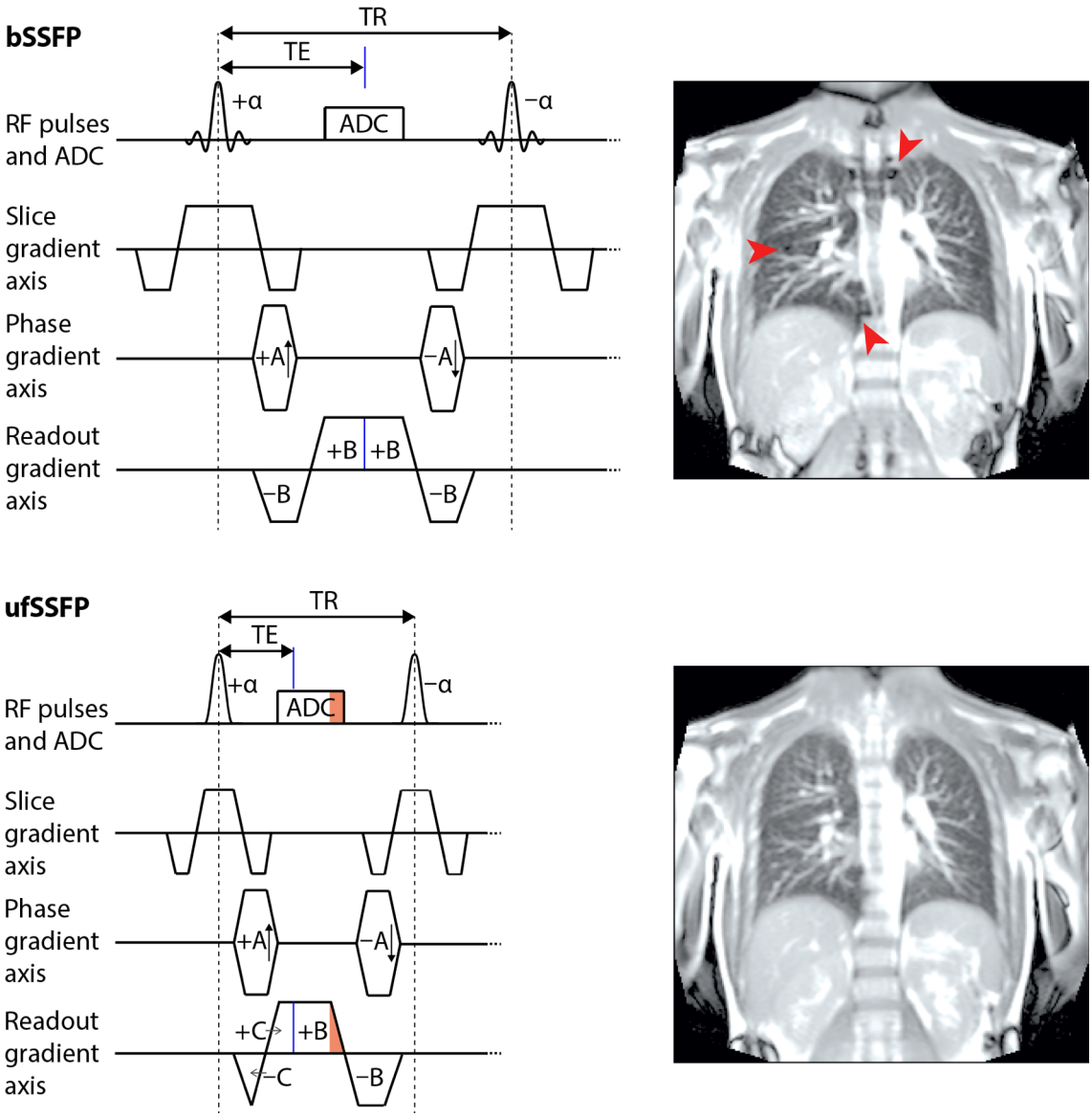

Figure 1.9. Diagrams (left) of a 2D bSSFP pulse sequence (top) and of 2D ufSSFP (bottom) including typical acquired images (right). After the RF excitation pulse, the phase and frequency encoding is started. Within each TR, the net gradient area and dephasing are zeroed (fully refocused). Compared to conventional bSSFP, ufSSFP reaches a shorter TR due to shortened RF pulses, asymmetric readout (i.e., C<B in the diagram), and sampling on the ramp-down readout gradient (marked in orange). The sequence scheme for 3D SSFP sequences is similar, including additionally a phase-encoding gradient (and a rewinder gradient) along slice-selection direction (not illustrated). The repetition time / echo time for the presented images acquired with 2D bSSFP and 2D ufSSFP acquisition were 1.9 ms / 0.87 ms and 1.46 ms / 0.67 ms, respectively. The red arrowheads indicate signal voids in the lung using bSSFP (top right), which are mitigated by ufSSFP (bottom right).

1.9 Balanced-SSFP with minimal TR: ultra-fast SSFP

Recently, a novel bSSFP implementation was proposed for pulmonary imaging with extremely short TR, termed ultra-fast SSFP [45]. There are two factors that need to be considered to achieve a TR as short as possible. The first is the design of a short RF pulse and the second to ensure a rapid Cartesian image encoding scheme. Usually, in the common implementation of the bSSFP sequence, the flip angle is produced by a SINC-shaped RF pulse with a relatively long fixed duration that allows to generate flip angles that are even larger than 90°. However, as derived from Eq. (1.3), the optimal flip angle for the steady-state signal is only about 25° in the lung tissue ($T_1 \approx 1375$ ms and $T_2 \approx 66$ ms)[46]. As a consequence, the following minimal RF pulse duration can be obtained: for 3D ufSSFP, non-selective rectangular-shaped pulses of 70 µs duration (hard pulses); and for 2D ufSSFP, Gaussian-shaped pulses of 240 µs duration. Moreover, the time that is required for image encoding is mainly determined by the readout. As a consequence, ufSSFP combines asymmetric echoes and ramp sampling techniques to shorten the readout time.

A scheme of the optimized ufSSFP sequence including a representative image is shown in Figure 1.9. Using an asymmetric echo, the TR can be reduced in comparison to the centered echo (TE = TR/2). Therefore, in this optimized ufSSFP implementation, the echo is slightly shifted away from TR/2. Since the achieved TR is extremely short, the additionally introduced T_2^* weighting is marginal. Both, theoretical simulations as well as in-vivo experiments demonstrated that in the lung tissue, a truly balanced SSFP is obtained only with TR < 2 ms; with TR > 2 ms, due to intravoxel dephasing, a rather unbalanced SSFP is produced with signal amplitudes that are only half as high in comparison to bSSFP [45].

In conclusion, 3D ufSSFP has the ability to achieve for example TR/TE as short as 1.08 ms / 0.42 ms for a 2.5 mm isotropic resolution, allowing imaging of the whole lung in 18 seconds with 3 averages (parallel imaging, Grappa acceleration factor 2). In 2D mode, ufSSFP can achieve TR/TE as short as 1.36 ms / 0.52 ms for an in-plane resolution of 1.8×1.8 mm^2 and a slice thickness of 8 mm with an acquisition time of 110 ms per slice. Representative lung images obtained with 3D ufSSFP can be found, e.g., in Figures 1.2c, 1.7d, 1.8c, and in Chapters 3 and 6 (Figs. 3.1 and 6.1). A comparison of 2D bSSFP and 2D ufSSFP is presented in Chapter 2 (Fig. 2.4).

The optimized ufSSFP sequence provides diagnostic lung imaging with a high signal-to-noise ratio, free of banding, and with only minor motion artifacts and image degradation [45, 47]; ideal to develop new functional imaging techniques and to improve the robustness and reliability of existing methods.

1.10 Aim of the thesis

Morphological and functional imaging of the lung is of high clinical importance. The main drawback of current clinical standards, such as CT and nuclear medicine techniques, is the implied radiation dose, particularly when longitudinal imaging is required to monitor the disease progression and medical interventions. Especially for children, where pathologies could affect the lung development and reduce their quality of life, radiation-free imaging modalities are an urgent necessity. Non-proton based MRI with inhaled hyperpolarized gas (i.e., ^{3}He, ^{129}Xe, ^{19}F) showed promise for measuring several functional biomarkers of the lung (e.g., ventilation and alveolar size), but the need for dedicated equipment and specialized staff limit its transition to the clinics.

On the other hand, proton MRI is radiation-free and widely available. Nevertheless, proton lung MRI is challenging. In fact, the physical characteristics of the lung tissue that are unfavorable for MRI (i.e., low proton density and short apparent transverse relaxation time, cf. Section 1.6) can lead to a low detected signal; not sufficient for a veritable evaluation of pulmonary structures and function. These present limitations have been recently mitigated with accelerated bSSFP schemes, namely with ufSSFP sequences that are characterized by an extremely short TR (cf. Section 1.9) and yield an improved signal-to-noise ratio of the pulmonary tissues and artifact-free images [45]. Within the work presented in this thesis, new and improved techniques were developed with ufSSFP acquisition schemes for accurate pulmonary functional imaging at 1.5 Tesla.

It has been shown previously that time-resolved two-dimensional bSSFP imaging of the lung during free-breathing and Fourier decomposition (FD) of the physiological signal modulations allow calculating quantitative maps related to pulmonary perfusion and ventilation [102]. The purpose of the first work included in this thesis (**Chapter 2**) is to adapt ufSSFP imaging for FD-MRI with an increased signal and functional image quality. Thanks to free-breathing acquisitions, FD-MRI can easily be performed in clinical settings. As a major drawback, however, FD-MRI is limited to 2D imaging, thus covering only portions of the thorax. Furthermore, FD-MRI ventilation measurements depend on the breathing amplitude of the examined subject.

These limitations have been overcome in the second work described in **Chapter 3** where rapid 3D multi-volumetric ufSSFP breath-hold acquisitions combined with a model of the lung are used to retrieve voxelwise the parameter α, a new ventilation-weighted quantitative measure that describes the compression/expansion of the lung. The index α is independent of the breathing amplitude as well as the lung density and capacity. The quantitative parameter α strongly differs

from ventilation-related biomarkers presented in the literature, such as simple subtraction of images acquired at diverse respiratory level [112, 113]. The difference between the derived novel ventilation parameter α and contemporary ventilation measures is briefly described in the Addendum to Chapter 3. Within the scope of the **Addendum to Chapter 3**, the ventilation impairments quantified with α-mapping are evaluated in a cohort of children with cystic fibrosis.

Oxygen-enhanced (OE) MRI allows for an indirect measure of ventilation, diffusion, and perfusion. Usually, OE-MRI is performed with T_1-weighted imaging (IR-HASTE or UTE). Since the signal enhancement given by oxygen is weak, the measured oxygen enhancement can be flawed by the signal changes in the parenchyma caused by different inspiratory levels. In the third work included in **Chapter 4**, 3D multi-volumetric ufSSFP breath-hold imaging is combined with a lung model (as described in Chapter 3) to take into account these density variations for the calculation of robust oxygen-enhancement maps.

Relaxation time measurements (T_1 and T_2) have demonstrated clinical value for various pathologies of the human body [91]. Lung T_1 relaxometry in combination with oxygen breathing as contrast agent has been explored for physiological imaging in several studies and has shown good prospect amongst certain patient groups [92, 93, 114, 115]. Usually, inversion recovery GRE or HASTE sequences are employed for pulmonary T_1-relaxometry. Recently inversion recovery ufSSFP has shown promise for robust lung T_1 and T_2 relaxometry [46]. Therefore, the objective of the fourth work (**Chapter 5**) is to employ 2D IR-ufSSFP breath-hold imaging to rapidly and simultaneously map theT_1 and T_2 relaxation times of the lung under normoxic and hyperoxic conditions. The proposed quantitative OE-MRI method allows mapping functional biomarkers such as the change in the T_1 and T_2 relaxation time after hyperoxic conditions (i.e., ΔT_1 and ΔT_2) or the physiological oxygen wash-in and wash-out time constants (related to the time needed to shorten T_1 after oxygen breathing).

The vascular integrity of the pulmonary parenchyma is usually assessed by SPECT/CT, which is a time-consuming imaging modality with rather low spatial resolution, and furthermore, it is radioactive. Many MR radiological protocols include contrast agent, e.g., for lung perfusion with DCE-MRI, cardiac examinations, or the evaluation of mediastinal masses. It is thus appealing to add to these protocols a rapid imaging technique optimized for parenchyma functional assessment to ameliorate the diagnosis, the disease characterization as well as to quantify the pulmonary impairments caused by the pathology. Even though bSSFP sequences are considered to be rather insensitive to contrast agents, they have shown promise to detect the signal increase after contrast agent administration [116, 117]. As a consequence, in the last work (**Chapter 6**), signal enhancement ratio (SER) mapping is presented – a rapid technique developed for specific visualization of disorders altering regional lung parenchyma perfusion.

1.11 Outline of the thesis

The naturally occurring lung signal modulations associated with pulmonary blood flow and respiration are used to recover perfusion and ventilation imaging in Chapter 2. Similarly, in Chapter 3 ventilation maps are calculated from the lung signal modulations occurring at diverse respiratory levels. In Chapters 4 and 5, pure oxygen is breathed and acts as a mild contrast agent, thus enabling pulmonary imaging that contains information about ventilation, diffusion, as well as perfusion. Finally, Gadolinium contrast agent is employed for functional imaging related to pulmonary parenchyma perfusion in Chapter 6.

Chapter 2. An optimal ufSSFP sequence scheme with minimal TR and TE is presented for FD-MRI. Optimization with regard to the achievement of a short TR includes shortening of the RF pulse duration and the use of an asymmetric readout. Furthermore, ramp-up and ramp-down radio-frequency (RF) preparation pulses to stabilize the magnetization vector are introduced. The influence of the flip angle, RF pulse length, in-plane resolution, field-of-view, and image acquisition rate (i.e., the temporal resolution) are evaluated to optimize the FD-MRI protocol with respect to parenchyma signal intensity and image quality. FD-MRI with optimized ufSSFP acquisitions is compared to conventional bSSFP in healthy volunteers at 1.5T. Furthermore, the optimized FD-MRI protocol is also evaluated at 3T.

Chapter 3. Three-dimensional multi-volumetric ufSSFP breath-hold imaging is used to study the lung SI modulations at diverse respiratory volumes (i.e., capacities). A simple compression model of the lung is introduced to retrieve voxelwise the measure α; a novel quantitative parameter for lung ventilation imaging that is nearly independent of the breathing phases, lung density and capacity. Three-dimensional α-mapping is evaluated in healthy volunteers, two COPD patients and one cystic fibrosis patient, and compared to DCE-MRI, FD-MRI, and CT. Moreover, in the **Addendum to Chapter 3**, α-mapping is evaluated in 24 pediatric patients with cystic fibrosis (CF). The ventilation impairments are quantified with α-mapping and compared to the lung clearing index (LCI), a functional lung parameter resulting from nitrogen multiple-breath washout measurements (N_2-MBW) [118].

Chapter 4. Three-dimensional ufSSFP breath-hold imaging is employed for OE-MRI. After flip-angle optimization, multi-volumetric ufSSFP lung imaging under both normoxic (air, 21% O_2) and hyperoxic conditions (100% O_2) is investigated in healthy volunteers. The lung model retrieved in Chapter 3 is used to map the oxygen enhancement (percentage of signal increase), mitigating the confounding bias inherent to common OE-MRI techniques that arises from residual lung density modulations. Even when the imaging is performed at a fixed inspiratory level (e.g., FRC), lung

density variations lead to a bias in contemporary OE-MRI methods since it is, in practice, not possible to exactly reproduce a given inspiratory level.

Chapter 5. Pulmonary OE-relaxometry with IR-ufSSFP is evaluated in healthy volunteers. Cardiac-triggered breath-hold imaging with IR-ufSSFP is continuously performed every 30 s; first in normoxic conditions for 5 min, then in hyperoxic conditions for 5 min (wash-in), and again in normoxic conditions for 5 min (wash out). Quantitative maps of T_1 and T_2 change between the different oxic conditions (ΔT_1 and ΔT_2), as well as maps representing the oxygen wash-in and wash-out time constants (i.e., the characteristic rate of T_1 decrease and increase), are calculated. It is important to note that OE-relaxometry does not require density corrections (cf. Chapter 4) since it provides quantitative measures of T_1 and T_2 that are not proton-density weighted.

Chapter 6. Static signal enhancement ratio (SER) maps (percentage of signal enhancement) are calculated from 3D ufSSFP breath-hold imaging, acquired once before and once 3 min after intravenous Gadolinium-based contrast administration. Post-contrast imaging for static SER mapping is performed 3 min after the injection of Gadolinium to ensure a constant dilution and distribution of the contrast agent in the blood pool. The flip angle is optimized considering the maximal signal intensities of ufSSFP in the lung, before and after contrast agent administration, as well as the stability of the signal [117]. To motivate the use of ufSSFP for lung imaging, the image quality and the signal level yielded by ufSSFP imaging are compared to contemporary volume-interpolated breath-hold examinations (VIBE) in 10 subjects with healthy lung. Secondly, ufSSFP-SER maps are evaluated in 9 patients with different pulmonary diseases (3 COPD, 4 COPD+ lung cancer, 1 pulmonary fibrosis, 1 traumatic lung contusion). For the COPD cohort, SER is compared to ^{99m}Tc-MAA-SPECT/CT by radiological scoring of lung deficits.

CHAPTER 2

Ultra-fast steady-state free precession pulse sequence for Fourier decomposition pulmonary MRI

A modified version of this chapter has been published as:

Pusterla O*, Bauman G*, Bieri O. *Ultra-fast Steady-State Free Precession Pulse Sequence for Fourier Decomposition Pulmonary MRI.* Magn Reson Med, 2015, 75:1647-53.

*Equally contributed to this work.

CHAPTER ABSTRACT

Purpose: To assess whether ultra-fast steady-state free precession (ufSSFP) can improve image quality in Fourier decomposition (FD) MRI of lung ventilation and perfusion.

Methods: Series of two-dimensional time-resolved lung images were acquired in healthy volunteers at 1.5T and 3T using an FD adapted ufSSFP. For comparison, the imaging protocol was complemented by a standard implementation of the FD-MRI technique using balanced steady-state free precession (bSSFP). Imaging parameters were evaluated to optimize the ufSSFP FD-MRI protocol with respect to the signal intensity of the lung parenchyma and the severity of image artifacts.

Results: FD-MRI with the adapted ufSSFP pulse sequence resulted in increased signal intensity in the lung tissue by 19% and significantly decreased banding artifacts due to shorter repetition times: 1.46 ms for ufSSFP and 1.90 ms for bSSFP. Despite improved image quality FD-MRI is still problematic at 3T.

Conclusion: MRI of the lung with ufSSFP performs better than bSSFP in terms of signal and banding artifacts, and can be used to either increase resolution or overall image quality of FD images.

2.1 Introduction

Nowadays, radionuclide planar scintigraphy and single photon emission computed tomography (SPECT) are widely accepted as a clinical standard for the measurement of pulmonary perfusion and ventilation [19, 20]. Nuclear techniques, however, are based on the application of radioactive labeled tracers and are thus limited by relatively poor spatial and temporal resolution. As a result, non-ionizing methods, such as magnetic resonance imaging (MRI) with inhaled hyperpolarized noble gases (^{3}He, ^{129}Xe) were introduced for the assessment of static and dynamic lung ventilation [38, 119]. Alternatively, pulmonary function can also be assessed by proton MRI using a T_1-shortening contrast agent, such as oxygen, for ventilation mapping [95], or by the injection of gadolinium-based contrast agents for the evaluation of pulmonary perfusion [120, 121] but not without the possible risk of acute allergic reactions and nephrogenic systemic fibrosis in patients with impaired renal function [122]. Hence, simple, easy and non-invasive MRI techniques for the assessment of regional pulmonary function are highly desirable.

In the recent years a novel, native, functional lung imaging method, known as Fourier decomposition (FD) MRI, has been introduced [102] providing ventilation-weighted (Vw) and perfusion-weighted (Qw) information from a single acquisition series, requiring no administration of contrast agent, as well as no further patient compliance such as repeated or prolonged breath holding. FD-MRI was validated in animal experiments against other imaging modalities including SPECT/CT, DCE-MRI and ^{3}He-MRI [105, 123] and first clinical data were obtained in a population of cystic fibrosis patients and non-small cell lung cancer patients for assessment of regional perfusion [106, 124]. Nevertheless, the application of FD-MRI in some groups of patients, e.g., chronic obstructive pulmonary disease (COPD), can be limited from the presence of emphysematous lung destruction leading to very low regional signal intensity. Here, the key limitation of FD-MRI is the minimal achievable echo time (TE), which is too long to sufficiently sample very fast decaying signal.

Only recently, some major methodological advances have been demonstrated for lung imaging based on a very fast steady state free precession (SSFP) imaging technique, termed ultra-fast SSFP (ufSSFP) [45]. For ufSSFP, excitation pulses and gradient switching patterns of a conventional Cartesian SSFP imaging scheme were optimized, and further reduced by partial echo readouts and ramp sampling techniques. As a result from the overall reduced repetition time (TR), image acquisition is shortened, motion and banding artifacts are reduced, and the parenchyma signal is increased.

Consequently, the purpose of this work is to fuse two recently introduced promising concepts, namely FD-MRI and ufSSFP imaging, for improved lung imaging in the clinical setting.

2.2 Methods

2.2.1 Adaptation and optimization of ufSSFP for FD-MRI

The basis of FD-MRI is a time-resolved series of 2D balanced SSFP acquisitions with a frame rate of about 3-4 images per second to assess lung function from signal modulations caused by respiratory and cardiac cycles. Overall, due to the very short T_2* relaxation times of lung tissue at 1.5T [34], the key factor driving balanced SSFP image quality and visibility of the lung parenchyma is TR.

Figure 2.1 shows a schematic of the acquisition using a balanced ufSSFP scheme. Generally, the 2D image acquisition blocks are interleaved by a time interval (TW) for magnetization recovery and imaging is thus performed mainly during the transient state. Overall, TR is reduced using a tailored duration of the radio-frequency (RF) excitation pulse adjusted to the limit given by the specific absorption rate (SAR) and by partial echoes [45]. The readout asymmetry was set to 75% of the full echo and combined with POCS [125] reconstruction of the missing *k*-space data. A ramp of 10 RF pulses increasing linearly from $\alpha/10$ to α was used to stabilize the magnetization vector [126]. An optional post scanning linear ramp down scheme of 10 subsequent RF pulses for magnetization refocusing was also implemented and a linear *k*-space reordering was chosen to mitigate eddy currents [127].

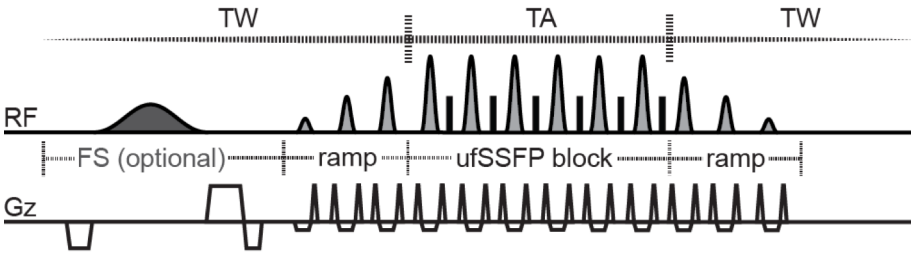

Figure 2.1. Schematics of the FD-MRI adapted ultra-fast steady-state free-precession (ufSSFP) imaging sequence comprising an optional fat saturation block (FS), ramp-up and ramp down magnetization preparation steps for stabilization of the magnetization vector, image acquisition block (TA), and time interval (waiting time: TW) between consecutive image acquisitions.

2.2.2 MRI data acquisitions

Experiments were performed on a 1.5T MR-scanner (MAGNETOM Avanto, Siemens Healthineers, Erlangen, Germany) using a 12-channel thorax and a 24-channel spine coil receive-array. Five healthy volunteers were examined with both a time-resolved 2D ufSSFP sequence, as well as a standard 2D bSSFP used in previous publications on the FD-MRI [102, 105, 106, 123, 124]. Generally, scans were performed with predefined default shim settings and on the same volunteer on the same day.

The dependence between the signal intensity (SI) in the lung parenchyma and the flip angle (α), the duration (τ) of sinc-shaped RF pulses, the interval time (TW) between each image acquisition and spatial resolution was analyzed in expiratory breath hold with variable parameters: α = 5°–75°, τ = 250–500 µs, TE = 0.61–0.75 ms, TR = 1.37–1.61 ms, TW = 0–280 ms, leading to variable acquisition times TA = 80–160 ms for spatial resolutions ranging from 4.7×4.7 mm^2 (96×96 matrix) to 2.6×2.6 mm^2 (176×176 matrix). The acquisition rate was kept constant at 3.33 images/s by adapting the interval length TW, with and without the post-scan linear RF ramp, for a fixed field-of-view (FOV) = 450×450 mm^2, slice thickness = 12 mm, bandwidth in a range 2003-2056 Hz/px, 64 images per slice, parallel imaging GRAPPA [128] factor 2. Additionally, simple numerical simulations of the magnetization vector evolution using Bloch equations (taking into account relaxation but neglecting pulmonary perfusion and susceptibility effects) were performed to explore the relationship between flip angle and signal intensity in the lung parenchyma to qualitatively check whether the calculations supported the experimental data [129]. In the simulation we assumed that the lung tissue is characterized by T_1 = 1000 ms and T_2 = 60 ms (15).

For ventilation and perfusion imaging, sets of time-resolved images were acquired in free-breathing with a fixed flip angle and RF pulse length of α = 65° and τ = 360 µs, but otherwise identical imaging parameters to the breath hold scans. Two hundred images were acquired per slice with a total acquisition time of 66 seconds per slice. A supplemental acquisition with a fat saturation RF pulse was performed, for possible beneficial suppression of ghost artifacts from oscillations of the magnetization occurring in the transient state. For comparison, scans using the standard bSSFP sequence was performed [102]. The main sequence parameters were as follows: TE/TR/TA = 0.8/1.9/118 ms, TW = 180, acquisition rate = 3.33 images per second, α = 75°, FOV = 450×450 mm^2, slice thickness = 12 mm, matrix = 128×128 (resolutions of 3.5×3.5 mm^2), GRAPPA factor 3.

Additionally, we scanned one healthy volunteer at a 3T clinical MR-scanner (MAGNETOM Prisma, Siemens Healthineers, Erlangen, Germany) using an 18-channel thorax and a 32-channel spine coil receive-array. The parameters of the ufSSFP sequence were as follows: TE/TR/TA/TW =

0.61/1.36/100/170 ms, flip angle α = 36°, FOV = 450×450 mm^2, matrix = 128×128, 200 images per slice, slice thickness = 12 mm, bandwidth = 2055 Hz/px, GRAPPA factor 3.

2.2.3 Image post-processing and analysis

Respiratory motion in time-resolved ufSSFP data was compensated with a two-dimensional non-rigid image registration algorithm [130]. Vw and Qw images were created by integration of respiratory and cardiac spectral lines obtained after Fourier analysis of the registered data. The non-rigid registration algorithm as well as Fourier decomposition routine was implemented in a dedicated software program (fMRLung 4.5, Siemens Corporate Research, Princeton, NJ). A general description of image post-processing can be found in Bauman et al [102].

Subsequently, the lung parenchyma was segmented in both lungs separately with exclusion of large vessels using a region growing algorithm [131] (see Figure 2.2). Segmentation masks were propagated along the temporal dimension of the registered data sets for calculation of the mean signal intensity in each time frame. Furthermore, the mean over time μ_t(SI) as well as the standard deviation over time σ_t(SI) from the averaged signal intensity in the segmented region were computed. The standard deviation σ_t(SI) reflects the sensitivity of the FD-MRI technique for detection of signal fluctuations caused by physiological processes, i.e., cardiac cycle in breath-hold acquisitions. Dedicated software (The Medical Imaging Interaction Toolkit 2014.03.0, Heidelberg, Germany) was used for the segmentation. The signal intensity analysis and visualization of the data was performed using Python 2.7 (Anaconda Python distribution, Continuum Analytics, version 2.0).

2.3 Results

Illustrative cuts of 2D coronal chest images acquired at 1.5T with a FD adapted ufSSFP sequence are shown in Figure 2.2. From the short TR of 1.46 ms used, essentially no banding is present within the lung parenchyma. For a flip angle of α = 50°, as compared to α = 25°, lung tissue signal increases by about 66% from 29 ± 1 [a.u.] to 48 ± 1 [a.u.] (see Fig. 2.2a). Similarly, an increase in TW between subsequent image acquisitions from 0 ms to 280 ms increases the signal in the lung parenchyma by almost 100% from 28 ± 1 [a.u.] to 54 ± 1 [a.u.] (Fig. 2.2b). Generally, delays (TW) allow for partial recovery of the magnetization and for inflow of fresh blood in the slice being imaged. Moreover, the implementation of a reversed RF pulse ramp (see Fig. 2.1) at the end of the ufSSFP acquisition block resulted in a further slight increase in the signal intensity of the lung parenchyma by about 14% from 42 ± 1 [a.u.] to 48 ± 1 [a.u.].

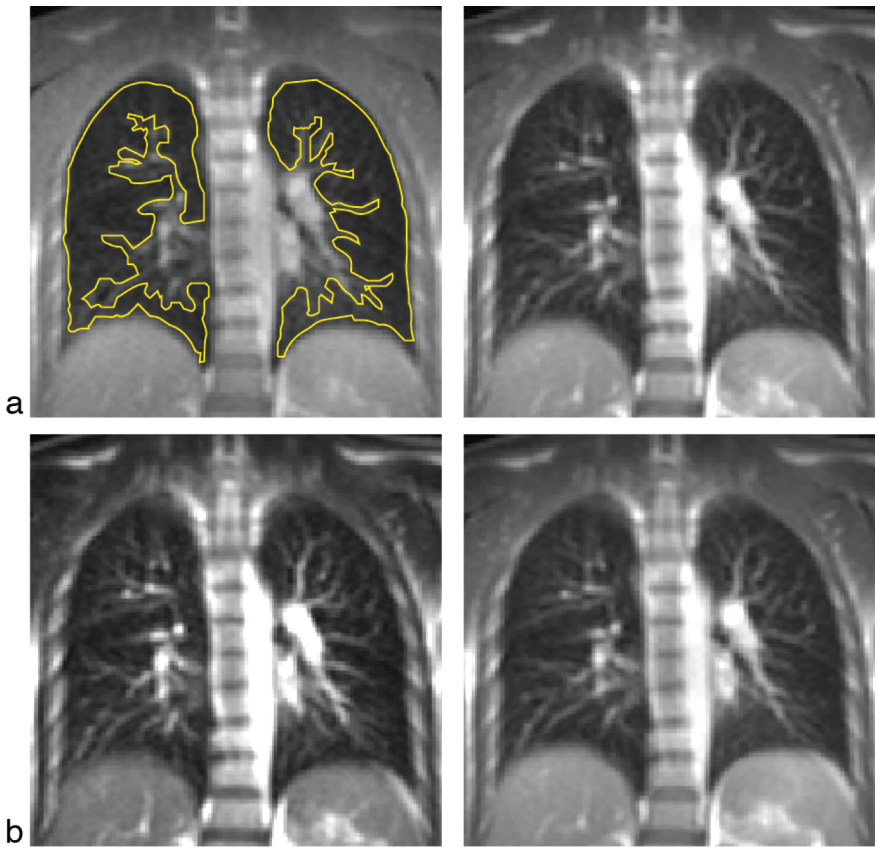

Figure 2.2. (a) Time-resolved 2D ufSSFP coronal sample images of the chest acquired at 1.5T in an expiratory breath hold for two different flip angle values α = 25° (left) and α = 50° (right). Other sequence parameters were: TE/TR/TA/TW = 0.67/1.46/110/180 ms and RF pulse length τ = 360 µs, resolution = 3.5 × 3.5 mm^2 (128 × 128 matrix). (b) Coronal sample images acquired with a fixed flip angle α = 60° but using different time interval values (TW) between consecutive image acquisitions: 0 ms (left) and 280 ms (right). Regions of interest for the assessment of parenchymal signal intensity are indicated by the yellow outline.

For optimization purposes, the mean signal intensity, μ_t(SI), in the lung parenchyma and its variation over time, σ_t(SI), are now analyzed in detail as a function of the flip angle α, the time interval TW between consecutive images, the RF pulse length τ, as well as the spatial resolution (see Fig. 2.3).

As can be expected, the lung signal as well as the sensitivity for detection of signal fluctuations increases with increasing flip angle (see Fig. 2.3a) but starts to level off only for $\alpha \approx$ 60-65°. For the chosen waiting time (TW = 180 ms) and pulse length (τ = 360 µs), any further increase in the flip angle, however, is limited due to SAR. Similarly, the simulation of the SSFP behavior in the transient state of the magnetization shows an increase in the signal with increasing the flip angle. A similar strong influence on the parenchymal signal level is found for TW (see Fig. 2.3b). Within the accessible range (for appropriate sampling of the cardiac frequency, 3 to 4 images per second

need to be acquired), a near linear relationship is observed. Almost no effect of the TW length on σ_t(SI) was measured. Thus, TW should be chosen to be maximal.

The mean signal intensity over time maximizes for RF pulse lengths (τ) around 350–400 µs (see Fig. 2.3c), whereas the standard variation over time increases with a prolongation of the RF duration (see Fig. 2.3c). A pulse length of 360 µs was chosen, providing flip angle settings within the optimal range (see Fig. 2.3a).

As can be expected, the lung signal intensity decreases with increasing resolution (see Fig. 2.3d): for example, for an increase in the matrix size from 96×96 to 176×176, μ_t(SI) decreases from 57 ± 2 [a.u] to 36 ± 1 [a.u]. Similarly, as a result of the prolonged image acquisition times and reduced waiting times (TW), σ_t(SI) decreases with increasing spatial resolution.

Contemporary bSSFP FD imaging, performed with an in-plane resolution of 3.5×3.5 mm^2 for a matrix size of 128×128 [123], is now compared to FD imaging using an optimal ufSSFP setup, and the corresponding results are shown in Fig. 2.4. Residual banding artifacts, especially in regions near spine, ribs and mediastinum persist with bSSFP, resulting in local defects in Vw and Qw images (as indicated in Fig. 2.4a). This is in contrast to ufSSFP imaging, where no residual banding can be perceived (Fig. 2.4b). For healthy lung tissue, this essentially results in artifact-free Vw and Qw images of notable homogeneous intensity. As compared to bSSFP, lung tissue signal from ufSSFP signal was increased by 21%: the mean signal intensity and corresponding standard deviation in free breathing acquisitions was: 34 ± 4 for bSSFP and 41 ± 3 for ufSSFP. As demonstrated

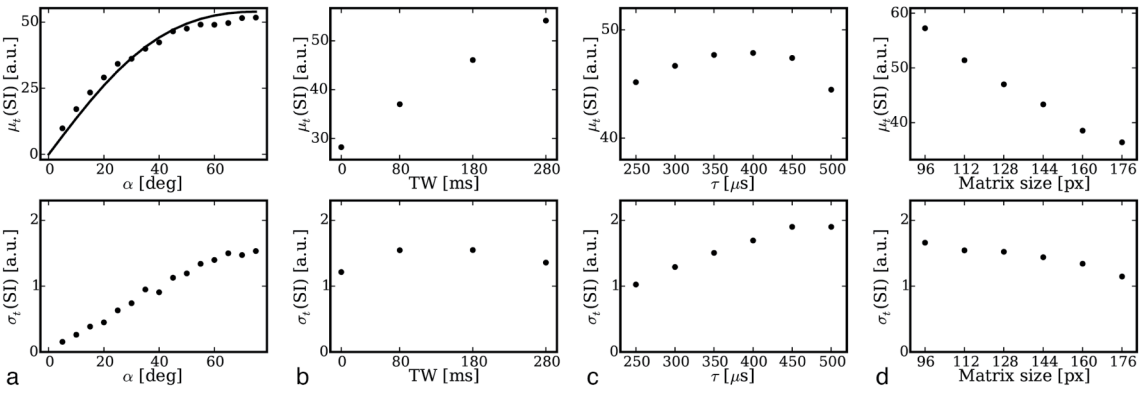

Figure 2.3. The diagrams present measurements of the mean signal intensity over time µt(SI) (top row) and the standard deviation over time σt(SI) (bottom row) in the lung parenchyma (for definition of ROI, see Fig. 2.2a) of a healthy volunteer in expiration at 1.5T using the 2D+t ufSSFP imaging as a function of the flip angle and signal intensity values obtained from the numerical simulation of the signal behavior (a), the time interval (TW) between consecutive image acquisitions (b), the RF pulse length τ (c), and the matrix size (d). The standard deviation over time estimated in the lung parenchyma reflects the sensitivity of the FD technique for detection of signal modulations mainly induced by blood pulsation in the data acquired in breath hold.

in Fig. 2.4c, fat-saturation (FS) can be applied without notable lung tissue signal loss (38 ± 4 [a.u.]). Despite the methodological advances of ufSSFP, FD imaging is still problematic at 3T (see Fig. 2.4d) as a result of pronounced banding artifacts and overall reduced signal levels in the lung parenchyma (16 ± 2 [a.u.]) due to SAR constraints requiring considerably lower flip angles (see also Fig. 2.3a).

From the increased lung signal in the FD adapted ufSSFP sequence at 1.5T (19 ± 5% measured for five volunteers) in combination with the reduced TR (~23%), FD-MRI of the lung can be performed with increased spatial resolution. Native ufSSFP images acquired at 1.5T and corresponding Vw and Qw images are shown in Fig. 2.5 for three different spatial resolutions of 4.0×4.0 mm^2, 3.5×3.5 mm^2, and 2.8×2.8 mm^2.

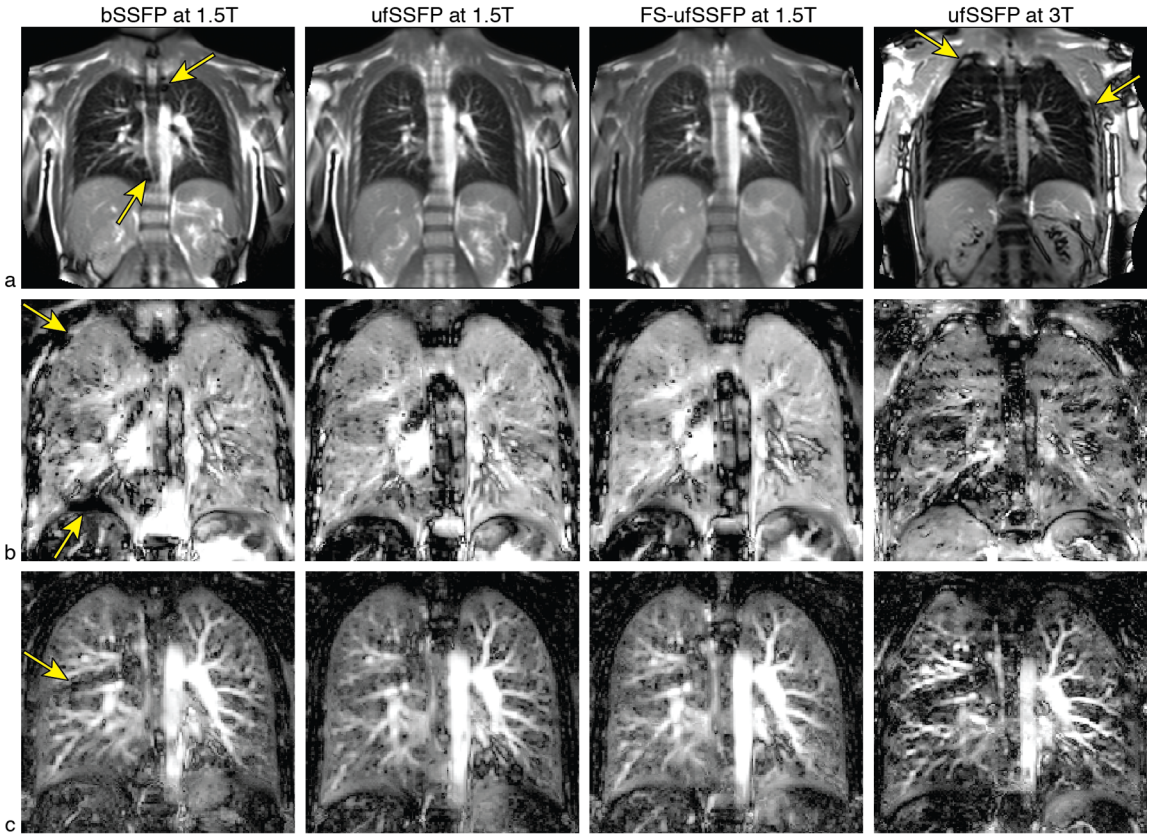

Figure 2.4. Illustrative 2D FD ufSSFP imaging results at 1.5T in a healthy volunteer: (a) native ufSSFP images of the chest from time resolved data sets, (b) ventilation-weighted and (c) perfusion-weighted images. Yellow arrows indicate location of the banding artifacts. Imaging sequence parameters at 1.5T were: TE/TR/TA/TW = 0.87/1.9/110/180, and α = 75°, for standard bSSFP; TE/TR/TA/TW = 0.67/1.46/110/180 ms and α = 65° for ufSSFP; TE/TR/TA/TW = 0.67/1.46/110/170 ms and α = 65° for ufSSFP with fat saturation (FS-ufSSFP); and TE/TR/TA/TW = 0.61/1.36/100/170 ms and α = 26° with ufSSFP at 3T. The in-plane resolution and matrix of the presented images were 3.5 × 3.5 mm^2 and 128 × 128, respectively.

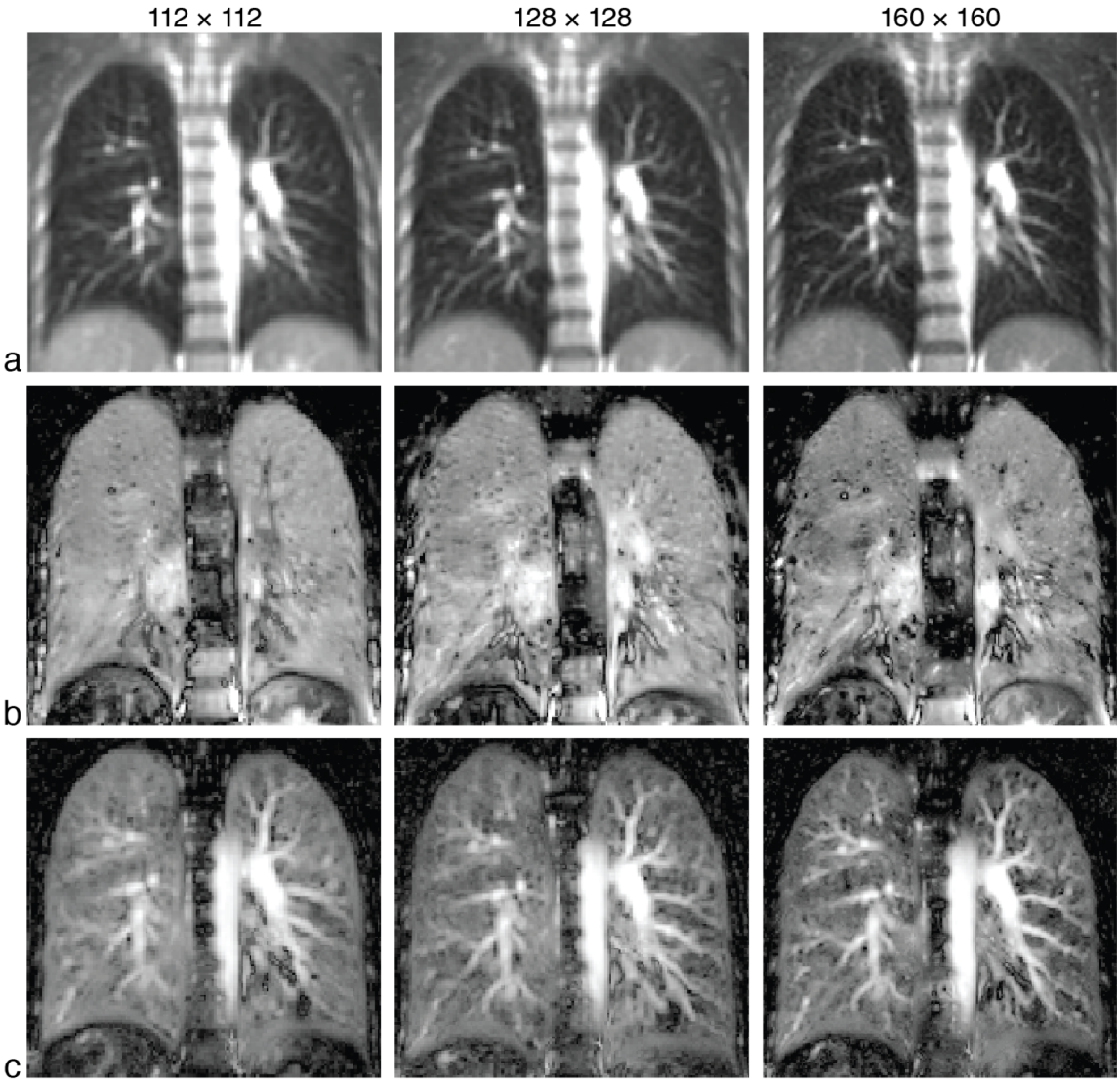

Figure 2.5. Native ufSSFP images (a) obtained (from left to right) with following matrix sizes, spatial resolutions and imaging parameters: 112 × 112 (4.0 × 4.0 mm^2), TE/TR/TA/TW = 0.64/1.41/90/195 ms; 128 × 128 (3.5 × 3.5 mm^2), TE/TR/TA/TW = 0.67/1.46/110/180 ms; and 160 × 160 (2.8 × 2.8 mm^2), TE/TR/TA/TW = 0.73/1.55/140/150 ms, as well as the corresponding ventilation-weighted (b) and perfusion-weighted (c) images.

2.4 Discussion

In this work, the recently proposed ufSSFP framework was adapted and optimized for FD-MRI. The major benefits from ufSSFP as compared to standard bSSFP used in previous FD-MRI studies mainly originate from minimal TR times that can be achieved by pushing the sequence building blocks to the hardware limits of the MR scanner. The reduction in TR by 23% (from 1.90 ms to 1.46 ms for the standard matrix size of 128×128) resulted in an overall decrease of banding artifacts and image acquisition time used to reduce the parallel imaging acceleration factor from 3 to 2. Furthermore, the decreased TE/TR times in combination with a reversed linear RF pulse ramp at the end of the image acquisition block implemented in the ufSSFP pulse sequence resulted in markedly improved signal intensities in the lung tissue (~ 19%) and successfully mitigated banding issues at 1. 5T. Eddy currents and pulsation artifacts were reduced by a linear reordering *k*-space acquisition scheme.

Generally, a compromise between ufSSFP FD imaging parameters is required in order to maintain both a sufficient high sampling rate for respiratory and cardiac cycles and appropriate SNR from the lung parenchyma. To this end, the imaging parameters including flip angle, waiting time, RF pulse duration and spatial resolution were optimized in order to achieve both the maximal possible signal intensity in the lung tissue as well as the sensitivity of FD-MRI to detect signal variations caused by physiological cycles. In the experiments performed in healthy volunteers we kept a constant field-of-view of 450×450 mm^2 and a frame rate of 3.33 images per second. Nevertheless, parameters such as field-of-view, acquisition matrix and waiting time should to be adapted for the specific patient group. Pediatric patients may require smaller field-of-view or increased spatial resolution. We have shown that the decreased ufSSFP acquisition time can be traded for an increase of the spatial resolution up to 2.8×2.8 mm^2, without notable quality loss in the derived functional lung images; even in adults. In contrast, reduced spatial resolution can be used for diseases heavily affecting the density of the lung parenchyma, such as emphysema or COPD. The optional fat saturation pulse implemented prior the image acquisition block may prove useful in obese patients or in presence of lesions containing fatty tissue.

After optimization, the ufSSFP pulse sequence provided functional Vw and Qw images of increased homogeneity across the lung tissue in the healthy volunteers at 1.5T. Despite the significant improvements in the image quality at 1.5T, the application of the ufSSFP pulse sequence for FD-MRI at 3T still appears problematic. Major limitations arise from SAR, which reduces the maximal achievable flip angle, as well as increased susceptibility effects, resulting in more severe banding. As a result, functional lung images obtained at 3T using ufSSFP FD-MRI are of markedly inferior quality as compared to 1.5T. Unfortunately, the achievable TR is not short

enough to reduce the banding artifacts to an acceptable level, and from hardware limitations, no further reduction in TR can be currently achieved. As an alternative, the application of the spoiled gradient echo sequence for FD-MRI was recently proposed [132].

2.5 Conclusion

In this work, we adapted and optimized the recently proposed ufSSFP scheme for FD-MRI of the lung at 1.5T. The optimized ufSSFP sequence profits from the overall reduced TR values and improves the image quality by increasing the signal intensity in the lung tissue while reducing the amount of banding artifacts at 1.5T. In addition, ufSSFP offers the possibility to acquire functional lung data with higher spatial resolution as compared to standard bSSFP imaging used in previous FD-MRI studies, which can lead to an increased sensitivity for the detection of functional lung pathologies.

CHAPTER 3

Rapid three-dimensional in vivo ^{1}H human lung respiratory imaging at 1.5T using ultra-fast balanced steady-state free precession

A modified version of this chapter has been published as:

Pusterla O, Bauman G, Wielpütz MO, Nyilas S, Latzin P, Heussel CP, Bieri O. *Rapid 3D in vivo ^{1}H human lung respiratory imaging at 1.5 T using ultra-fast balanced steady-state free precession.* Magn Reson Med, 2017, 78:1059–1069.

CHAPTER ABSTRACT

Purpose: To introduce a reproducible non-enhanced 1H MRI method for rapid in vivo functional assessment of the whole lung at 1.5T.

Methods: At different respiratory volumes, the pulmonary signal of ultra-fast steady-state free precession (ufSSFP) follows an adapted sponge model, characterized by a respiratory index α. From the model, α reflects local ventilation-related information, is virtually independent from the lung density and thus from the inspiratory phase and breathing amplitude. Respiratory α-mapping is evaluated for healthy volunteers and patients with obstructive lung disease from a set of five consecutive three-dimensional ufSSFP scans performed in breath-hold and at different inspiratory volumes. For the patients, α-maps were compared to CT, dynamic contrast-enhanced MRI (DCE-MRI) and Fourier decomposition (FD).

Results: In healthy volunteers, respiratory α-maps showed good reproducibility and were homogeneous on iso-gravitational planes but showed a gravity-dependent respiratory gradient. In patients with obstructive pulmonary disease, the functional impairment observed in respiratory α-maps was associated with emphysematous regions present on CT images, perfusion defects observable on DCE-MRI, and impairments visualized on FD ventilation and perfusion maps.

Conclusion: Respiratory α-mapping derived from multi-volumetric ufSSFP provides insights into functional lung impairment and may serve as a reproducible and normative measure for clinical studies.

3.1 Introduction

Periodical bidirectional airflow is the primary process taking place in the lung, enabling gas exchange in the alveoli [57]. As a result, the measurement of both global and local ventilation is a key parameter not only to diagnose and understand pathophysiology in lung diseases, but also for monitoring the progression and the response to therapeutic procedures [11].

A global measure of lung ventilation can be obtained by conventional whole-lung spirometry, plethysmography or multiple-breath washout tests [7]. The strength of these pulmonary function tests (PFTs) relies on their low costs and in the standardization of normative results (e.g., gender, body size, age) for a comparison of disease severity and progression. Conventional PFTs, however, cannot provide information about regional lung processes which add fundamental insights into pathophysiologic mechanisms or improve therapies by tailoring to specific lung regions and disease phenotypes [10, 11].

A broad spectrum of imaging modalities is available to assess the regional lung ventilation. Single-photon emission computed tomography (SPECT), planar scintigraphy and positron emission tomography (PET) are nuclear medicine imaging modalities based on radioactive-labeled tracer administration. Despite their relatively poor spatial and temporal resolution, SPECT and PET are commonly used in clinical routine for lung functional imaging [16]. More recently, xenon-enhanced dual-energy computed tomography (CT) [133] and the novel four-dimensional CT [134, 135] have been shown to provide high spatial resolution ventilation imaging in short scanning times. Despite the constant progress of nuclear medicine and CT in reducing radiation doses, exposure to any ionizing radiation is still of concern [22, 23]; especially for children, pregnant women, or patients who require frequent follow-up examinations [25].

Alternatively, magnetic resonance imaging (MRI) is an attractive radiation-free imaging modality, and over the last decade a variety of powerful methods have been developed for the evaluation of both lung morphology and function. Among them, for the assessment of pulmonary perfusion and indirectly evaluate lung respiratory obstructions [75, 136], dynamic contrast-enhanced (DCE) MRI is a well-established technique [4, 29], but it requires the injection of contrast agents. For ventilation assessment, non-proton based lung imaging with hyperpolarized (HP) noble gases, such as Helium-3 or Xenon-129, has demonstrated the ability to measure various pulmonary functional biomarkers [35]; furthermore, pulmonary ventilation can be visualized in MRI using inert fluorinated gas tracers which have recently generated high quality images similar to those from HP gases [36]. As it requires specific equipment, broad clinical roll out of gas ventilation MRI is challenging, requiring a dedicated commitment.

In contrast, non-invasive, proton-based imaging of regional lung function is possible in vivo using a technique known as Fourier decomposition (FD) [102] MRI. This approach, although relatively new, was already validated in animal and human studies [105, 106, 123]. FD utilizes dynamic balanced steady state free precession (bSSFP) imaging in free-breathing with subsequent image registration and voxel-wise spectral analysis to extract local ventilation and perfusion information. Nevertheless, due to the required time-resolution to separate perfusion from ventilation, FD-MRI is a single slice method. As a result, a stack of coronal two-dimensional (2D) slices must be acquired to cover the whole lung volume, thus offering relatively low through plane resolution.

In this work, we introduce a novel proton-based and contrast-agent-free MRI technique which provides regional isotropic three-dimensional information related to pulmonary ventilation [137]. The method acquires a range of 3D ultra-fast balanced steady state free precession (ufSSFP) [45] chest scans at different inspiratory volumes (multi-volume 3D MRI) to derive a new volumetric lung functional measure termed respiratory index α. The new method is evaluated at 1.5T in healthy volunteers and in obstructive pulmonary disease patients. For the patients, respiratory α-mapping is compared to dynamic contrast-enhanced MRI (DCE-MRI), FD-MRI and computed tomography (CT).

3.2 Theory

3.2.1 The adapted sponge model and the respiratory α-index

The lung parenchyma can be compared mechanically to sponge-like tissue, which periodically expands and contracts following the movement of the diaphragm and chest walls, resulting in bidirectional air flow and ventilation.

In a simple dry sponge model [138] where the sponge mass is constant, the signal intensity (SI) is inversely-proportional to the lung volume V:

$$\mathrm{SI}(V) = \Lambda \cdot V^{-1} + \eta \tag{3.1}$$

where Λ is a signal intensity scaling factor (related to parenchymal "mass"), and η is the SI in the limit of infinite volume, i.e., noise. The assumption of mass preservation in the dry sponge model, however, is not precise enough to model the lung mechanics [138, 139] due to physiological

changes, such as the variability of blood volume during breathing [71], or due to ventilation inhomogeneities or regional abnormalities. As a result, Equation (3.1) needs to be modified to take the form

$$\mathrm{SI}(V) \;=\; \Lambda \cdot V^{-\alpha} \;+\eta \tag{3.2}$$

where α is referred to as respiratory index, which maps lung expansion and changes in pulmonary blood volume during breathing.

In the limit of $\eta \ll \Lambda \cdot V^{-\alpha}$, the adapted sponge model [cf. Eq. (3.2)] can be rewritten to yield

$$\log(\mathrm{SI}) \;=\; \log\left(\Lambda \cdot V^{-\alpha}\,(1+\frac{\eta}{\Lambda \cdot V^{-\alpha}})\right) \approx \log(\Lambda \cdot V^{-\alpha}) \;=\; \log(\Lambda) - \alpha \cdot \log(V) \tag{3.3}$$

and the respiratory index α can be estimated globally considering the mean SI over the whole lung volume, $\overline{\mathrm{SI}}$, using

$$\alpha_{\mathrm{global}} := -\frac{\partial(\log(\overline{\mathrm{SI}}))}{\partial\big(\log(V)\big)}\,. \tag{3.4}$$

Similarly, after co-registration of multi-volumetric acquisitions using a deformable registration algorithm, the respiratory index can be estimated voxel-wise (i.e., locally at the position $\vec{x}$)

$$\alpha_{\mathrm{local}}(\vec{x}) := -\frac{\partial\left(\log\big(\mathrm{SI}(\vec{x})\big)\right)}{\partial(\log(V))}\,. \tag{3.5}$$

3.2.2 The respiratory α-index: theoretical formulation and interpretation

In the following, we consider a physical pulmonary model in which the main components of the lung are parenchyma (tissue), blood and air.

During breathing the whole lung volume *V* continuously increases or decreases, allowing for airflow. For small enough variations in the total lung volume, $V \;=\; V_0 \pm \delta V$, the average density in the lung ($\overline{\rho}$) is assumed to become a function of the global variations only, i.e.,

$$\overline{\rho}(V) := \frac{M_{\mathrm{blood}}(V) + M_{\mathrm{air}}(V) + M_{\mathrm{tissue}}}{V} \approx \frac{\rho_{\mathrm{blood}} \cdot V_{\mathrm{blood}}(V) + \overline{\rho}_{\mathrm{tissue}} \cdot V_{\mathrm{tissue}}}{V} \tag{3.6}$$

where $\mathrm{V} \;=\; \mathrm{V}_{\mathrm{blood}} + \mathrm{V}_{\mathrm{air}} + \mathrm{V}_{\mathrm{tissue}}$, ρ_{blood} is constant, $\overline{\rho}_{\mathrm{tissue}}$ is the average tissue density, and where we neglected the contribution of the air to the mass, since $\mathrm{M}_{\mathrm{air}} << \mathrm{M}_{\mathrm{blood}}, \mathrm{M}_{\mathrm{tissue}}$.

Similarly, if ventilated, the volume of a small macroscopic region, $v = v(\vec{x})$, expands or compresses due to air inflow or outflow. For example, while the region inflates, the volume of air (v_{air}) increases, the tissue in the region stretches (but preserves its mass), and the blood volume (v_{blood}) might be altered due to physiological changes. Analogous to Equation (3.6), we assume that for small enough variations in the total lung volume the local volume changes become a function of the global variations only, i.e., $v = v(\vec{x}, V)$. Thus, the local density becomes,

$$\rho(\vec{x}, V) := \frac{m_{\text{blood}}(\vec{x}, V) + m_{\text{air}}(\vec{x}, V) + m_{\text{tissue}}(\vec{x})}{v(\vec{x}, V)} \approx$$

$$\approx \frac{\rho_{\text{blood}} \cdot v_{\text{blood}}(\vec{x}, V) + \rho_{\text{tissue}}(\vec{x}) \cdot v_{\text{tissue}}(\vec{x})}{v(\vec{x}, V)} \tag{3.7}$$

where again, we neglect the contribution of the air to the local mass.

Provided that there is no or only a limited change in the lung T_2/T_1 during breathing, the change in the steady-state signal of multi-volumetric ufSSFP acquisitions, ΔSI, becomes proportional to the change in the proton density, $\Delta\rho_{MRI}$. From the model [cf. Eq. (3.6)], we thus find for the global index:

$$\alpha_{\text{global}}(V_0) \approx -\left.\frac{\partial \log\left(\bar{\rho}(V)\right)}{\partial \log(V)}\right|_{V = V_0} = 1 - \frac{V_0}{M_0} \cdot \left.\frac{\partial M_{\text{blood}}}{\partial V}\right|_{V = V_0} \tag{3.8}$$

where the second term reflects the change in whole pulmonary blood mass as a function of the whole lung volume (note $\frac{V_0}{M_0}$ is simply a scaling factor and $M_0 := M(V_0)$). Simulations indicate that α_{global} is almost independent of the breathing position, V_0, that is $\left|1 - \frac{\alpha_{\text{global}}(V+\delta V)}{\alpha_{\text{global}}(V-\delta V)}\right| < 0.03$ for variations up to $\delta V = \frac{V_0}{6}$ (tidal breathing, e.g., 2.4±0.4 L), and $\left|\frac{\partial M_{\text{blood}}}{\partial V}\right| < 0.25 \cdot \frac{M_0}{V_0}$ (value elaborated from [71] assuming healthy tissues and $M_{\text{tissue}} = M_{\text{blood}}(V_0)$).

From Equation (3.8), α_{global} measures the change in lung perfusion as a function of the whole lung volume change (e.g., percentage of whole lung mass change divided by the percentage of the total lung volume change). Thus, $\alpha_{\text{global}} = 1$ indicates no perfusion change, $\alpha_{\text{global}} > 1$ means that the blood decreases in inspiration and $\alpha_{\text{global}} < 1$ the opposite.

In analogy, for the local respiratory index [cf. Eq. (3.5)], we find using Eq. (3.7)

$$\alpha_{\text{local}}\big(v(\vec{x},V_0)\big) \approx -\left.\frac{\partial \log\big(\rho(\vec{x},V)\big)}{\partial \log(V)}\right|_{V=V_0} =$$

$$= \frac{V_0}{v(\vec{x},V_0)} \cdot \left.\frac{\partial v(\vec{x},V)}{\partial V}\right|_{V=V_0} - \frac{V_0}{m(\vec{x},V_0)} \cdot \left.\frac{\partial m_{\text{blood}}(\vec{x},V)}{\partial V}\right|_{V=V_0}. \tag{3.9}$$

From Equation (3.9), the local respiratory index depends on two main components: the first differential term reflects the local change in volume as a function of the total lung volume change, thus local ventilation, whereas the second differential term describes the change in the local lung mass (i.e., pulmonary blood volume) as a function of the total lung volume change. Note, that in Equation (3.9), the terms $V_0/v(\vec{x},V_0)$ and $V_0/m(\vec{x},V_0)$ are scaling factors.

If the second term in Equation (3.9) fulfills

$$\frac{V_0}{m(\vec{x},V_0)} \cdot \left.\frac{\partial m_{\text{blood}}(\vec{x},V)}{\partial V}\right|_{V=V_0} \ll \frac{V_0}{v(\vec{x},V_0)} \cdot \left.\frac{\partial v(\vec{x},V)}{\partial V}\right|_{V=V_0} \tag{3.10}$$

the respiratory index becomes a measure of local ventilation (e.g., percentage of the local volume change divided by the percentage of the total lung volume change),

$$\alpha_{\text{local}}\big(v(\vec{x},V_0)\big) \approx \frac{V_0}{v(\vec{x},V_0)} \cdot \left.\frac{\partial v(\vec{x},V)}{\partial V}\right|_{V=V_0}. \tag{3.11}$$

The premise of Equation (3.10) has already been assumed by other ventilation-weighted imaging techniques [102, 112, 123, 134, 140] and is corroborated by recent findings [71, 141] which show a not statistically significant pulmonary perfusion change over the whole lung and no significant lobar perfusion redistribution for breath-holds in the tidal volume region. As a result, the respiratory index $\alpha_{\text{local}}(\vec{x})$ reflects virtually lung ventilation and is independent of the lung density [see Eq. (3.11)]. A value $\alpha_{\text{local}}(\vec{x}) = 1$ indicates that a region-of-interest (ROI) expands equally to the whole lung, $\alpha_{\text{local}}(\vec{x}) > 1$ that the ROI expands at a rate higher than the whole lung, and $\alpha_{\text{local}}(\vec{x}) < 1$ the opposite.

3.3 Methods

3.3.1 MRI data acquisition

All datasets were acquired with 1.5T clinical whole-body MR-scanner (Siemens Healthineers, Erlangen, Germany). A 12-channel thorax and a 24-channel spine coil were used as receive-array; the body coil as transmitter. Measurements were performed in a total of ten healthy volunteers and three patients; written informed consent was obtained from each subject prior to the examinations.

Images were acquired in breath-hold and in supine position using a 3D balanced ufSSFP sequence, offering a T_2/T_1 weighted contrast for TR < 2 ms at 1.5T [45] and sensitive enough to depict the signal intensity modulations of the lung parenchyma arising at diverse inspiratory levels [137]. For the healthy volunteers, the sequence parameters were set as follows: TE/TR = 0.47/1.19 ms, flip angle 23° (optimized for highest ufSSFP lung signal intensity, see Eq. (3.1) in [117] for details), RF pulse length 80 µs, bandwidth 1563 Hz/pixel, field-of-view 400 × 400 × 250 mm^3, two averages, isotropic resolution 3.1 mm^3, reconstruction matrix 128 × 128 × 80, parallel imaging GRAPPA factor 2 (phase encoding R-L), phase oversampling 30%, asymmetric echo readout (66% of full echo), total acquisition time 16 s. The protocol was shortened to 11 s for the patients: field-of-view 450 × 450 × 250 mm^3, isotropic resolution 3.5 mm^3, reconstruction matrix 128 × 128 × 72, no phase oversampling and otherwise equal protocol parameters as for the volunteers. In all the acquisitions predefined default shim settings (tune up) were used. An in depth description of the ufSSFP pulse sequence and technical details can be found in Bieri [45].

3.3.2 The adapted sponge model

In order to validate the adapted sponge model [Eq. (3.2)], 3D ufSSFP imaging of the lung was performed from forced expiration (i.e., residual volume, RV) to forced inspiration (i.e., total lung capacity, TLC) in five healthy volunteers (30 ± 4 years old, males). Typically, around 14 scans in inspiratory breath-hold were recorded. The breathing commands were given vocally to the volunteers, which were instructed to change their breathing position for each of the 14 scans (from RV to TLC).

For the post-processing, the acquisitions were median filtered (filter kernel size 5 × 5 × 5 voxels) to remove the vasculature overlaying the pulmonary tissue, in particular vessels smaller than 4 × 4 × 4 voxels [142]. The lungs were segmented using a 3D fast-marching algorithm using a standalone software (MITK) [131]. The consistency of the segmentation was verified slice-by-

slice and in between datasets by a trained observer; if needed, the regions-of-interest were corrected manually. From this, the volume of the lung and the corresponding mean signal intensity in each acquisition was calculated. Finally, the global respiratory index α_{global} was calculated by fitting the observed mean signal intensity in the lung parenchyma as a function of the lung volume to the adapted sponge model [Eq. (3.2)]. Fitting was performed by orthogonal regression (singular value decomposition).
Data visualization and post-processing was performed using Python 2.7 (Anaconda Python distribution, Continuum Analytics, version 2.5).

3.3.3 Respiratory α-mapping

Respiratory α-mapping [Eq. (3.5)] was evaluated in ten healthy volunteers (36 ± 6 years old, four females and six males), five of which were already scanned for the adapted sponge model protocol. Respiratory α-mapping was also performed in three patients with obstructive pulmonary disease: two chronic obstructive pulmonary disease (COPD) GOLD III (53 year old male and 75 year old female) and a pediatric patient with cystic fibrosis (CF) (12 year old, female). For the COPD patients, respiratory α-mapping was compared with clinically indicated CT and DCE-MRI, which were acquired the same day for emphysema treatment planning. The CT acquisitions were post-processed with the software YACTA (programmed by Oliver Weinheimer, Heidelberg, Germany) [143] to generate color-coded emphysema maps. For the pediatric CF patient, respiratory α-maps were compared to the functional information derived from FD [104, 144]. To this end, time-resolved sets of coronal images were acquired in free-breathing using TE/TR = 0.68/1.54, flip angle 60°, field-of-view 400 × 400 mm^2, matrix 128 × 128 (interpolated to 256 × 256), slice thickness 12 mm, bandwidth 2056 Hz/pixel, GRAPPA factor 2, imaging rate 4 images/s, 160 images per set, for an acquisition time of 40 s / slice.

The scanning protocol for the calculation of respiratory α-maps, in contrast to the 14 MR scans performed to validate the adapted sponge model (cf. “Adapted Sponge Model”, Section 3.2.1), consisted of only five 3D ufSSFP lung acquisitions. The acquisitions were recorded at different breathing positions around the tidal respiratory volume region, generally from functional residual capacity (FRC) to tidal inspiration. To this end, the volunteers and patients were instructed either to “breathe-in, breathe-out, and hold” or to “breathe-in and hold” before the respective FRC and tidal inspiration acquisitions. The three scans in respiratory phases in between FRC and tidal inspiration were performed with the following breathing commands: “breathe-in, breathe-out, one-sip / two-sips / three-sips of air, and hold”, respectively.

Scanning in the tidal breathing region facilitated the spatial co-registration of the limited volume differences. The co-registration was performed using a 3D deformable B-spline mass preserving

image registration algorithm implemented in elastix (elastix version 4.7, University Medical Center Utrecht, The Netherlands) [145]. The registration algorithm aims at aligning dense and high signal intensity landmarks of images, such as lung vessels and chest cage. For the registration, the scan with a mean value of the lung volume was chosen as a fixed dataset (baseline) and the remaining four, so-called "moving" datasets were co-registered. After registration, the images were median-filtered and the respiratory index α_{local} was calculated voxel-wise by orthogonal regression estimation of the observed SI as function of the lung volume, cf. Equation (3.5). The lung volume of each scan was determined on native datasets (unregistered) by segmentation, as described above.

3.3.4 Reproducibility

The reproducibility of respiratory α-mapping was assessed in three healthy volunteers. Each subject was scanned three times, but taken out and repositioned to mimic and enforce new measurement conditions (including the frequency adjustments). The resulting three respiratory α-maps of each subject were spatially matched by co-registration (elastix) in order to assess the local variability. As a global measure, the gamma-index percent passing rate [146] was calculated to assess the voxel-to-voxel similarity between the maps over the whole lung. The gamma-index percent passing rate was derived with acceptance criteria of 5% for the respiratory α-index deviation and a physical distance to agreement of 10 mm. In contrast to a relative difference analysis, the gamma-index tolerates spatial and structural misalignments caused by differences in the lung volume of the baseline datasets (used to calculate the respiratory α-maps).

3.4 Results

3.4.1 Validation of the adapted sponge model

Exemplary 3D ufSSFP images obtained in a healthy volunteer are shown in Figure 3.1a for two different inspiratory volumes (i.e., 1.8 L and 4.6 L). As a result of the very short TR, no banding artifacts are visible and airways are well visualized in the native images. The difference in signal levels in the lung parenchyma for the two lung volumes are clearly noticeable; especially in the dependent (dorsal) part of the lung. Median filtering, as shown in Figure 3.1b, is used to remove the overlying vascular structure while preserving the underlying pulmonary signal variation [142].

The observed mean parenchymal signal intensity variation (over the whole lung; see yellow outlines in Figure 3.1 for definition of the region-of-interest) is shown in Figure 3.2 as a function of lung volumes. The overall SI variation of the lung parenchyma was as low as 36 [a.u.] in forced inspiration (V = 6.31 L) and increased about 4-fold, up to 147 [a.u.], in forced expiration (V = 1.92 L). This is in contrast to the SI in the liver, remaining constant (304±4 [a.u.], mean ± SD). In comparison to the signal intensity emanating from the lung parenchyma, a low noise level of about 5±2 [a.u.] was measured in air justifying the limit of $\eta \ll \Lambda \cdot V_L^{-\alpha}$ and thus the validity of Equation (3.3), especially for respiratory phases in the tidal breathing region. Overall, the signal variation follows the adapted sponge model [cf. Eq. (3.4)]. A fit of the adapted sponge model yields α_{global} = 1.16 ± 0.02 (mean ± uncertainty) in combination with a SI scaling factor Λ = 317 ± 7 [a.u.]. The small residual deviations of the experimental data from the linear fit in the double logarithmic scale corroborate the overall independency of the respiratory index α_{global} from the breathing phase. Moreover, a respiratory index α_{global} deviating from one indicates that the dry sponge model (α = 1) is not accurate in describing the lung SI modulations. Similar results are found for all five volunteers (cf. Table 3.1).

In summary, for lung volumes ranging from RV and TLC, the respiratory index α_{global} varied between 1.04 and 1.16 (uncertainty ±3%), indicating only residual contributions from blood changes [cf. Eq. (3.8)]. The orthogonal regression analysis yields coefficients of determinations R^2 higher than 0.996, demonstrating an appropriate description of the experimental data based on the adapted sponge model.

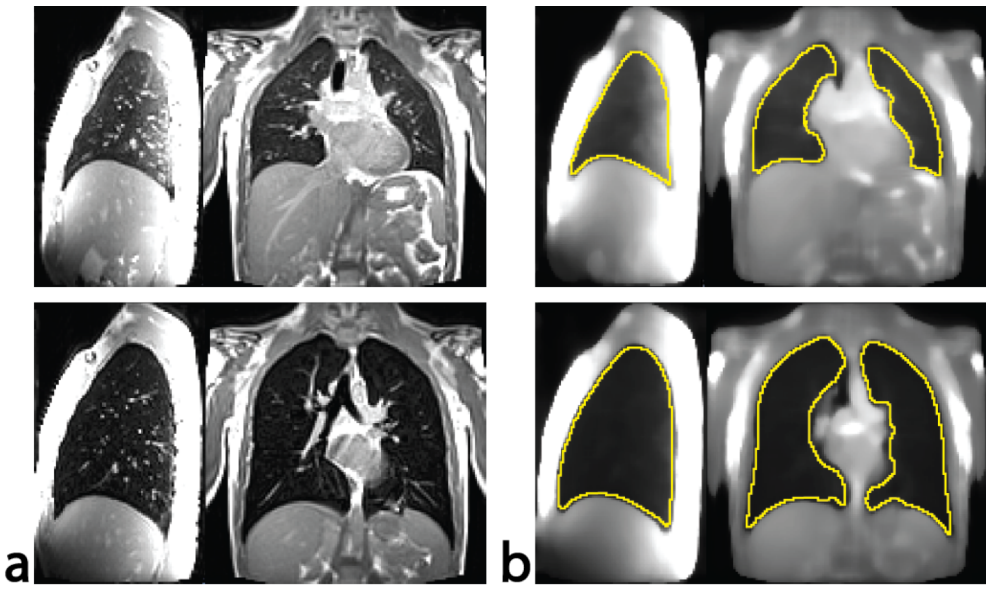

Figure 3.1. (a) Sagittal and coronal 3D ufSSFP chest images illustrating end-expiration (top) and full inspiration (bottom). (b) Median-filtered images with segmentation (yellow outline) used for estimation of parenchymal signal intensity and lung volume.

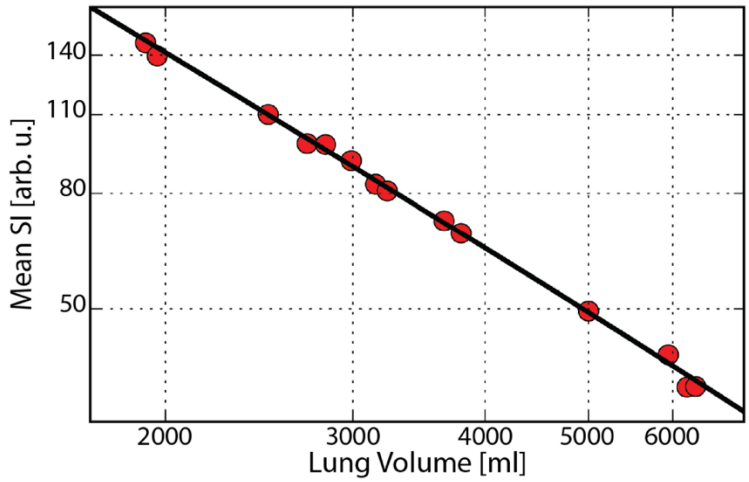

Figure 3.2. Measured mean signal intensity of the parenchyma (red dots) as a function of the lung volume in double logarithmic scale. A fit of the adapted sponge model (black line) yields α_{global} = 1.16±0.02 (cf. Table 3.1, Volunteer #1).

Table 3.1. Demographic information (gender, age, height, weight), global respiratory index (mean ± uncertainty), Pearson correlation coefficient (R^2) and lung volume (mean ± SD, min, max) for the subjects examined with the adapted sponge model protocol (lung volumes ranging from RV to TLC).

Subject	Gender, Age, Height (cm), Weight (kg)	α_{global}	R^2	Lung volume [L]		
				mean±SD	min	max
Volunteer 1	M, 32, 179, 82	1.16 ± 0.02	0.997	3.73 ± 1.52	1.92	6.31
Volunteer 2	M, 26, 190, 80	1.11 ± 0.03	0.997	3.67 ± 1.40	1.92	6.66
Volunteer 3	M, 34, 175, 80	1.14 ± 0.02	0.999	3.09 ± 0.91	1.47	5.32
Volunteer 4	M, 32, 178, 75	1.07 ± 0.03	0.996	4.38 ± 1.41	2.09	6.39
Volunteer 5	M, 28, 185, 84	1.04 ± 0.02	0.999	3.39 ± 1.09	1.85	5.53

3.4.2 Respiratory α-mapping in healthy subjects

From the respiratory mapping protocol, exemplary coronal views of the five native datasets acquired in a healthy volunteer at different inspiratory levels are shown in Figure 3.3a. The datasets are reordered as a function of the lung volume determined by segmentation, from FRC to tidal inspiration. For this range of volumes, the mean parenchyma SI varies from 102±42 [a.u.] (SI_{min} = 53 [a.u.], V = 2.71 L, FRC) to 72±21 [a.u.] (SI_{min} = 39 [a.u.], V = 3.78 L, tidal inspiration), while the noise level is about 4±2 [a.u.]. A global respiratory index α_{global} = 1.04±0.03 is recovered, similar to the value found by the adapted sponge model protocol (cf. Table 3.1, Volunteer #5, α_{global} = 1.04±0.02).

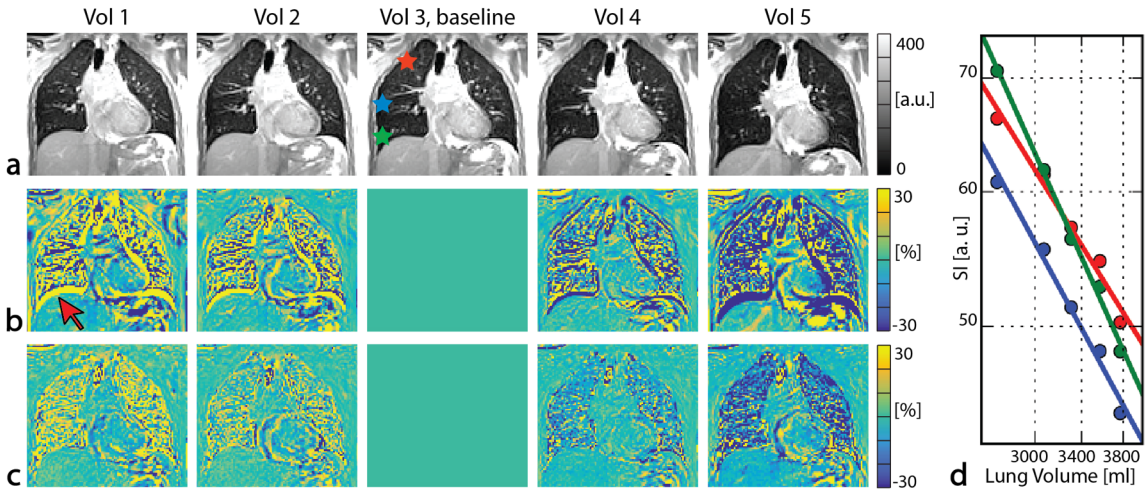

Figure 3.3. (a) Exemplary 3D ufSSFP coronal views of the same slice acquired at five different tidal volumes used for respiratory α-mapping. The datasets are ordered from left to right according to their lung volume (i.e., from FRC to tidal inspiration). The middle volume scan served as a baseline; i.e., was chosen as a reference image during the registration process. (b) Relative signal intensity difference maps between the baseline and the target images (to be registered) accentuating differences in the diaphragm position (e.g., red arrow), lung boundaries and arteries due to the respiratory phase mismatch. (c) Corresponding relative signal intensity difference maps after image co-registration, revealing lung structural alignment while preserving the signal intensity. (d) Local parenchymal signal (averaged over 4 × 4 × 4 voxels) as a function of the lung volume in double logarithmic scale for three selected ROI (for position of ROI, see (a), Vol 3). A fit of the adapted sponge model yields: $\alpha = 0.81\pm0.07$ (red line), $\alpha = 0.93\pm0.07$ (blue line) and $\alpha = 1.13\pm0.05$ (green line).

For better visualization of the rather marginal differences in the respiratory phases, relative signal intensity difference maps are calculated and shown in Figure 3.3b (with respect to the scan taken at middle respiratory phase). As a result, the diverse lung parenchyma signal levels, lung structural misalignments and through plane motion due to slightly different inspiratory volumes are accentuated. Finally, in Figure 3.3c, relative signal intensity difference maps are shown after image registration. Overall, image registration does not affect lung signal intensity, and resolves structural mismatches, such as vessels, diaphragm position and lungs boundaries and corrects for through plane motion.

For three different ROIs (4 × 4 × 4 pixels), the mean SI, as observed in the five datasets after image co-registration, is shown in Figure 3.3d. Local respiratory index values α_{local} of 0.88±0.07, 0.93±0.07 and 1.13±0.05 are found with an R^2 exceeding 0.976, indicating appropriate description of the experimental data by the adapted sponge model after image registration using an ROI analysis.

Illustrative respiratory α-maps for two volunteers (a male and a female) are shown in Figure 3.4 for representative slices in coronal, sagittal, and axial orientations. Generally, a homogenous respiratory index is observed on iso-gravitational planes, whereas the respiratory index values almost double in the caudal part (α ≈ 1.4) in comparison to ventral part (α ≈ 0.7).

A side-by-side comparison of respiratory α-maps for a volunteer examined three consecutive times for reproducibility tests is presented in Figure 3.5, revealing a striking visual similarity in the respiratory α-maps. This is corroborated by the low standard deviation (Fig. 3.5d) and by high gamma-index passing rates of 84% and 87%. As a result, highly similar global respiratory indices α_{global} are observed for the three examinations: 0.97±0.03, 0.98±0.04 and 0.95±0.03 (coefficient of variation cv = 1.6 %). The reproducibility results for the two other subjects revealed analogous results: similar global respiratory indices for the three examinations (cv = 1 %, c.f. Table 3.2) and gamma-index passing rate in between 87% and 94%.

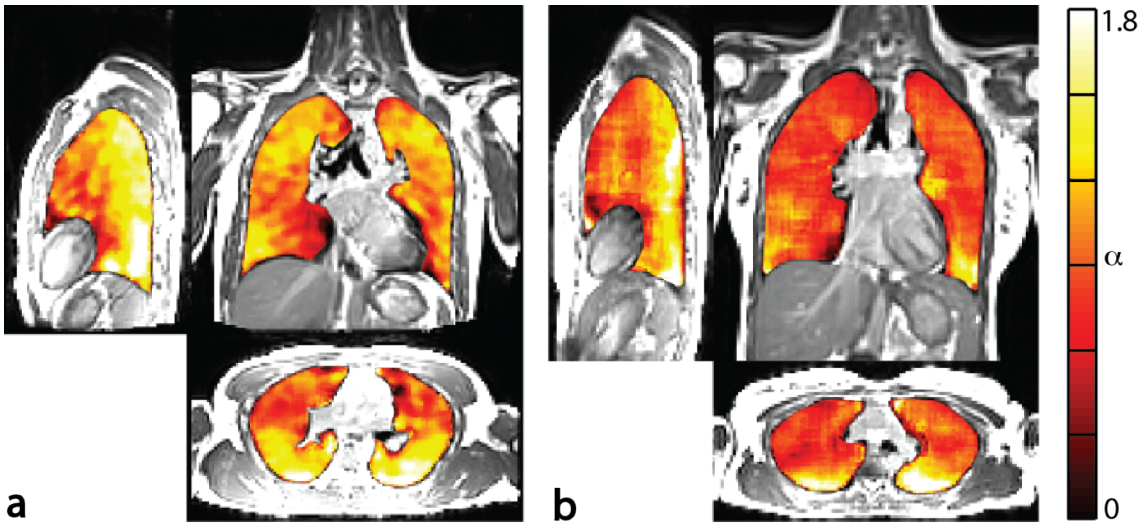

Figure 3.4. Three-dimensional respiratory α-maps overlaid on 3D ufSSFP morphological images in sagittal, coronal, and transverse orientation for two healthy volunteers [(a): male and (b): female]. A global respiratory index of α_{global} = 1.10±0.04 (male) and of α_{global} = 0.91±0.04 (female) was found (cf. Table 3.2, Volunteers 2 and 8).

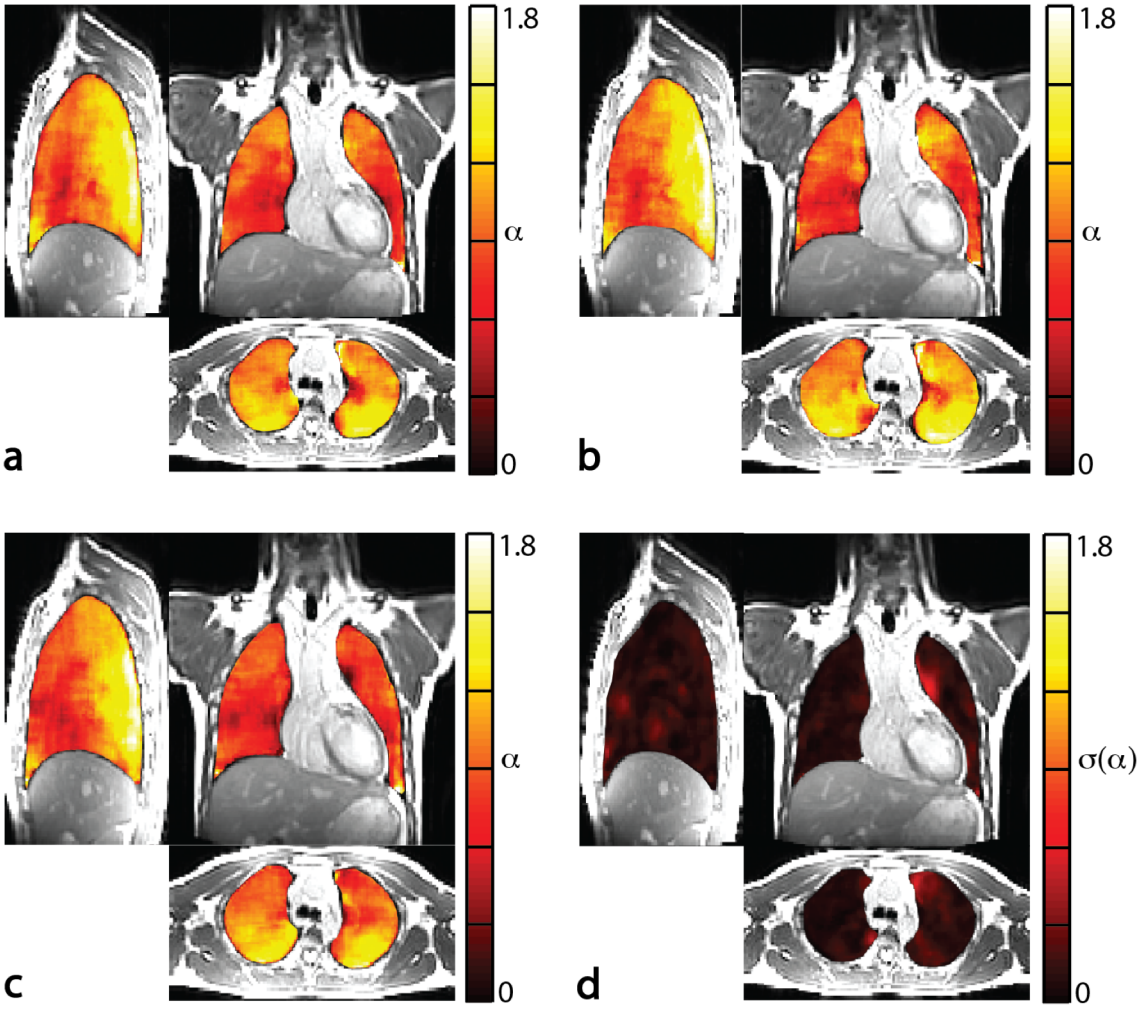

Figure 3.5. (a-c) Reproducibility of respiratory α-mapping evaluated in a healthy subject (Table 3.2, Volunteer #6) scanned three consecutive times and (d) the resulting standard deviation map.

3.4.3 Respiratory α-mapping in patients

Finally, the feasibility of respiratory α-mapping was evaluated in the clinical setting. Respiratory α-maps obtained in two COPD patients are shown in Figure 3.6 and compared to CT and DCE-MRI. Respiratory α-mapping is compared to DCE which is a robust and well established clinical imaging technique [2, 31, 147–149] for the assessment of obstructions; DCE perfusion-impairments reflect the effects of hypoxic pulmonary vasoconstriction and this is regarded as a surrogate for lung ventilation [75, 136]. Similarly, for COPD, it has been shown the emphysematous destruction, as quantified with CT densitometry, leads to a significant increase of closed volume, thus a decreased ventilation of those regions and subsequent hypoxic vasoconstriction [148, 150]. CT emphysema maps reveal different impairments for the two COPD patients: the

first has localized large emphysematous regions (Fig. 3.6 in the upper row, 53 year old male) while the second patient has a more diffuse form of emphysema (in the bottom row, 75 year old female). Similar abnormalities are seen on DCE perfusion images. Overall, structural emphysematous tissue destruction and perfusion defects visually correlate with the location of conspicuous functional impairment indicated on the respiratory maps (e.g., $\alpha_{local} < 0.3$). Global respiratory indexes $\alpha_{global} = 1.07\pm0.03$ and $\alpha_{global} = 0.66\pm0.05$ are found (comparable with literature results from CT measurements [139]).

Respiratory α-maps for a CF patient are compared to FD ventilation- and perfusion-weighted maps in Figure 3.7. The three functional imaging modalities visually correspond, showing the same major functional defect in the middle lobe, less severe impairments and similar healthy pulmonary regions. The global respiratory index for the CF patient is $\alpha_{global} = 0.91\pm0.04$.

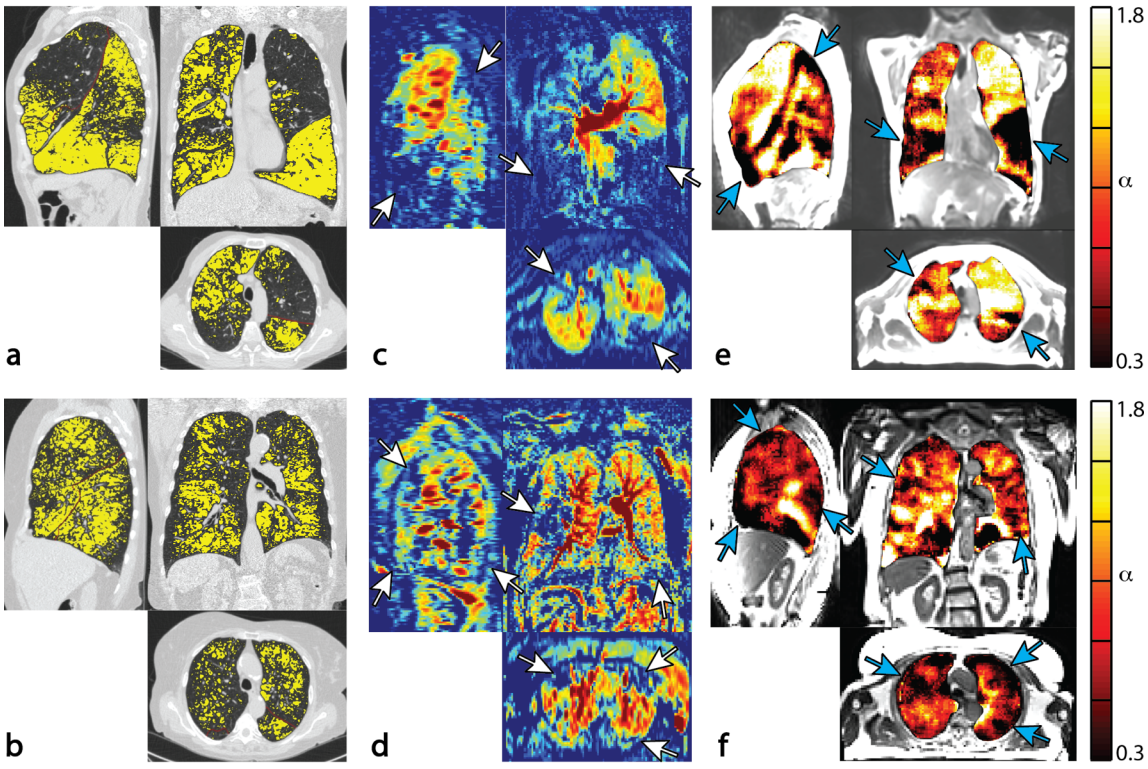

Figure 3.6. Intraindividual scans in COPD patients performed the same day: CT emphysema maps (a, b), DCE-MRI subtraction maps (c, d) and respiratory α-maps (e, f). The arrows indicate exemplary functional defects on respiratory α-maps (e.g., $\alpha_{local} < 0.3$) that correlate with both emphysematous regions on CT images (colored in yellow) and perfusion defects in DCE-MRI (blue regions).

Table 3.2 summarizes the respiratory index values for the volunteers and the patients examined with the respiratory α-mapping protocol (lung volumes from FRC to tidal inspiration). For healthy male volunteers, respiratory index α_{global} varied between 0.95 and 1.14 (1.07±0.06, mean ± SD), while for female volunteers it varied from 0.91 to 1.05 (0.95±0.06, mean ± SD); the volunteers average was α_{global} = 1.02±0.07. For the five volunteers scanned with both the adapted sponge model protocol (lung volumes ranging from RV to TLC) and the respiratory α-mapping protocol (lung volumes from FRC to tidal inspiration), the respiratory values α_{global} between the two experiments differ less than 2% and show a strong correlation (Lin's Concordance correlation coefficient ρ_c = 0.93). For all examined subjects, coefficients of determinations R^2 higher than 0.972 are found, indicating an appropriate description of the experimental data using the adapted sponge model.

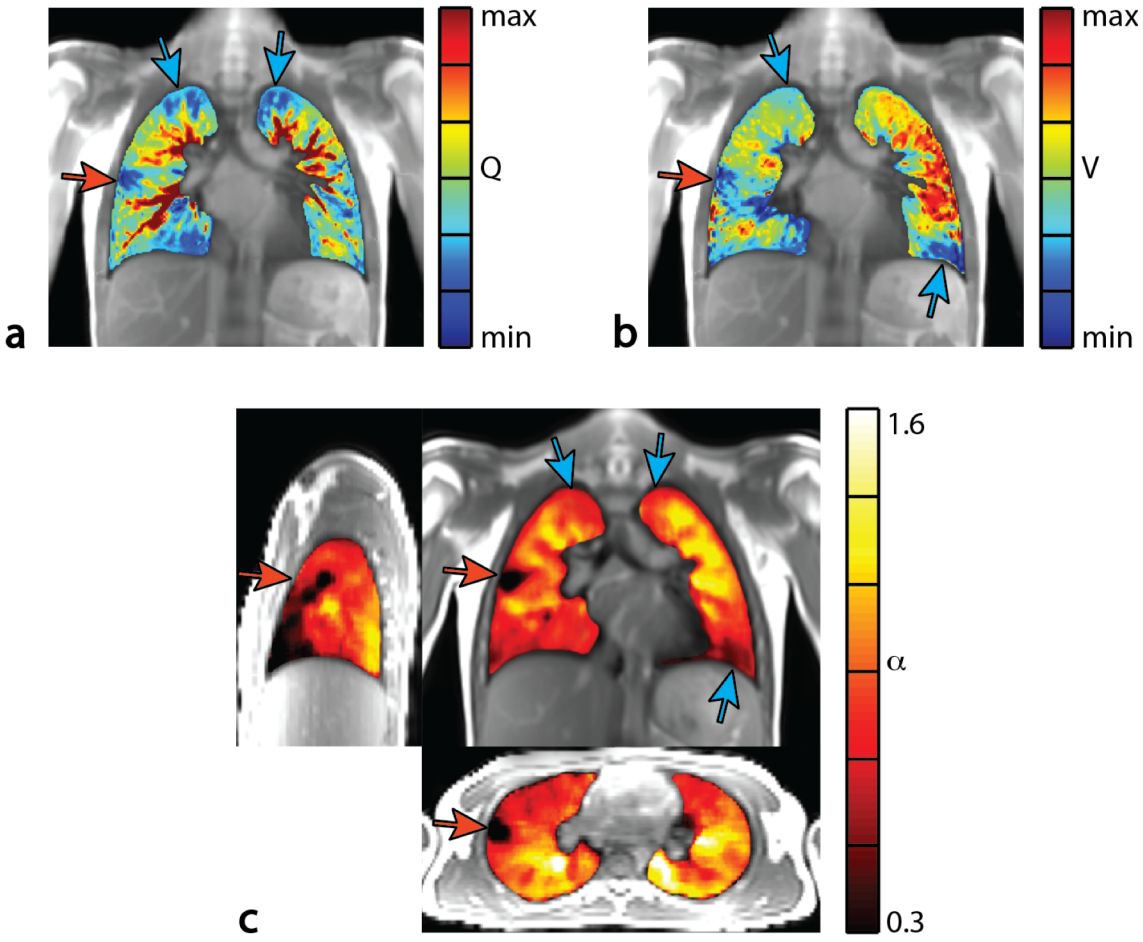

Figure 3.7. Fourier decomposition (a) perfusion-weighted and (b) ventilation-weighted maps compared to (c) α-maps for a pediatric CF patient. A major functional defect of the middle lobe (red arrows) and other less severe impairments (blue arrows) are clearly visible on all the three imaging modalities.

Table 3.2. Demographic information (gender, age, height, weight), global respiratory index (mean ± uncertainty), Pearson correlation coefficient (R^2) and lung volume for the subjects examined with the respiratory α-mapping protocol (lung volumes from FRC to tidal inspiration).

Subject	Gender, Age, Height (cm), Weight (kg)	α_{global}	R^2	Lung volume [L]		
				mean±SD	min	max
Volunteer 1(*)	M, 32, 179, 82	1.14 ± 0.04	0.973	2.85±0.28	2.72	3.23
Volunteer 2(*)	M, 26, 190, 80	1.10 ± 0.04	0.994	2.69±0.24	2.41	2.99
Volunteer 3(*)	M, 34, 175, 80	1.12 ± 0.02	0.996	1.99±0.27	1.69	2.29
Volunteer 4(*)	M, 32, 178, 75	1.05 ± 0.02	0.997	2.79±0.28	2.38	3.08
Volunteer 5(*), scan 1	M, 28, 185, 84	1.04 ± 0.03	0.996	2.92±0.41	2.71	3.78
" , scan 2	"	1.02 ± 0.03	0.995	3.20±0.44	2.40	3.65
" , scan 3	"	1.03 ± 0.02	0.999	3.13±0.39	2.64	3.69
Volunteer 6, scan 1	M, 29, 175, 75	0.97 ± 0.03	0.996	2.59±0.40	2.21	3.34
" , scan 2	"	0.98 ± 0.04	0.997	2.43±0.35	2.08	3.03
" , scan 3	"	0.95 ± 0.03	0.998	2.48±0.42	2.16	3.25
Volunteer 7, scan 1	F, 49, 164, 58	1.04 ± 0.02	0.984	2.72±0.27	2.40	3.10
" , scan 2	"	1.05 ± 0.03	0.986	2.62±0.23	2.37	2.95
" , scan 3	"	1.03 ± 0.02	0.989	2.63±0.21	2.34	2.89
Volunteer 8	F, 30, 168, 53	0.91 ± 0.04	0.995	1.84±0.27	1.53	2.28
Volunteer 9	F, 30, 170, 54	0.92 ± 0.03	0.994	2.49±0.19	2.28	2.75
Volunteer 10	F, 34, 170, 60	0.94 ± 0.02	0.996	2.31±0.39	1.89	2.83
Patient 1, COPD	M, 53, 186, 78	1.07 ± 0.03	0.989	7.13±0.44	6.66	7.84
Patient 2, COPD	F, 75, 158, 67	0.66 ± 0.05	0.972	3.93±0.37	3.39	4.40
Patient 3, CF	F, 12, 157, 42	0.91 ± 0.04	0.991	1.48±0.34	1.29	1.98

(*) volunteers 1 to 5 were scanned with both protocols (cf. Table 3.1) and the two measurements correlate (Lin's Concordance correlation coefficient $\rho_c = 0.93$).

3.5 Discussion

In this work, we introduced a novel proton-based MR method for volumetric whole lung functional imaging on 1.5T, applicable in the clinical setting not requiring contrast application of any sort or experimental hardware. The adapted sponge model is used to derive respiratory α-maps from a set of ufSSFP scans acquired around the tidal volume region. Similarly to well-established ventilation techniques such as SPECT [67], ^{3}He [68] and PET [69], respiratory α-maps in healthy subjects exhibited the expected iso-gravitational homogeneity, and showed a marked/distinctive gravitation-related respiratory gradient. In accordance with literature [70], respiration from the non-dependent (ventral) to the dependent (dorsal) lung regions was almost doubled. In patients

with obstructive lung diseases, the functional impairments associated with emphysematous regions on CT images, perfusion defects on DCE-MRI and ventilation / perfusion abnormalities on FD-maps coincided well with the defects identified on the respiratory α-maps.

For healthy volunteers, the respiratory index α_{global} (which is a measure for the change in lung perfusion during the breathing cycle, cf. "Theory" Section 3.2.2) was on average 1.02±0.07, in accordance with literature results (data elaborated from [71], α_{global} = 1.04). Interestingly, α_{global} appears to be different for male and female (1.07 and 0.95, respectively), but a larger collective of volunteers would be required for conclusive results.

Multi-volumetric proton-based lung MRI using spoiled gradient echo was already introduced by Pennati et al. [112] as a biomarker for regional ventilation. In their work, lung acquisitions at two different inspiratory volumes were used to calculate by subtraction proton density difference maps. It was demonstrated that the maps positively correlate with hyperpolarized ^{3}He imaging in healthy volunteers and in patients affected by asthma and emphysema. The derivation of ventilation-weighted information by simple subtraction or by taking the relative difference between a variety of breathing phases (e.g., using Fourier decomposition, cf. [123, 140]), however, depends on the lung proton density and thus on the breathing phase (cf. Fig. 3.3 and [151]). In contrast, based on 3D ufSSFP multi-volumetric acquisitions, the respiratory index α_{local} assesses regional ventilation from a physical lung model taking into account the lung volume which modulates the regional signal intensities in the lung. From the model, the resulting respiratory index α becomes rather insensitive to the lung density and thus to the breathing phase [cf. Eq. (3.11)]. This provides respiratory α-mapping with high reproducibility, as demonstrated by a low standard deviation and high gamma-index passing rate.

Respiratory α-maps were shown to yield comparable ventilation-related information as Fourier decomposition (cf. Fig. 3.7). Contemporary FD imaging typically requires the acquisition of 8 – 12 coronal image time series (each series contains about 160 images acquired within 40 – 50 s) acquired in free-breathing to cover the whole lung [104]. This yields a total scan time of 6 – 10 min for a typical slice thickness of 12 – 15 mm. Generally, chest wall expansion during breathing can cause through-plane motion (anterior-posterior) leading to image artifacts and image registration issues [102]. In contrast, respiratory α-mapping requires breath-holding maneuvers and is only able to capture ventilation-related information but provides an isotropic assessment of the whole lung from just five multi-volumetric acquisitions that can be acquired in about 3 min scan time. Furthermore, the respiratory index is virtually independent from the inspiratory phase and breathing amplitude, thus providing high reproducibility.

Similarly to other proton-based ventilation techniques [112, 123, 140], respiration-related signal modulations were assumed to reflect density changes in the lung (cf. “Theory” Section 3.2.2). Lung relaxation times, however, might be affected by breathing, which in turn may lead to a bias in the observed signal modulations. To investigate the influence of the lung relaxation times, a T_1 change of less than 10% [152] in combination with a presumably substantially overvalued 100% variation in T_2 is considered. The induced T_1/T_2 variations based on these assumptions affect the bSSFP signal by less than one order in magnitude as compared to the observed signal variation between full inspiration and forced expiration. Considering a T_1 change of less than 10% [152], in combination with a presumably considerably overvalued 100% variation in T_2, however, leads to T_1/T_2 variations that affect the bSSFP signal by less than one order in magnitude as compared to the observed signal variation between full inspiration and forced expiration. This justifies the assumption that the signal variations between diverse respiratory phases reflect predominantly proton density changes.

Generally, respiratory α-maps were derived from MR scans taken around tidal respiratory volumes to mimic tidal respiration and to avoid possible registration issues related to the requirement of large deformations fields, e.g., if scans were performed from forced expiration to total lung capacity. Thus, excellent registration accuracy could be achieved, as confirmed by whole lung SI preservation measurements (not presented) and by qualitative visual assessment of selected landmarks. Moreover, for scanning, the tidal volume region rather than the inspiratory phase was selected to achieve close to maximum parenchymal signal levels. However, we recognize that our method still depends on the accuracy of the deformable image registration, which is a common issue for several lung ventilation imaging techniques. Another limitation is the requirement for manual lung segmentation. An automatic lung segmentation algorithm would be required to reduce the manual burden for large-scale studies or to enroll the method into the daily clinical routine. Recently proposed algorithms, such as the ones presented by Kohlmann et al. [153] and by Tustison et al. [154], might be suitable, but their applicability needs to be investigated. Another potential limitation refers to the ability of patients to perform breath-holding maneuvers. Nevertheless, from the initial experience the heavily compromised patients could perform breath-holds of 11 seconds. However, especially for infant, a free-breathing, self-navigating, 3D bSSFP method is necessary and can be adopted [155, 156].

As shown for the patients, on respiratory α-maps under-ventilated and incompressible lung regions (e.g., bullae, obstructions, air-trapping, emphysematous destructions and hypoxic vasoconstrictions) expand less than healthy tissues. Overall, respiratory α-mapping may also be a sensitive measure for assessing the functionality of lungs in other categories of pulmonary obstructive diseases, such as asthma, primary ciliary dyskinesia and bronchiolitis obliterans. Moreover, it might be used to evaluate disease progression and to assess lung functionality in

impaired regions before and after therapeutic interventions (e.g., drug administration, surgery, broncoscopically implanted valves, and bronchial thermoplasty).

3.6 Conclusions

We have introduced a fast and reproducible contrast agent-free volumetric method for functional lung imaging using proton-based MRI at 1.5T that is applicable in the clinical setting even in patients with shortness of breath and children. Based on an adapted sponge model for lung tissue, the deduced respiratory index α may serve as a reproducible and normative measure to evaluate disease progression and for repeated monitoring of therapeutic responses of functionally impaired lung regions.

ADDENDUM TO CHAPTER 3

Respiratory α-mapping of cystic fibrosis at 1.5T

A modified version of this chapter has been published as:

Pusterla O, Bauman G, Nyilas S, Madörin P, Jung B, Ith M, Stranzinger E, Frey U, Latzin P, Bieri O. *Respiratory α-Mapping of Cystic Fibrosis at 1.5T.* Proceedings of the 25th annual meeting of the ISMRM, Honolulu, HI, USA. 2017:0118.

A3.1 Purpose

To evaluate 3D respiratory α-mapping, a new method for native whole-lung pulmonary functional imaging at 1.5T derived from ^{1}H multi-volumetric ultra-fast balanced steady-state free precession (ufSSFP) breath-hold scans [45, 157], in pediatric patients with cystic fibrosis (CF) in comparison to functional parameters derived from nitrogen multiple-breath washout (N_2-MBW).

A3.2 Materials and methods

A3.2.1 Theory

At every breath the lung tissue undergoes compression/expansion and its physical mass density varies ($\rho = \frac{M}{V}$).

The observed ufSSFP signal intensity variation at diverse inspiratory volumes (Fig. A3.1) is in excellent agreement with the adapted sponge model (see Section 3.4), predicting, similar to physical mass density ($\rho = \frac{M}{V}$), the signal intensity (SI) to scale inversely proportional to the lung volume V:

$$\mathrm{SI}(V,\vec{x}) = \Lambda(\vec{x}) \cdot V^{-\alpha(\vec{x})} + \eta(\vec{x}) \quad \Longrightarrow \quad \alpha(\vec{x}) = -\frac{\partial\left(\log\left(\mathrm{SI}(V,\vec{x})\right)\right)}{\partial(\log(V))} \tag{A3.1}$$

where $\vec{x}$ is the position of a voxel, $\Lambda(\vec{x})$ is a SI scaling factor, $\eta(\vec{x})$ the SI in the limit of infinite volume, i.e., noise, and $\alpha(\vec{x})$ maps lung expansion during breathing, referred to as respiratory α-index. The index α reflects a ventilation-weighted pulmonary measure (the acronym "α" was chosen after Aeolus, mythical divinity, ruler of the winds!) and is virtually independent from regional lung density, as well as from the inspiratory phase and breathing amplitude (cf. Fig. A3.1b and Section 3.2.2). From the model, a value $\alpha(\vec{x}) = 1$ indicates that a region-of-interest (ROI) expands equally to the whole lung mean expansion, whereas $\alpha(\vec{x}) < 1$ indicates that the ROI expands less [for $\alpha(\vec{x}) > 1$, more] than the whole lung mean expansion. Generally, functionally impaired under-ventilated lung regions have low respiratory α-values (e.g., α < 0.3-0.5).

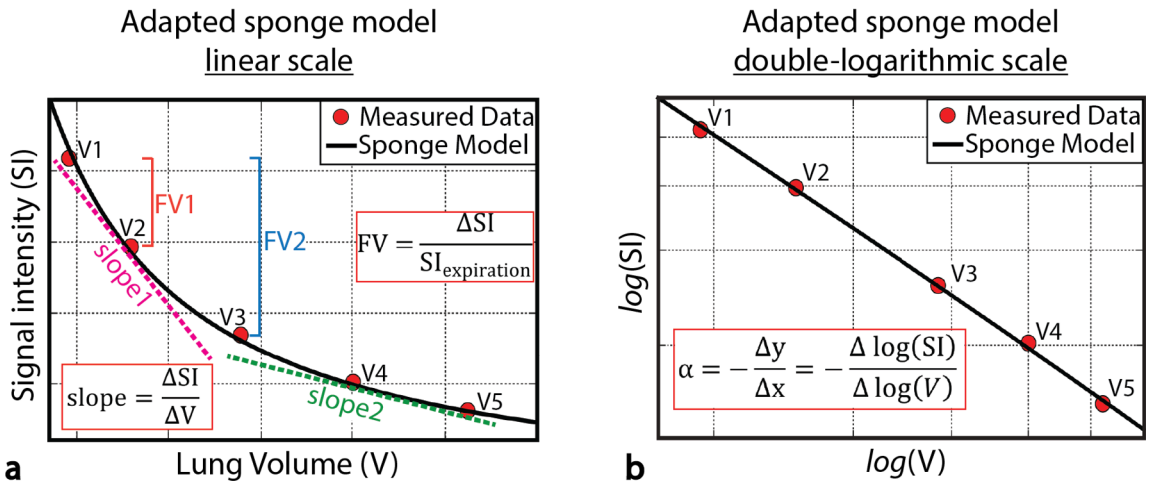

Figure A3.1. For ufSSFP imaging the measured pulmonary SI (red dots) as a function of the lung volume (e.g., measured in an ROI as indicated in Fig. A3.2d) follows the adapted sponge model (solid lines). (a) The sponge model visualized on a linear scale shows that classical SI-regressions analysis (*slope* = $\frac{\Delta SI}{\Delta V}$, e.g., pink and green dashed-lines, or Fractional Ventilation *FV* = $\frac{\Delta SI}{SI_{expiration}}$) will depend on the lung volume and inspiratory-level (and *slope* = $\frac{\Delta SI}{\Delta V}$ from local proton-density as well!). (b) The sponge model visualized on double-logarithmic scale highlight that the respiratory index $\alpha = -\frac{\Delta \log(SI)}{\Delta \log(V)}$, in contrast, is virtually independent on the lung volume.

A3.2.2 Subjects and measurement protocol

Respiratory α-mapping was evaluated in 24 pediatric patients with CF (13±3 years, range 6-17 years) and compared to the lung clearance index (LCI) from N_2-MBW measurements, acquired at the same day. This prospective study was approved by the local Ethics Committee and all participants/legal guardian provided informed consent.

Multi-volumetric ufSSFP scans of the lung were performed in breath-hold (< 12 seconds) and in supine position at 1.5T (Aera, Siemens Healthineers). Scanning was repeated at five breath-holding positions comprised in the tidal respiratory region with an isotropic resolution of 3.1 mm, a TE/TR = 0.47/1.19 ms, and a flip angle of 19° (for technical details and other parameters cf. Section 3.3). Clinical acquisition-time for α-mapping was less than 3 minutes.

A3.2.3 Image post-processing and analysis

Figure A3.2 summarizes the principal steps to calculate respiratory α-maps, i.e., semi-automatic segmentation of the lung volume, 3D deformable image registration (Elastix), median filtering to remove the vasculature [142], and voxel-wise calculation of the respiratory indexes $\alpha(\vec{x})$ [cf. Eq. (A3.1)] . Due to the ventral-to-dorsal respiratory-gradient characteristic e.g., in the α-maps of healthy volunteers (cf. Fig. A3.2e), respiratory impairments were analyzed iso-gravitationally and automatically associated with an α-value less than 0.75 of the observed median α-value distribution in each coronal plane. From this, a respiratory percent defect ratio was calculated from the number of impaired voxels divided by the total number of voxels enclosing the whole lung.

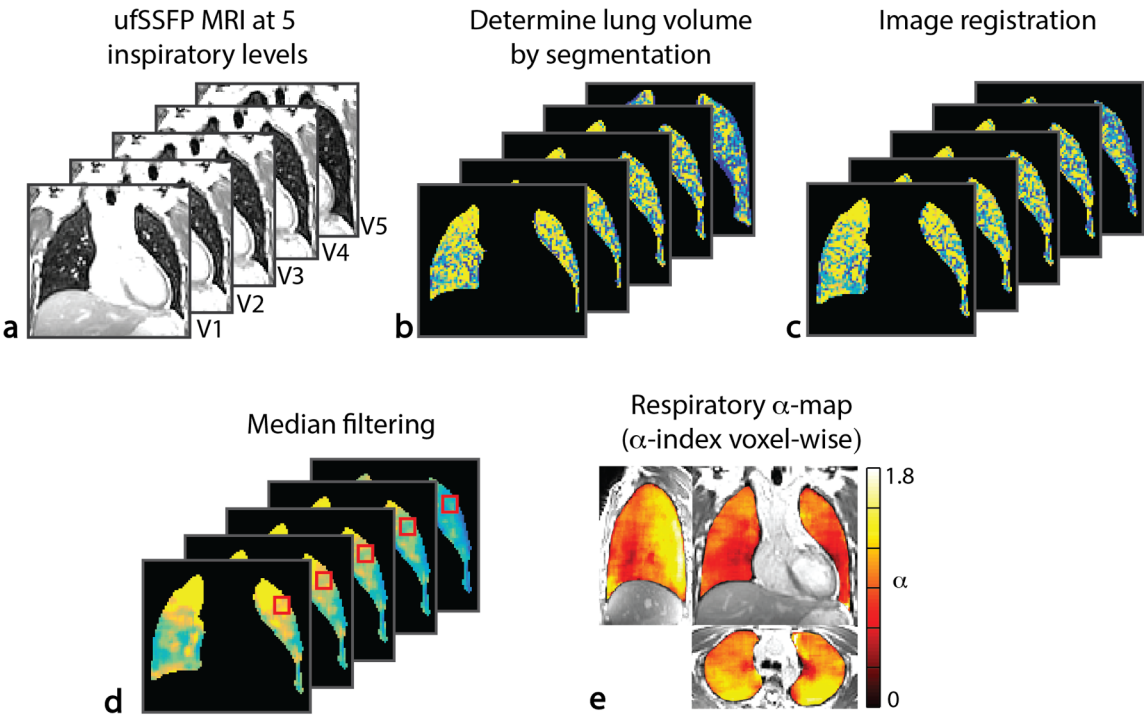

Figure A3.2. Illustrative summary of the framework used for respiratory α-mapping. (a) Imaging is performed at 5 different inspiratory levels. (b) As a result of the compression/expansion, the pulmonary signal intensity variates and is modulated depending on the lung volume (cf. Fig. A3.1). The 5 lung volumes are assessed by semi-automated segmentation. (c) Image registration resolves structural misalignments caused by the different inspiratory levels, while preserving the signal. (d) Median filtering removes vasculature and resolves parenchyma signal. (e) The α-index is calculated voxel-wise. The α-maps represents normal appearing lung tissue of an healthy subject.

A3.3 Results

From the 24 patients enrolled in the study, breath-holding was feasible for 22, and images were artifact-free in 20 patients. Illustrative morphological ufSSFP images and α-maps in a CF patient (15 y, male) are shown in Figure A3.3. In contrast to the characteristic iso-gravitational homogeneity and the physiological ventral-to-dorsal respiratory-gradient present in the α-maps of a healthy volunteer (Fig. A3.2e), respiratory α-maps of the CF patient (Fig. A3.3b) revealed under-ventilated regions. The α-impairments are mainly associated with heavily atelectatic areas of the lung in this case (Fig. A3.3a). Overall, in the cohort of patients, the percentage of respiratory α-impairments determined by α-mapping revealed a highly significant (p-value < 10^{-6}) and strong correlation (Spearman ρ = 0.88) with the LCI, as shown in Figure A3.4.

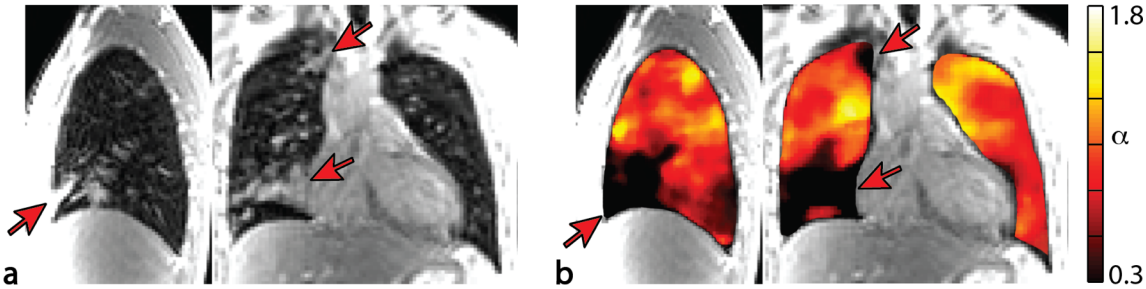

Figure A3.3. Morphological ufSSFP imaging (a) and respiratory α-maps (b) in a CF patient (male, 15 years old). Lung impairments with reduced ventilation [black regions in (b), α<0.3] correspond well to regions of atelectasis and mucus observed on morphological images [red arrows in (a)].

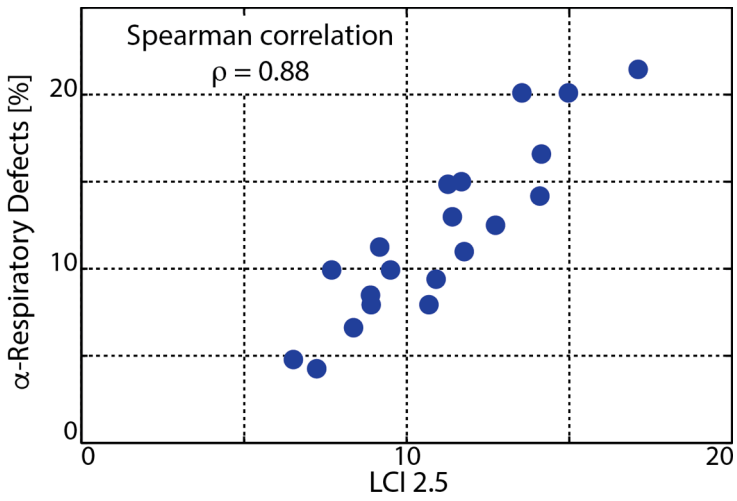

Figure A3.4. Plot of the assessed respiratory defects from α-mapping and the lung clearance index (LCI) from multiple-breath washout measurements. The functional parameters show a highly significant (p-value < 10^{-6}) and strong correlation (Spearman ρ = 0.88).

A3.4 Discussion

In this work, we evaluated the recently introduced respiratory α-mapping method in a small cohort of pediatric patients with CF. Respiratory α-mapping allows for regional respiratory assessment of the whole lung, and the percentage of automatically detected respiratory defects showed a pronounced correlation with LCI from N_2-MBW measurements.

The index α is derived from a multi-volumetric physical compression model of lung tissue, and since it is virtually independent from the respiratory phase (cf. Fig A3.1b), the breathing amplitude and from regional lung density (cf. Sections 3.2 and 3.3), respiratory α-mapping may serve as a reproducible and normative measure to quantify and evaluate patho-physiological impairments, and can be potentially used to compare measurements between different subjects and/or changes in the disease progression, such as in CF patients. In conclusion, respiratory α-mapping shows good prospects as a quantitative outcome measure for monitoring respiratory impairments or to assess the effect of therapeutic or clinical interventions.

CHAPTER 4

Three-dimensional oxygen-enhanced MRI of the human lung at 1.5T with ultra-fast balanced steady-state free precession

A modified version of this chapter has been published as:

Pusterla O, Bauman G, Bieri O. *Three-dimensional oxygen-enhanced MRI of the human lung at 1.5T with ultra-fast balanced steady-state free precession.* Magn Reson Med, 2018, 79:246–255.

CHAPTER ABSTRACT

Purpose: To assess the feasibility of three-dimensional (3D) oxygen-enhanced (OE) MRI of the lung at 1.5T using multi-volumetric ultra-fast balanced steady-state free precession (ufSSFP) acquisitions.

Methods: Isotropic imaging of the lung for OE-MRI was performed with an adapted three-dimensional ufSSFP sequence using five breath-hold acquisitions ranging from functional residual capacity to tidal inspiration under both normoxic (room-air) and hyperoxic (100% O_2) gas conditions. A sponge model, which captures the parenchymal signal intensity variation as a function of the lung volume, for each O_2 concentration was fitted to the acquired multi-volumetric datasets after semi-automatic lung segmentation and deformable image registration. From the retrieved model parameters, 3D oxygen-enhancement maps were calculated.

Results: For OE ufSSFP imaging, the maximum parenchymal signal is observed for flip angles around 23° under both normoxic and hyperoxic conditions. It is found that the sponge model accurately describes parenchymal signal at different breathing positions, thereby mitigating the confounding bias in the estimated oxygen-enhancement from residual density modulations. From the model, in the healthy volunteers an average lung oxygen-enhancement of 7.0%±0.3% was found, and the oxygen-enhancement maps indicate a ventral to dorsal gravitation-related gradient.

Conclusion: The study demonstrates the feasibility of whole-lung OE-MRI from multi-volumetric ufSSFP in healthy volunteers.

4.1 Introduction

With the development of dedicated pulse sequences and optimized acquisition schemes, magnetic resonance imaging (MRI) has become an attractive radiation-free modality for morphological and functional imaging of the lung [4, 29]. For the assessment of pulmonary perfusion, dynamic contrast-enhanced (DCE) MRI is a well-established technique that provides high spatial and temporal resolution, but requires the intravenous injection of contrast agents. For ventilation imaging, non-proton-based MRI with inhaled hyperpolarized ^{3}He or ^{129}Xe gases yields a direct measure of pulmonary ventilation and has demonstrated compelling results [38, 119]. However, its broad application is hindered by the requirement of dedicated equipment.

An interesting alternative to hyperpolarized gas imaging may be found in oxygen-enhanced (OE) proton-based MRI [95] since it does not require additional equipment and is based on the paramagnetic properties of oxygen itself. When breathed, oxygen acts as a weak contrast agent in the lung, shortening the longitudinal relaxation time (T_1) and the apparent transverse relaxation time (T_2*) [158]. The observed decrease in T_1 under hyperoxic condition is attributed to an increased concentration of dissolved O_2 in the parenchyma, blood vessels and lung tissue [99]. OE-MRI is usually considered an indirect measure for ventilation, diffusion and perfusion on T_1-weighted images [96]. If only one of the three functions is regionally hampered, a lower signal intensity (SI) enhancement is detected locally. In contrast, the T_2* shortening effect in the lungs while breathing oxygen can be attributed to the mesoscopic magnetic susceptibility changes at the tissue/gas interfaces in the alveoli and reflects a measurement for pulmonary ventilation [99].

Oxygen-related signal enhancement in the lung is commonly derived voxel-wise based on the relative difference of images acquired in hyperoxic (100% O_2) and normoxic (room-air, 21% O_2) conditions and has shown promising results for patients with diseases such as cystic fibrosis, pulmonary embolism, and emphysema [115, 159]. Moreover, the technique was recently applied to monitoring the severity of asthma, evaluating pharmacological treatment in COPD, and defining candidates for lung volume reduction surgery [98, 160, 161]. Generally, however, the overall magnitude of the signal enhancement from oxygen is weak, i.e., 5%-10% [99, 158]. As a result, the oxygen-enhancement is typically inferior to the natural SI variations of the lung parenchyma induced by different but similar inspiratory volumes (e.g., in expiration) and OE-MRI can be easily flawed [162]. Consequently, a strategy to take into account the SI modulations of the lung at diverse inspiratory phases appears mandatory. Moreover, most of the OE-MRI methods are confined to 2D acquisitions and are thus limited either in speed and/or chest coverage.

Here, we investigate the feasibility of 3D oxygen-enhanced MRI using ultra-fast balanced steady-state free precession (ufSSFP) imaging, recently introduced for improved morphological and functional lung imaging [45, 157]. Based on multi-volumetric ufSSFP lung scans (acquired at different inspiratory phases), we propose a new framework for robust volumetric OE-MRI that takes into account signal intensity variations of the lung parenchyma using an adapted sponge model (see Chapter 3 and Ref. [157]).

4.2 Methods

Four healthy subjects (29 ± 3 years old, three males and one female) underwent ufSSFP lung imaging on a 1.5T whole-body MR-scanner (MAGNETOM Avanto, Siemens Healthineers, Erlangen, Germany) using a 12-channel thorax and a 24-channel spine receive-array. Written informed consent was obtained from each subject prior to the examinations. All measurements were performed in breath-hold and in supine position. Normoxic scans were acquired first. Subsequently, after a 5 min 100% O_2 wash-in phase, hyperoxic imaging was performed. The gases were delivered through a non-rebreathing face-mask with a 1.5 L reservoir bag at a flow rate of 20-25 L/min.

4.2.1 Oxygen-related signal enhancement for balanced SSFP

The oxygen-enhancement between scans acquired under normoxic (room air, 21% O_2) and hyperoxic (100% O_2) conditions is defined as a relative measure:

$$\mathrm{OE} := \frac{\mathrm{SI_{O2}} - \mathrm{SI_{Air}}}{\mathrm{SI_{Air}}} \tag{4.1}$$

where the subscripts "*Air*" and "O_2" indicate the two different gas phases, respectively.

For ufSSFP imaging, the theoretically expected O_2-enhancement can be estimated using the common bSSFP signal model [163] assuming a T_2/T_1 ranging between 100 ms/1000 ms to about 40 ms/1400 ms in normoxic condition [29, 99, 101, 164], and a 10% decrease in T_1 (but constant T_2 [101, 164]) for hyperoxic conditions [99, 101, 165]. At on-resonance, bSSFP becomes T_2/T_1-weighted, and thus, similarly to the oxygen-enhancement with T_1 weighted pulse-sequences [96], OE-MRI with bSSFP is an indirect measure for ventilation, diffusion, and perfusion altogether.

4.2.2 Respiratory-related signal modulation in bSSFP - The sponge model

The lung parenchyma can be compared to sponge-like tissue, which periodically expands and contracts following the movement of the diaphragm and chest walls, resulting in bidirectional air flow and ventilation. It has been previously hypothesized that for two volumetric CT images the signal intensity modulations resulting from contraction / expansion of the lung can be described by a sponge model [166]. This model has recently been reformulated for ultra-fast bSSFP imaging (see Chapter 3 and Ref. [157]), based on the observation that the pulmonary bSSFP signal scales inversely proportional with the total lung volume V (similarly to mass density $\rho = \frac{M}{V}$), yielding the adapted sponge model:

$$\mathrm{SI}_{\mathrm{Sponge}}(V) = \Lambda \cdot V^{-\alpha} + \eta \tag{4.2}$$

where Λ (>0) is a scaling factor (reflecting parenchymal spin density). In Equation (4.2), η refers to the SI in the limit of infinite volume, i.e., noise, and α (≈1) maps the lung expansion and changes in pulmonary blood volume during breathing. Overall, Λ, η, and α are assumed to be constant over the breathing cycle.

For shallow breathing (small volume variations), e.g., in the tidal respiratory volume region, we approximate the adapted sponge model as a Taylor series expansion around an arbitrary reference volume V_{ref} (in the tidal volume region), which yields after short calculations and rearrangement of terms, the linear relation [167]:

$$\begin{aligned}\mathrm{SI}_{\mathrm{Sponge}}(V) = \Lambda \cdot V^{-\alpha} + \eta \approx [(1+\alpha)\cdot\Lambda\cdot {V_{\mathrm{ref}}}^{-\alpha} + \eta] - \left[\alpha\cdot\Lambda\cdot {V_{\mathrm{ref}}}^{-\alpha-1}\right]\cdot V \equiv \\ \equiv \mathrm{C}_0 - \mathrm{C}_1 \cdot V\end{aligned} \tag{4.3}$$

4.2.3 Calculation of oxygen-enhancement maps from the sponge model

After estimation of the sponge model parameters [C_0 and C_1; cf. Eq. (4.3)] for both normoxic and hyperoxic conditions (e.g., by orthogonal regression of the volume-signal intensity relationship of the lung parenchyma), the SI can be derived for any arbitrary lung volume V (around V_{ref}). From this, the global O_2-enhancement of the lung is given by inserting Eq. (4.3) into Eq. (4.1):

$$\mathrm{OE}_{\mathrm{global}}(V) = \frac{(\mathrm{C}_{1,\mathrm{Air}} - \mathrm{C}_{1,\mathrm{O2}})\cdot V + (\mathrm{C}_{0,\mathrm{O2}} - \mathrm{C}_{0,\mathrm{Air}})}{\mathrm{C}_{0,\mathrm{Air}} - \mathrm{C}_{1,\mathrm{Air}}\cdot V} \tag{4.4}$$

Similarly, after spatially matching the lung structures of the multi-volumetric acquisitions by a

deformable registration algorithm, sponge model parameters [C_0 and C_1; cf. Eq. (4.3)] can be estimated voxel-wise (i.e., locally at the position $\vec{x}$, cf. Chapter 3) to yield a voxel-wise, i.e., local estimation of the O_2-enhancement,

$$OE_{local}(\vec{x},V) = \frac{\left(C_{1,Air}(\vec{x}) - C_{1,O2}(\vec{x})\right)\cdot V + \left(C_{0,O2}(\vec{x}) - C_{0,Air}(\vec{x})\right)}{C_{0,Air}(\vec{x}) - C_{1,Air}(\vec{x})\cdot V} \quad (4.5)$$

4.2.4 Imaging

Imaging was performed with an ultra-fast SSFP framework, as described elsewhere [45], yielding a TE/TR of 0.47 ms/1.19 ms, using a non-selective RF pulse with a duration of 80 µs, a readout bandwidth of 1563 Hz/pixel, and a field-of-view of 400 × 400 × 250 mm^3, yielding an isotropic resolution of 3.1 mm^3 (128 × 128 × 80 imaging matrix). A parallel imaging with generalized auto-calibrating partially parallel acquisition (GRAPPA) [128] factor 2 and 40% phase oversampling was used, yielding a total acquisition time of 16 seconds for an acquisition with two averages. For all scans, predefined default shim settings (tune up) were used.

4.2.5 Flip angle optimization

Measurements were performed for both normoxic and hyperoxic gas conditions for a set of flip angles (12°, 15°, 18°, 21°, 24°, and 27°) in order to derive an adapted ufSSFP MRI protocol providing optimal bSSFP signal intensity. To this end, for each flip angle and both O_2 concentrations, three ufSSFP scans were recorded at functional residual capacity (FRC) to bypass involuntary small discrepancies between the acquired end-expiratory phases. The volumetric scans were then randomized in order to mitigate any possible bias in the semi-automated volume segmentation. Furthermore, the datasets were median filtered (kernel size 5 × 5 × 5) to reduce sparse signals from vasculature overlying the pulmonary tissue [142]. After these two steps, the mean parenchymal SI was derived from the segmented volume and logically reordered as a function of the associated breathing gas and flip angle, and finally averaged for each flip angle and for each gas condition.

4.2.6 Signal intensity variability at functional residual capacity

Oxygen-enhanced MRI requires at least two datasets, one recorded in normoxic and one in hyperoxic condition [Eq. (4.1)]. Even for acquisitions at end-expiratory breath-holding (FRC), the two datasets will show small, but unavoidable, differences in the breath-hold positions, yielding volume-related signal modulations which are on the same order of magnitude as the oxygen-

related signal increase. To illustrate the practical issue of equal end-expiratory breath-holding (FRC) and its subsequent possible bias on oxygen-enhanced MRI, three datasets were acquired in normoxic condition (referred to as A_1, A_2, A_3) and three datasets in hyperoxic condition (O_1, O_2, O_3). Each of the three normoxic acquisitions can be combined with one of the three hyperoxic acquisitions to calculate the oxygen-enhancement, resulting in a total of 9 combinations to calculate the oxygen-enhancement (A_1O_1; A_1O_2; A_1O_3; A_2O_1; A_2O_2; A_2O_3; A_3O_1; A_3O_2; A_3O_3). For each combination, the whole lung oxygen-enhancement [Eq. (4.1)] was calculated from the mean parenchymal SI, determined by segmentation as explained in the "Flip angle optimization" Section 4.2.5 (i.e., specific steps include: randomized data sets, median filtering, segmentation, reordering).

4.2.7 OE-MRI using the sponge model

A series of five 3D ufSSFP lung scans in normoxic condition were obtained at different breathing phases, spanning from functional residual capacity (FRC) to tidal inspiration. The same measurements were repeated for hyperoxic conditions. To ensure a relatively uniform range of lung volumes (which is not required, but desired), the volunteers followed breathing commands. For the first two scans, instructions to exhale to FRC (breathe-out) and to breathe-in to tidal inspiration were given. The three scans in respiratory phases between FRC and tidal inspiration were acquired with the following breathing commands: "breathe-in, breathe-out, one-sip / two-sips / three-sips of air, and hold", respectively. Determination of the corresponding lung volumes was achieved by semi-automated volume segmentation after randomizing the datasets, median filtering (kernel size 5 × 5 × 5), and reordering, as described before. From this, the average oxygen-enhancement in the lung tissue [cf. Eq. (4.4)] can be easily retrieved from an orthogonal regression analysis of the adapted sponge model [cf. Eq. (4.3)] to the observed volume-related average signal variations. A corresponding outline is shown in Figures 4.1a-c. Uncertainty calculations were performed by Gaussian error propagation of the uncertainties of the sponge model fitting parameters (68% confidence interval window).

For the generation of the OE-MRI maps [OE_{local}, Eq. (4.5)], the native datasets acquired at different inspiratory phases were first spatially co-registered. Amongst the five chest acquisitions under normoxic condition, the one closest to the average lung volume was chosen as a reference and was referred to as baseline acquisition of volume $\overline{V}$ [i.e., $V = \overline{V}$ in Eqs. (4.4) and (4.5)]. The four remnant air datasets as well as the five O_2 datasets were then co-registered to the baseline. All datasets were subsequently median filtered (kernel size $5 \times 5 \times 5$ voxels) and fitted voxel-wise to the linear sponge model [Eq. (4.3)] for each O_2 concentration using orthogonal regression (the lung volume was retrieved in the aforementioned segmentation process on the non-registered

images). The local oxygen-enhancement, $OE_{local}(\overline{V})$, was then calculated voxel-wise [cf. Eq. (4.5)]. For a schematic summary, see Figures 4.1d-f.

The effect of the image registration on OE-MRI was analyzed from a direct comparison of the whole lung oxygen-enhancement before and after image registration. Moreover, as a negative control, the signal enhancement obtained from two normoxic phases of five multi-volumetric acquisitions each was calculated for one subject [cf. Eq. (4.4) and Eq. (4.5)].

For data visualization, data analysis, and simulations Python 2.7 was used (Anaconda Python distribution, Continuum Analytics, version 2.0). Segmentation of the lung was performed semi-automatically by a trained observer who used a region growing tool implemented in MITK (The Medical Imaging Interaction Toolkit 2014.03.0, Heidelberg, Germany). The lung datasets were co-registered using a mass preserving 3D deformable B-spline image registration algorithm (elastix version 4.7, University Medical Center Utrecht, The Netherlands) [145, 168].

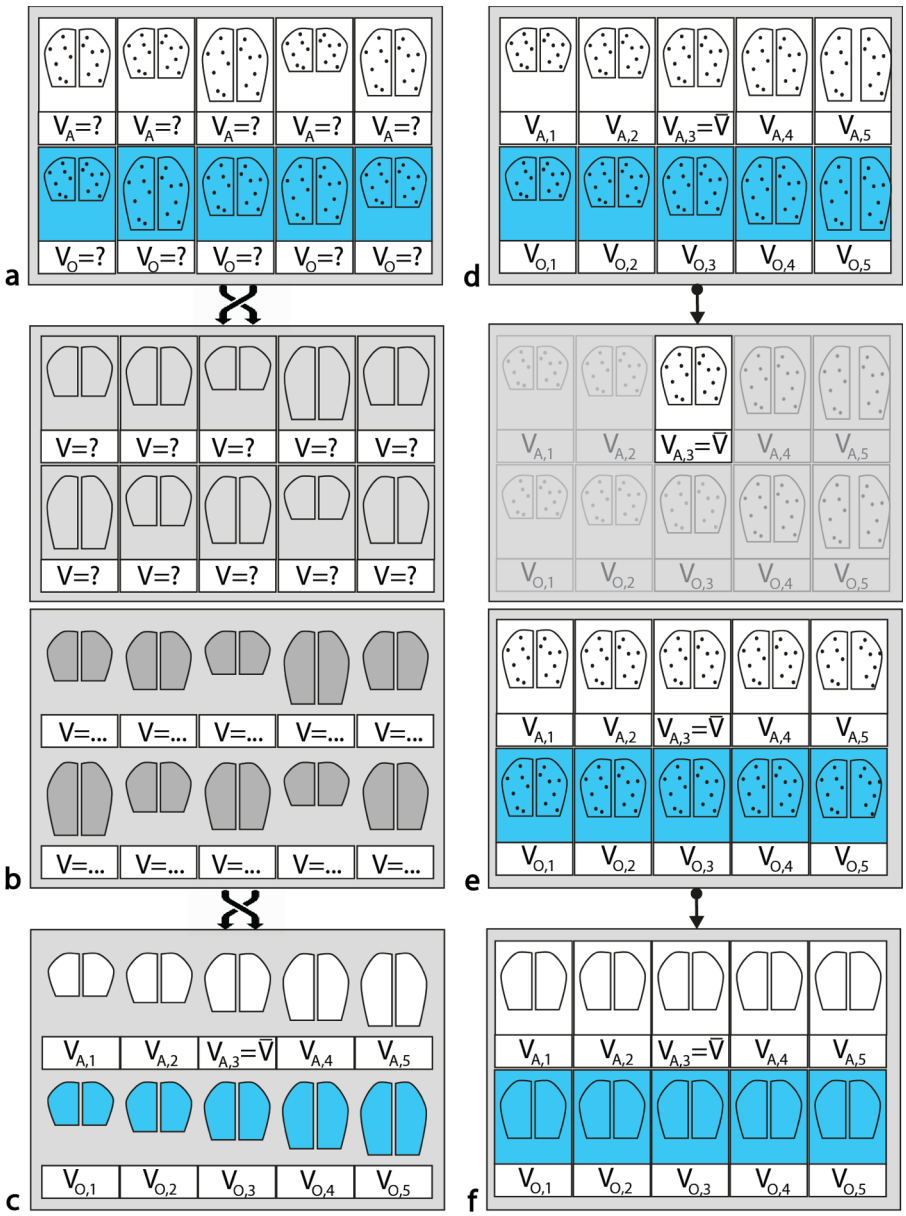

Figure 4.1. Schematic of the oxygen-enhancement calculation process. (a) Two multi-volumetric sets (five normoxic and five hyperoxic scans) were acquired from functional residual capacity (FRC) to tidal inspiration. (b) The datasets were subsequently shuffled (blinded to investigator), median filtered (to remove the overlying vascular signal), and the lung volumes were determined by semi-automatic segmentation. (c) The segmented and median-filtered datasets were ordered with respect to their lung volumes ($V_{A,i}$ for air, $V_{O,i}$ for oxygen). The whole lung mean signals (SI_i) in the segmented region of interests (V_i) were used to calculate the whole lung oxygen-enhancement OE_{global} (Eq. (4.4), unregistered images), using the sponge model [Eq. (4.3)]. (d) The multi-volumetric datasets were ordered according to their volumes [using the information gained in (b)]. (e) All dataset were then co-registered to the normoxic scan of volume $\bar{V}$, which is the one with minimum volume deviation from the average lung volume. (f) After median filtering, the oxygen-enhancement (OE_{local}) is derived voxel-wise from Eq. (4.5), as well as the whole lung mean oxygen-enhancement (OE_{global}, registered images)

4.3 Results

Illustrative native and median filtered ufSSFP lung images at FRC are shown in Figure 4.2 under both normoxic and hyperoxic conditions for a flip angle of 23°. Because of the very short TR, no banding artifacts are visible in the lung parenchyma and vasculature is well recognizable in the native images (Figs. 4.2a and 4.2b). Median filtering removes the sparse hyperintense vascular signals (Figs. 4.2c and 4.2d) to recover the underlying smooth parenchymal background signal variation, e.g., the ventral to dorsal density variation (cf. sagittal slices in Fig. 4.2) due to gravitational effects [65].

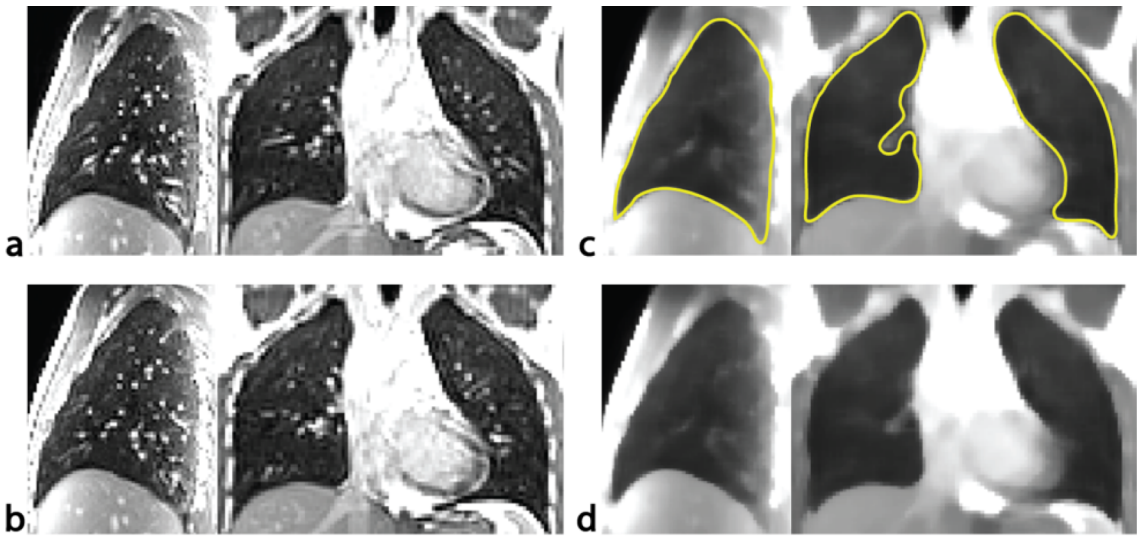

Figure 4.2. (a,b) Illustrative sagittal and coronal chest images obtained using 3D ufSSFP scans at FRC while breathing (a) air and (b) 100% oxygen (α = 23°). (c,d) Corresponding images after 3D median filtering and segmentation (yellow outline) for estimation of the parenchymal mean signal intensity and lung volume.

4.3.1 Flip angle optimization

The low proton density and consequently low signal-to-noise ratio (SNR) of the lung parenchyma makes MR imaging challenging. Moreover, the O_2-related signal increase while breathing pure oxygen is barely recognizable by direct visual comparison (cf. Figs. 4.2c to 4.2d). As a result, the flip angle of ufSSFP pulse sequence was varied to find its optimal value providing maximal whole lung signal intensities for both gas conditions (Fig. 4.3). A qualitatively good correspondence between the measured signals and the bSSFP signal model [163] is observed. For both gas conditions, the signal of ufSSFP is maximal for flip angles around 20° to 25°, yielding an overall O_2-enhancement between 5% ± 3% (mean ± SD) and 7% ± 3%. As a result, a flip angle of α = 23°

was chosen for OE-adapted ufSSFP scans. Similar results were found for all the healthy volunteers. The overall observed oxygen-related signal enhancement is in agreement with simulations (cf. "Method" Section 4.2) predicting an oxygen-enhancement of 3% to 8% for flip angles α around 20°-27°.

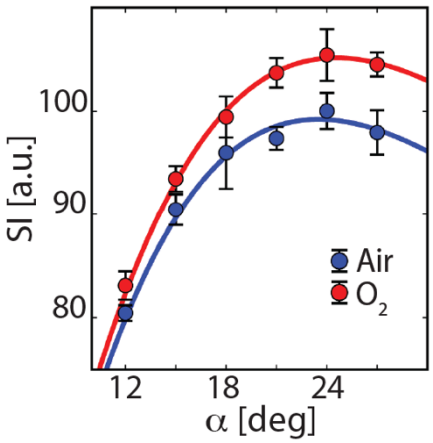

Figure 4.3. Observed average signal of the lung parenchyma as a function of the flip angle measured in a volunteer for both air and 100% oxygen. The average lung mean SI refers to the average of three acquisitions and the error bars represent its standard deviation. An analysis with the common bSSFP signal model (solid lines) yields $T_1/T_2 \approx 26$ for air, $T_1/T_2 \approx 24$ for oxygen, and $M_0 = 665$ for both gases. The relative T_1/T_2 decrease between normoxic and hyperoxic conditions is 8%.

4.3.2 Signal intensity variability at functional residual capacity

Generally, OE-MRI requires (at least) two datasets, recorded under different gas conditions. As a result, the scans show small, but unavoidable, involuntarily different breath-hold positions even at end-expiration, as outlined in Figures 4.4a and 4.4b for normoxic and hyperoxic breathing. For the six scans, the observed average lung signals were 96 (arbitrary units [a.u.]), 101 [a.u.] and 102 [a.u.] while breathing air, and 103 [a.u.], 105 [a.u.] and 108 [a.u.] while breathing O_2. Since the overall O_2-enhancement is small (in the average from 100 ± 3 [a.u.] for air to 105 ± 3 [a.u.] for O_2), even marginal lung volume differences will lead to signal modulations of comparable strength. This leads to a large variability and thus imprecise quantification of the O_2-enhancement from only two datasets, as exemplarily demonstrated in Figure 4.4c. For all nine possible pairwise combinations resulting from the three normoxic and the three hyperoxic scans, the mean whole-lung O_2-enhancement spans from 1.0% to 12.5% [with an average O_2-enhancement of 5.8% ± 3.7% (mean ± SD)]. For reliable and reproducible OE-MRI, residual SI-volume modulations must be taken into account and can be addressed by the sponge model.

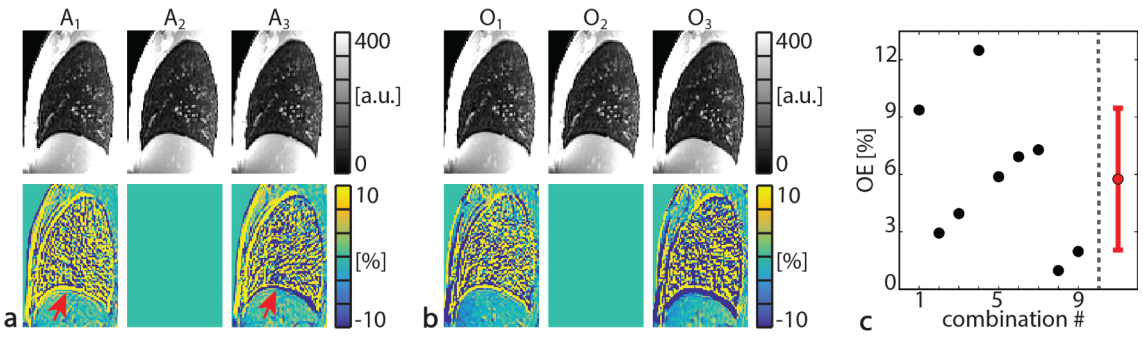

Figure 4.4. (a, top) Representative 3D ufSSFP sagittal views of the same slice acquired three times consecutively in end-expiration (FRC) while breathing air. (a, bottom) Relative difference maps between the baseline (A_2) and the target images (A_1 and A_3) accentuating the respiratory phase mismatch (e.g., diaphragm position depicted by the red arrows and lung boundaries) as well as the modulation of the lung signal occurring at similar but different FRC volumes (2550±80 cm^3, mean±SD of the three measurements). (b) As (a), but in hyperoxic conditions. (c) Nine combinations of whole lung oxygen-enhancement resulting from three scans in normoxic (a) and three in hyperoxic (b) conditions at FRC (see "Methods" Section 4.2.6). On the right, the mean and the standard deviation resulting from the nine combinations are indicated using a red color bar.

4.3.3 OE-MRI using the sponge model

Scanning was performed for five variable breath-hold positions around the tidal volume region, as presented in Figure 4.5a. For better visualization of the differences in the respiratory phases, relative SI difference maps are shown in Figure 4.5b (with respect to the scan taken at middle respiratory phase, volume $\overline{V}$). The relative difference maps accentuate the diverse lung parenchyma signal levels and the structural misalignments due to the different inspiratory volumes. In Figure 4.5c, relative signal intensity difference maps are shown after image registration. Image registration does not affect lung signal intensity; it resolves structural mismatches such as vessels, diaphragm position, lung boundaries and corrects for through-plane motion. In contrast to the moderate SI variation observed at FRC (cf. Fig. 4.4a), in the tidal breathing region the pulmonary signal ranged from 109 [a.u.] to 83 [a.u.], for corresponding lung volumes ranging from 2381 to 3075 cm^3. This is in contrast to the liver SI which remains constant (240 ± 3 [a.u.]) since it does not expand or contract. The background noise level [η, cf. Eq. (4.2)] was about 3 ± 2 [a.u.].

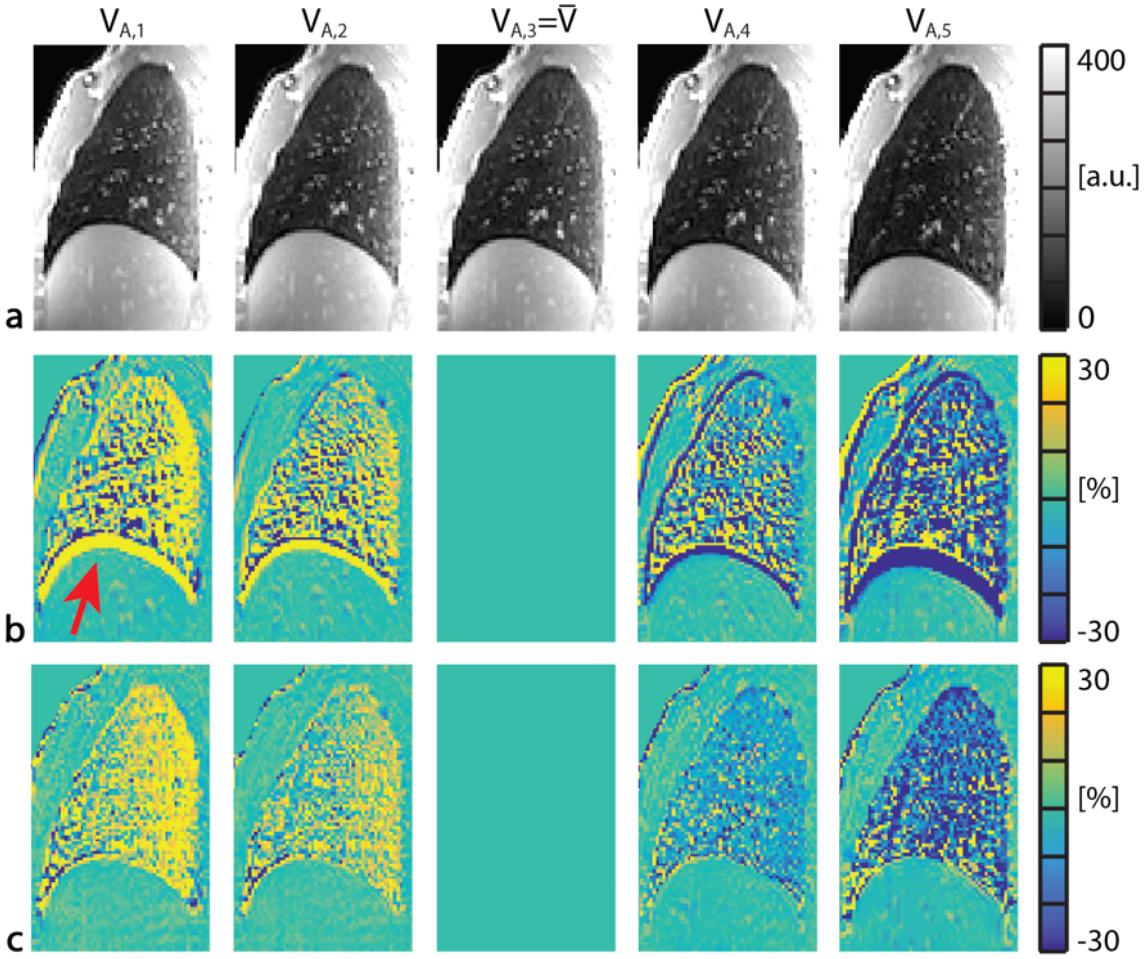

Figure 4.5. (a) Representative 3D ufSSFP sagittal views acquired at five different tidal volumes in normoxic condition. The datasets are ordered from left to right according to their lung volume (i.e., from FRC to tidal inspiration; cf. Fig. 4.1d). The middle volume scan, i.e., V_3 (referred to as volume $\bar{V}$), served as baseline for the registration process (cf. Fig. 4.1e). (b) Relative signal intensity difference maps between the baseline and the moving images (to be registered) accentuating the parenchymal signal intensity modulations, differences in the diaphragm position (e.g., red arrow) and lung structures due to the respiratory phase mismatch. (c) Corresponding relative signal intensity difference maps after image co-registration, revealing lung structural alignment while preserving the signal intensity.

The average, median-filtered, lung signal is shown for a representative volunteer in Figure 4.6 as a function of the lung volume for both normoxic and hyperoxic conditions and for both non-registered and registered datasets. An analysis with the linear sponge model yields for the non-registered datasets, $C_{0,Air} = (197.4 \pm 0.6)[a.u.]$, $C_{1,Air} = (37.2 \pm 0.2)[L^{-1} \cdot a.u.]$, $C_{0,O2} = (209.6 \pm 1.2)[a.u.]$, $C_{1,O2} = (39.4 \pm 0.4)[L^{-1} \cdot a.u.]$, whereas for the registered datasets $C_{0,Air} = (191.6 \pm 0.7)[a.u.]$, $C_{1,Air} = (35.4 \pm 0.2)[L^{-1} \cdot a.u.]$, $C_{0,O2} = (204.5 \pm 1.2)[a.u.]$, $C_{1,O2} = (37.6 \pm 0.4)[L^{-1} \cdot a.u.]$. For non-registered datasets, a whole lung O_2-enhancement [OE_{global}, Eq. (4.4)] of 6.7% ± 2.0% (mean ± uncertainty) was observed for a mean lung

volume $\overline{V}$ of 2821 cm^3 (see "Methods" Section 4.2.7 for the definition of $\overline{V}$). After registration, the whole lung oxygen-enhancement was 7.3% ± 2.2% (at $\overline{V}$ = 2821 cm^3).

It is observed that the oxygen-enhancement values from the sponge model were nearly independent of the lung volume: for the volunteer presented in Figure 4.6, at FRC (V = 2381 cm^3), the OE_{global} without registration was 6.6% ± 1.6% (with registration 7.2% ± 1.7%), whereas at tidal inspiration (V = 3075 cm^3), the oxygen-enhancement without registration was 6.9% ± 2.4% (with registration 7.5% ± 2.6%). This is expected, since in the tidal breathing region (e.g., $V = V_{ref} \pm \delta V \approx 2.4 \pm 0.4$ [L]), $\left|1 - \frac{OE_{global}(V_{ref} \pm \delta V)}{OE_{global}(V_{ref})}\right| < 0.1$ for variations $\delta V < \frac{V_{ref}}{6}$ using for example $C_{1,Air} \approx C_{1,O2} \approx 36$ [L^{-1} · a.u.], $C_{0,Air} \approx 190$ [a.u.] and $C_{0,O2} \approx 200$ [a.u.].

The OE_{global} results, determined with the sponge model at FRC, $\overline{V}$ and tidal inspiration, are summarized in Table 4.1 for the four healthy volunteers examined (Volunteer #4 refers to the case analyzed in Figure 4.6). Without registration, an average oxygen-enhancement of 6.5% ± 0.2% (mean ± intersubject SD) with an average intrasubject uncertainty of ±2.1% was measured. After registration, the four volunteers showed an average oxygen-enhancement of 7.0% ± 0.3% with an average intrasubject uncertainty of ±2.3%. In all the volunteers, the oxygen-enhancement is nearly independent from the lung volume (cf. Table 4.1).

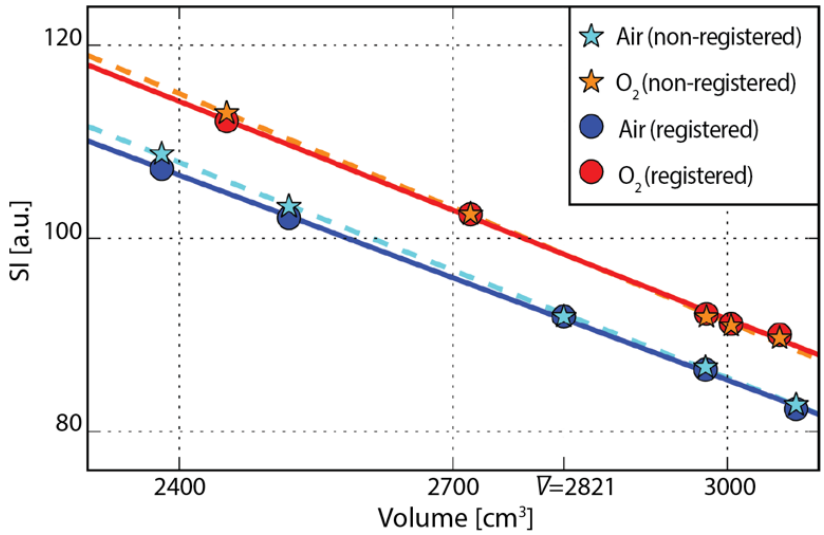

Figure 4.6. Mean signal intensity of the lung parenchyma as a function of the lung volume measured in a healthy volunteer for both normoxic (blue colors) and hyperoxic (red colors) conditions and for both native median-filtered datasets (non-registered, star signs) and registered median-filtered datasets (circles). The lines show the corresponding fit to the linear sponge model (dashed line: non-registered images, solid line: registered images). The lung volume of the acquisition used as baseline for the image registration is $\bar{V}$ = 2821 cm^3, as depicted in the figure

Table 4.1. Measured lung volumes at FRC, $\overline{V}$ and tidal inspiration, and the corresponding whole lung oxygen-enhancements (mean ± uncertainty) for both non-registered and registered datasets. The group mean and intersubject standard deviation are also given. Volunteer #4 refers to the subject analyzed in Figure 4.6.

Subject		Lung volume cm^3			OE_{global}, non-registered data [%]			OE_{global}, registered data [%]		
		FRC	$\overline{V}$	Tidal Insp.	OE(FRC)	OE($\overline{V}$)	OE(Insp.)	OE(FRC)	OE($\overline{V}$)	OE(Insp.)
#1	Air	2807	3320	3688	6.3±1.7	6.2±2.2	6.1±2.5	7.0±2.2	6.8±2.5	6.6±2.6
	O_2	2769		3660						
#2	Air	2555	2793	3032	6.2±1.5	6.4±1.8	6.6±2.4	6.5±1.9	6.6±2.0	6.7±2.4
	O_2	2603		3092						
#3	Air	2090	2416	2988	6.7±1.8	6.5±2.3	6.1±2.7	7.2±1.8	7.1±2.5	6.9±2.8
	O_2	2138		2908						
#4	Air	2381	2821	3075	6.6±1.6	6.7±2.0	6.9±2.4	7.2±1.7	7.3±2.2	7.5±2.6
	O_2	2452		3057						
Mean	Air	2458	2837	3196	6.5±0.2	6.5±0.2	6.4±0.4	7.0±0.3	7.0±0.3	6.9±0.4
	O_2	2495		3179						

Finally, exemplary OE-MRI maps of the lungs are presented in Figures 4.7. For all four volunteers, coronal, axial and sagittal slices are shown. Generally, a pronounced increase in the oxygen-enhancement from non-dependent (ventral) to dependent (dorsal) lung areas is observed, as well as "patchy" heterogeneities. The heterogeneities are increased especially in regions characterized by partial volume effects, physiological motion, and steep proton density gradients (e.g., in the pericardial areas, at the periphery of the lungs next to the rib cage or near vasculature and airways). Further oxygen-related signal enhancement can be located in the pulmonary veins, left heart, aortic blood pool (O_2-enhancement aortic arch ≈ 5%), renal cortex, and spleen (not shown). In contrast, no signal enhancement emanates venous blood (hypoxic) returning from the body, such as in the vena cava, left ventricle, left atrium, pulmonary arteries, and in the liver.

The specificity of the proposed approach to detect O_2-related signal enhancements is shown in Figure 4.8, reflecting OE-MRI maps calculated from two series of five acquisitions each, but performed both in normoxic conditions. As expected, the observed whole lung signal enhancement is almost zero: 0.2%±2.0 % (mean ± uncertainty) for the non-registered datasets, and 0.4% ± 2.3% (mean ± uncertainty) for the registered datasets. Consequently, the sponge model successfully removes possible volume-related signal modulations from multi-volumetric data acquisitions as used for OE imaging.

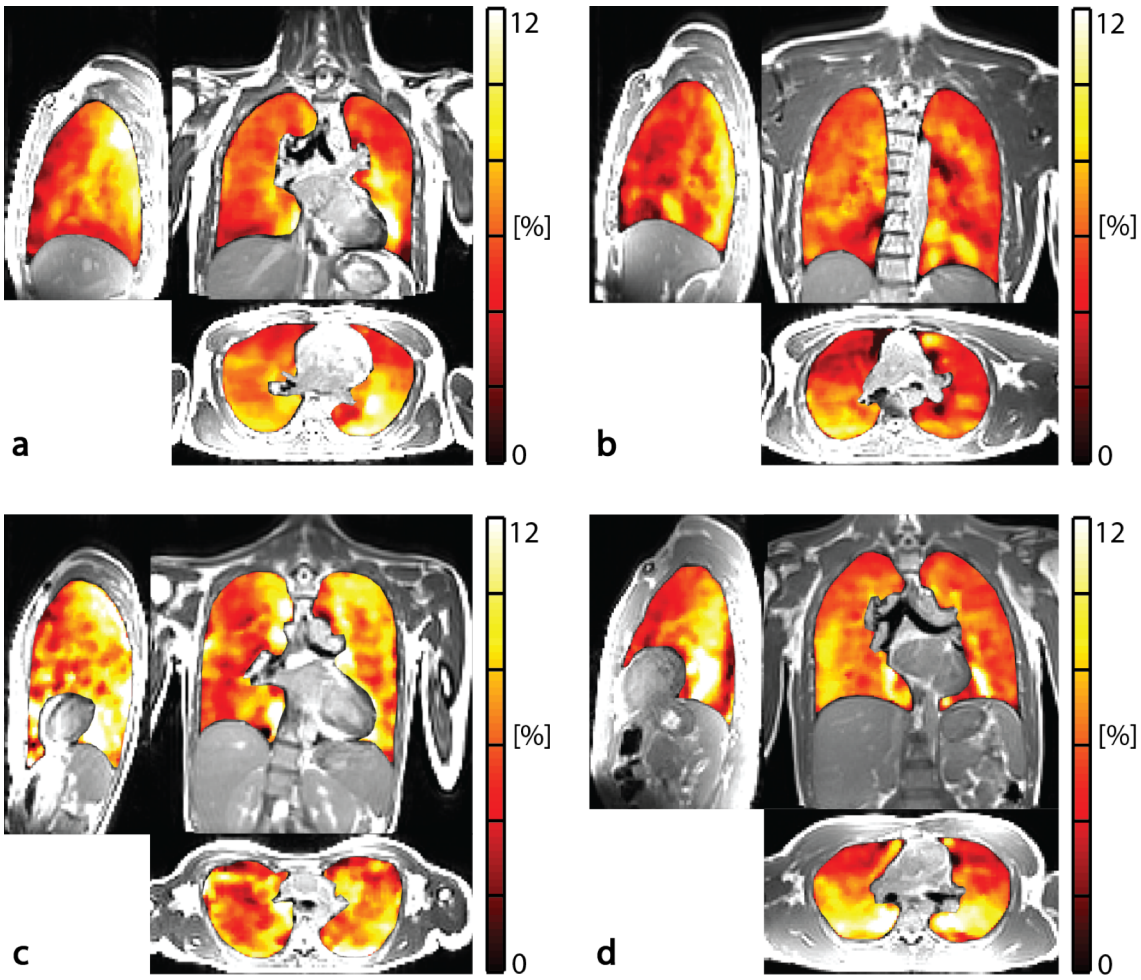

Figure 4.7. Lung oxygen-enhancement maps overlaid on structural images in sagittal, coronal, and axial views obtained in two healthy volunteers. The whole lung oxygen-enhancements (OE_{global}, registered datasets) are (a) 6.8%, (b) 6.6%, (c) 7.1% and (d) 7.3% (cf. Table 4.1, Volunteers 1-4).

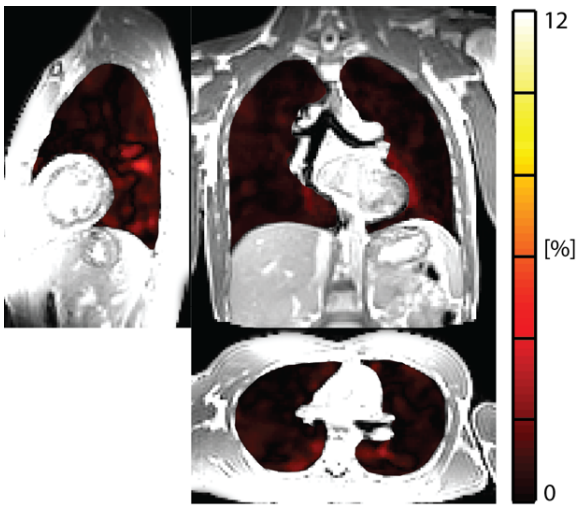

Figure 4.8. Signal intensity enhancement map (absolute value) obtained as a negative control from two phases while breathing air (Volunteer #4, cf. Fig. 4.7d). The mean "enhancement" OE_{local} is 0.4% ± 2.3%.

4.4 Discussion

In this work, we demonstrated the feasibility of 3D OE-MRI of the lung from two multi-volumetric sets of ultra-fast SSFP scans acquired in normoxic and hyperoxic gas conditions. A sponge model was used to take into account and mitigate oxygen-unrelated signal modulations associated with diverse breath-hold positions. In agreement with simulations, a mean whole lung oxygen-enhancement of 6.5% ± 0.2% (mean±SD, non-registered datasets) was observed for the four healthy volunteers, revealing limited intersubject variability. In healthy subjects, the derived OE-MRI maps exhibit a marked gravitation-related signal enhancement from anterior to posterior lung, in accordance with 2D OE-MRI [70] and similarly to well-established functional techniques such as SPECT, DCE-MRI or arterial spin labeling [66, 136, 169, 170]. Moreover, the signal from oxygenated blood (e.g., aorta) is also increased, representing the physiological validation of dissolved molecular O_2 and indicating that OE lung MRI with ufSSFP is weighted by both perfusion and ventilation.

In the proposed framework, OE-MRI is based on lung images acquired in the tidal respiratory volume region to achieve close-to-maximum parenchymal signal levels, but also to mitigate registration issues related to the requirement of large deformations fields, e.g., if scans were performed from forced expiration to total lung capacity. As a result, good registration accuracy could be achieved as confirmed by the qualitative visual assessment of selected landmarks (e.g., diaphragm position in Fig. 4.5c) and by the whole lung SI preservation (cf. Fig. 4.6). Overall, a rather marginal lung signal intensity change due to image registration was observed. Nevertheless, as a consequence of the limited oxygen-related signal enhancement of only a few percent (6.5% for the non-registered datasets, cf. Table 4.1), registration resulted in a detectable but moderate effect on the whole lung oxygen-enhancement (increased from 6.5% to 7.0%).

The feasibility of 3D OE-MRI of the lung has been recently demonstrated by Kruger et al. [158] and Hemberger et al. [171] using free-breathing respiratory-gated 3D radial ultra-short echo-time (UTE) pulse sequences. In this approach, the OE-MRI maps are derived based on only two matched volumetric sets, one set for each O_2 concentration (21% and 100% O_2). In comparison, the use of rapid breath-hold ufSSFP acquisitions at different inspiratory levels in combination with the sponge model mitigates oxygen-unrelated contributions from lung density modulations at different respiratory positions (lung volumes), thus improving the overall reliability of the oxygen-enhancement measure. As further advantage of the multi-volumetric approach, we consider its ability to provide simultaneously with oxygen-enhancement mapping also ventilation-weighted α-maps, which are sensitive to ventilation abnormalities in patients as presented in Chapter 3. Moreover, especially in the context of imaging anatomical regions with intrinsically

low proton density like the lung, the ability of balanced SSFP [45] to provide higher SNR compared to spoiled SSFP sequences (e.g., UTE) is beneficial.

A rigorous assessment of the repeatability of the oxygen-enhancement was not investigated in this work, but good reproducibility of the sponge model was observed for normoxic conditions (cf. Chapter 3). Although the sponge model requires short breath-holding at several inspiratory levels, these maneuvers are well tolerated and performed by patients (cf. Chapter 3 and Chapter 6). As a result, OE-MRI with the sponge model should be feasible also in the clinical setting and specific to O_2-related signal changes in impaired lung regions (e.g., emphysema, bullae, air trapping, fibrosis).

Here, we used the sponge model to capture volume-related balanced SSFP signal modulations in combination with the administration of oxygen. However, the proposed methodology could be easily adapted to other contrast agents such as gadolinium-based ones. Furthermore, the methodology could be used in combination with other basic pulse sequences (e.g., UTE) or by using self-navigated free breathing methods [155, 156] being able to provide multi-volumetric lung images; these imaging acquisitions might be required in patients with limited breath-holding capabilities or for infants. Moreover, currently, our method requires a semi-automatic lung segmentation to retrieve the lung signal volume-dependencies for the sponge model analysis. Obviously, for large-scale studies, a fully automatic lung segmentation algorithm, such as the one recently presented by Kohlmann et al. [153] and by Tustison et al. [154] might be required, but the achievable accuracy needs to be investigated.

4.5 Conclusions

We have shown that simple multi-volumetric ufSSFP breath-hold scans at different inspiratory phases under both normoxic and hyperoxic gas conditions in combination with a sponge model provides improved reliability and accuracy for 3D oxygen-enhancement mapping, since the parenchymal volume-related signal modulations are taken into account. This might ease the use of OE-MRI to evaluate disease progression and monitor therapeutic responses. However, clinical evaluation on a large population group is needed to further validate the robustness, reproducibility, and diagnostic potential of the proposed technique.

CHAPTER 5

Dynamic and steady-state oxygen-dependent lung relaxometry using inversion recovery ultra-fast SSFP imaging at 1.5T

A modified version of this chapter has been published as:

Pusterla O*, Bauman G*, Santini F, Bieri O. *Dynamic and steady-state oxygen-dependent lung relaxometry using inversion recovery ultra-fast steady-state free precession imaging at 1.5 T.* Magn Reson Med, 2018, 79:839–845.

*Equally contributed to this work.

CHAPTER ABSTRACT

Purpose: To demonstrate the feasibility of oxygen-dependent relaxometry in human lung using an inversion recovery ultra-fast steady-state free precession (IR-ufSSFP) technique.

Methods: ECG-triggered pulmonary relaxometry with IR-ufSSFP was performed in seven healthy human subjects at 1.5T. The data were acquired under both normoxic and hyperoxic conditions. In a single breath-hold of less than 9 seconds, 30 transient state IR-ufSSFP images were acquired, yielding longitudinal (T_1) and transversal (T_2) relaxometry parameter maps using voxel-wise nonlinear fitting. Possible spatial misalignments between consecutive IR-ufSSFP parameter maps were corrected using elastic image registration. Furthermore, dynamic relaxometry oxygen wash-in and wash-out scans were performed in one volunteer. From this, T_1-related wash-in and wash-out time constants (τ_{wi}, τ_{wo}) were calculated voxel-wise on registered maps using an exponential fitting model.

Results: For healthy lung, observed T_1 values were 1399±77 ms and 1290±76 ms under normoxic and hyperoxic conditions, respectively. The oxygen-related reduction of T_1 was statistically significant in every volunteer. No statistically significant change, however, was observed in T_2, with normoxic and hyperoxic T_2 values of 55±16ms and 56±17ms, respectively. The observed average τ_{wi} was 87.0±28.7 s, while the average τ_{wo} was 73.5±21.6 s.

Conclusion: IR-ufSSFP allows fast, steady-state and dynamic oxygen-dependent relaxometry of the human lung.

5.1 Introduction

Introduced already in the mid-1990s, oxygen-enhanced (OE) proton magnetic resonance imaging (MRI) of the lung was proposed as an alternative technique for the assessment of lung function [95]. In contrast to the hyperpolarized gas lung MRI [11, 37], OE-MRI does not rely on specialized hardware and can be easily performed using a standard clinical equipment. OE-MRI is based on the paramagnetic properties of O_2, changing lung tissue relaxivity. When breathed, oxygen acts as a weak contrast agent in the lung by shortening the longitudinal relaxation time (T_1) [96] and the apparent transverse relaxation time (T_2*) [158]. The observed reduction in T_1 under the pulmonary hyperoxia is attributed to an increased concentration of dissolved O_2 in blood vessels and lung parenchyma [95], thereby reflecting oxygen uptake (wash-in). OE-MRI is usually considered an indirect measure for ventilation, diffusion and perfusion using T_1-weighted images [99]. If one of those functions is regionally affected, a change in a signal enhancement can be detected locally. In contrary, no changes in the transverse relaxation time (T_2) in the lung parenchyma are expected in the hyperoxic condition, since T_2 of the arterial blood remains unchanged [164]. Furthermore, an increased concentration of O_2 has been shown to reduce T_2* in the lung by increasing the magnetic susceptibility of gas and blood in alveoli and thus can be used as a measure of ventilation [99, 101].

Hence, oxygen-dependent pulmonary relaxometry can be applied to measure the differences in relaxation times between the normoxic and hyperoxic conditions or to observe dynamic changes of tissue relativity, and potentially yield a useful diagnostic information. Only a small number of studies using quantitative oxygen-dependent T_1 relaxometry in patients with diseases such as cystic fibrosis [172], chronic obstructive pulmonary disease [114], chronic lung allograft dysfunction [173] or asthma [98] have been reported so far.

Most of the OE-MRI relaxometric techniques are based on either an inversion recovery (IR) snapshot fast low angle shot (FLASH) [93] or an IR half Fourier acquired single shot turbo spin echo (HASTE) [92] method. More recently, a radial acquisition technique with ultra-short echo (UTE) times has been presented for both for simultaneous T_1 and T_2* mapping of the lung [99]. The UTE approach provides improved signal-to-noise ratio in the lung parenchyma and shows inherent robustness against motion and pulsation artifacts.

As an advantage over spoiled gradient echo based sequences, balanced steady-state free precession (bSSFP) sequences offer the highest signal-to-noise ratio per unit of time amongst all MRI techniques [108]. Hence, in the recent years, bSSFP imaging has found an application in structural as well as functional lung imaging [47, 102, 174–177]. Specifically, an accelerated

implementation of the bSSFP, referred to as ultra-fast SSFP (ufSSFP), has shown to be well-suited for pulmonary imaging [45]. Optimization of RF pulse excitation timings and gradient switching patterns of the ufSSFP pulse sequence as well as application of partial echo readouts and ramp sampling techniques helped to substantially reduce the TR. Consequently, the shortened TR helped to mitigate banding and motion artifacts, and resulted in a substantial increase in the parenchymal signal. Recently, a derivate of the pulse sequence termed inversion recovery ultra-fast steady-state free precession (IR-ufSSFP) was presented for pulmonary relaxometry [46]. The technique allowed for fast, simultaneous and automatic mapping of T_1, T_2, and relative spin density M_0 in human lung at 1.5T. In this work, we demonstrate the feasibility of oxygen-dependent pulmonary relaxometry using IR-ufSSFP imaging and explored the influence of pulmonary hyperoxia on relaxivity of the lung tissue in a group of healthy volunteers.

5.2 Methods

5.2.1 Pulmonary relaxometry with IR-ufSSFP

Recently, a technique termed inversion recovery ultra-fast steady-state free precession (IR-ufSSFP) technique [46] was proposed for simultaneous measurement of T_1, T_2 and M_0 in the lung parenchyma. The acquisition scheme was based on an ECG-triggered two-dimensional (2D) time-resolved transient ufSSFP imaging preceded by a nonselective adiabatic hyperbolic-secant inversion pulse. Two time-resolved IR-ufSSFP blocks containing a user defined number of images were acquired during a single breath-hold. The start of the acquisition was triggered by patient's ECG signal at the beginning of the diastolic phase. The imaging blocks were separated by a time interval (TW~3 seconds) for the full recovery of the magnetization acquired during a single breath-hold. Furthermore, the second block was repeated with several dummy repetition times between the inversion recovery and the start of the acquisition block. Thus, the acquisition scheme produces two interleaved sets of images for improved sampling of the transient ufSSFP signal. For details and an in-depth description of the IR-ufSSFP technique, cf. Bauman et al [46].

5.2.2 Imaging procedure

Experiments were performed on a 1.5T MR-scanner (MAGNETOM Avanto-Fit, Siemens Healthineers, Erlangen, Germany) with peak gradient amplitude of 45 mT/ms and a maximum slew rate of 200 T/m/s using a 12-channel thorax and a 24-channel spine coil receive-array. All scans were performed with predefined default shim settings (tune-up mode).

Seven healthy human subjects were scanned in supine position using ECG-triggered 2D IR-ufSSFP sequence. The study was approved by the ethics committee. Written informed consent was obtained from all volunteers.

The imaging parameters of IR-ufSSFP were as follows:

- in-plane resolution = 2.8 mm
- field-of-view = 450 × 450 mm^2, slice thickness (ST) = 10 mm
- matrix size = 160 × 160
- asymmetric echo sampling: echo time (TE) / repetition time (TR) = 0.71 / 1.63 ms
- two acquisition blocks with 15 images each, acquisition time (TA) per image = 150 ms
- time between acquisition blocks (TW) = 3 seconds
- total scan time per slice = 9 seconds
- 10 dummy TRs after the second inversion recovery pulse
- bandwidth = 1955 Hz/pixel
- sinc-shaped radio-frequency (RF) pulse: 1.6 time-bandwidth product, 400 µs duration
- nominal flip angle α = 45°
- parallel imaging with generalized auto-calibrating partially parallel acquisition (GRAPPA) [128] factor = 2

The imaging protocol comprised three coronal, and two sagittal slices acquired in expiratory breath-hold. Each slice was acquired during a separate breath-hold. Scanning was repeated two times. The first scan was performed while the subjects breathed medical air with 21% oxygen (normoxic condition), whereas the second scan was acquired during supply of 100% oxygen (hyperoxic condition). Medical air and oxygen was delivered at 25 L/min through a non-rebreathing ventilatory mask with reservoir placed tightly over the subject's nose and mouth. After switching to 100% oxygen, a 4 minute long delay was used prior to the second scan, in order to achieve steady-state conditions for the pulmonary IR-ufSSFP under hyperoxia. Furthermore, to assess the reproducibility of the technique, the imaging protocol was repeated on 5 consecutive days in one volunteer.

In one volunteer a set of IR-ufSSFP acquisitions was performed during the dynamic oxygen wash-in phase, during the steady-state of pulmonary hyperoxia, and during the oxygen wash-out phase. Several additional acquisitions were performed prior to the wash-in phase. In order to sample each phase, IR-ufSSFP scans were performed in expiratory breath-hold approximately

every 30 seconds for more than 15 minutes. Dynamic scanning was repeated separately in coronal and sagittal orientation.

5.2.3 Generation of the parameter maps

Only images acquired in the diastolic phase were selected for post-processing based on the time recorded after the ECG-trigger. The number of images acquired in the diastolic phase was in the range of 14-18. Subsequently, a voxel-wise nonlinear fitting of the transient ufSSFP signal using a model proposed by Schmitt et al. [178, 179], was performed on the sorted image time-series obtained from both acquisition blocks. As a result, the relative spin density (M_0), and T_1 and T_2 values were derived.

For improved accuracy of the parameter maps, a correction for 2D slice profile effects was performed, as presented in Ehses et al [180] and subsequently modified by Santini et al [181], using a dictionary-based approach. Furthermore, the inversion pulse efficiency was taken into the account as proposed by the Kellman et al [182]. Post-processing and fitting procedures was performed directly on the scanner using IceLuva scripting framework [183].

Parameter maps, acquired in the same slice position during different gas-breathing conditions, were registered to eliminate the displacement of the diaphragm and pulmonary structures. Such displacement is often present due to the difficulty to reproduce an identical breathing-holding position during all scans. Registration was performed using the Advanced Normalization Toolkit [184], using a symmetric diffeomorphic registration algorithm with a cross-correlation metric. For each pair of images, the algorithm estimated a deformation that maximizes the cross-correlation metric between the reference and the uncorrected target image. For improved convergence the process was implemented in a multi-scale approach from coarse to fine resolution. Once the estimated deformation fields were calculated, the target image was warped and resampled using a B-spline interpolator.

Maps showing regional difference in T_1 and T_2 relaxation times measured during the hyperoxic condition ($T1_{\mathrm{O2}}$ and $T2_{\mathrm{O2}}$), as well as normoxic conditions ($T1_{\mathrm{air}}$ and $T2_{\mathrm{air}}$), were calculated for every volunteer using registered parameter maps from corresponding slices.

5.2.4 T_1-related oxygen wash-in and wash-out time constants

Sets of registered T_1 maps were used to assess dynamic changes in T_1 during the oxygen wash-in and wash-out phases. A conventional asymptotic exponential wash-out model was assumed and

non-linear fitting of an exponential function was performed voxel-wise on the sets of T_1 maps acquired during each phase. The three-parameter wash-in exponential function was defined as:

$$T1_{wi}(t) = Ae^{-t/\tau_{wi}} + B \quad (5.1)$$

where τ_{wi} is the T_1 wash-in time constant, and the initial values of remaining two parameters were set as $A = T1(0) - T1(N)$ and $B = T1(N)$, for time-steps $t = 0 \ldots N$.
Similarly, the wash-out was analyzed with the exponential function:

$$T1_{wo}(t) = A(1 - e^{-t/\tau_{wo}}) + B \quad (5.2)$$

where τ_{wo} is the T_1 wash-out time constant with initial fitting parameters set as $A = T1(N) - T1(0)$ and $B = T1(0)$.

5.2.5 Image analysis

The lungs were segmented in every volunteer with a region growing algorithm [131], excluding the large vessels, using a dedicated software (The Medical Imaging Interaction Toolkit, Heidelberg, Germany). Segmentation masks were used for the analysis of the T_1 and T_2 distributions. The Mann-Whitney U test was used to test for the intra-subject difference between distributions of relaxation times measured in hyperoxic and normoxic conditions, as well as to test if there was a significant difference between the distribution of the T_1-related O_2 wash-in and wash-out time constants. Paired two-sample t-test was performed to assess the mean values of relaxation times calculated for the whole group of subjects. The statistical tests were performed on the significance level of α equals 0.05. P values less than 0.05 were considered to be statistically significant. The statistical analysis and visualization of the data was performed using Matlab 2012b (MathWorks, Natick, MS, US).

5.3 Results

Illustrative thoracic coronal and sagittal T_1 and T_2 maps of a healthy volunteer are shown in Figure 5.1 for normoxic and hyperoxic conditions. Relaxometry was successful over the whole field-of-view, with the exception of regions outside the body which were subsequently masked. Overall, T_1 maps appear more homogenous than the ones of T_2. This is due to lower difference in T_1 between vessels and lung parenchyma. A subtraction of registered T_1 and T_2 maps from the same healthy subject, acquired during both steady-state gas-breathing conditions (room-air and 100%

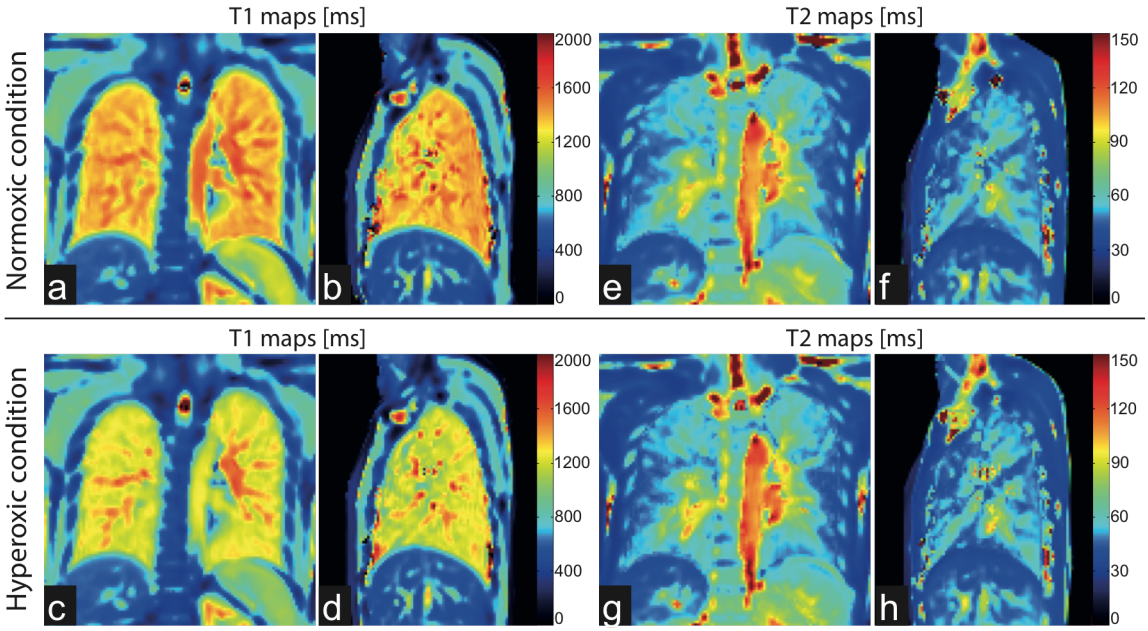

Figure 5.1. Coronal (a,c) and sagittal (b,d) T_2 maps as well as coronal (e,g) and sagittal (f,h) T_2 maps of the chest acquired under normoxic and hyperoxic conditions in Volunteer #6. A reduction of T_1 can be noticed in the lung and spleen regions on coronal images.

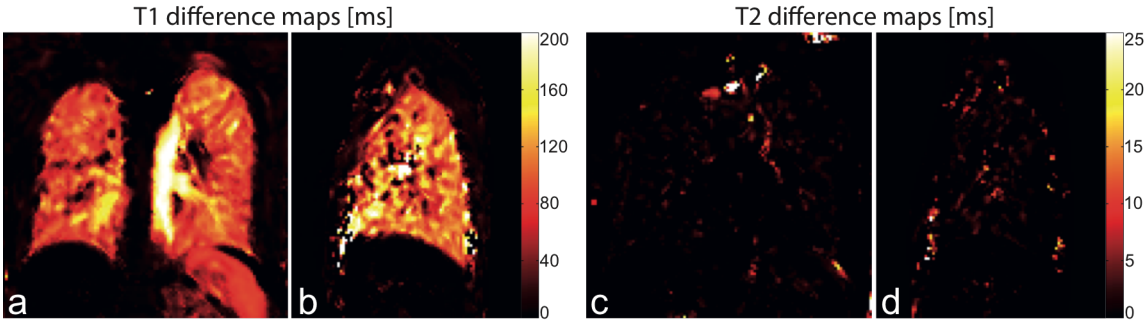

Figure 5.2. Maps showing the difference in T_1 and T_2 between the registered maps acquired during 21% O_2 and 100% O_2 gas-breathing phases in coronal (a,c) and sagittal (b,d) orientation.

O_2), yields O_2-related relaxometry difference maps, i.e., $\Delta T_1 := T1_{O2} - T1_{air}$ and $\Delta T_2 := T2_{O2} - T2_{air}$ (see Figure 5.2).

Table 5.1 summarizes the means and standard deviations of assessed relaxation times measured during hyperoxic and normoxic conditions in the lung in all healthy volunteers. The mean $\overline{T1}_{air}$ and $\overline{T1}_{O2}$ in healthy volunteers were 1399±77 ms and 1290±76 ms, respectively. The difference between the means ($\overline{T1}_{O2} - \overline{T1}_{air}$) for the whole group of subjects was 108 ms (7.8%) and was statistically significant ($P<10^{-4}$, paired two-sample t-test). The average difference between T_1 measured in both steady-state gas conditions was in the range of previously reported values

[185]. The mean $\overline{T2}_{O2}$ and $\overline{T2}_{air}$ in healthy volunteers were 55±16 ms and 56±17 ms, respectively. The difference between the means ($\overline{T2}_{O2} - \overline{T2}_{air}$) was -0.4 ms (-0.8%) and was not statistically significant (P = 0.6, paired two-sample t-test). On the intra-subject level a statistically significant difference between $T1_{O2}$ and $T1_{air}$ distributions was observed for all volunteers ($P<10^{-6}$, Mann-Whitney U test). The Mann-Whitney U test, however, showed no intra-subject difference between $T2_{O2}$ and $T2_{air}$ distributions in all volunteers; except for Volunteer #5 ($P<10^{-4}$) and during the second scan of Volunteer #7 ($P<10^{-3}$). The significant T_2 differences in those two volunteers were influenced by the imperfect ECG gating during those scans and due to the heart rate variability or overestimated length of the acquisition window. The T_1 difference in those two volunteers was not affected by the imperfect ECG-gating or heart rate variability in the same way as the T_2 difference since T_1 of blood and lung parenchyma are similar. The coefficient of variation (cv) calculated for repeated measurements in Volunteer #7 was lower for T_1 than T_2 relaxation times. For T_1, the cv was 0.0052 and 0.0064, whereas for T_2, the cv was 0.066 and 0.049 for normoxic and hyperoxic conditions, respectively.

The diagrams in Figure 5.3 show averaged T_1 values in the segmented lung parenchyma of a healthy subject measured in coronal and sagittal orientation before the administration of oxygen, during the oxygen wash-in, steady-state of pulmonary hyperoxia, and oxygen wash-out. From the observed dynamic T_1 changes, T_1-related O_2 wash-in and wash-out time constants are assessed using mono-exponential exponential fitting analysis, as indicated by the solid line in Figure 5.3. It can be noticed that the measured T_1 values fit the exponential model function better during the wash-out than the wash-in phase.

Figure 5.4 presents maps of T_1-related oxygen wash-in time constant τ_{wi} and wash-out time constant τ_{wo}. Mean τ_{wo} values in the lung were smaller than mean τ_{wi} values estimated for the voxel distributions in coronal and sagittal scans. Mean τ_{wi} measured in the segmented lung in the coronal and sagittal orientations were 80.0±18.6 s and 98.0±33.6 s, respectively, whereas mean τ_{wo} values calculated in the coronal and sagittal orientations were 67.6±13.2 s and 84.0±24.7 s, respectively. Mann-Whitney U test results showed that the differences in the mean values estimated during the wash-in and wash-out phases were statistically significant ($P<10^{-4}$). Furthermore, on the images acquired in the coronal orientation the T_1 change cannot only be observed in the lung regions but also in the kidneys and in the spleen, both highly perfused organs. The calculated wash-in and wash-out time constants in the lung parenchyma are larger than the mean values reported by Arnold et al. [186]. In his study, however, a large inter-subject variability of the measured time constants was observed.

Table 5.1. Mean, standard deviation of T_1 and T_2 relaxation times measured using IR-ufSSFP in the lung of healthy volunteers under normoxic and hyperoxic conditions, as well as differences in T_1 and T_2 between the both gas conditions. Volunteer #7 was scanned five times on different days for reproducibility assessment.

		Normoxic condition		Hyperoxic condition		Difference	
Volunteer	**Sex, age**	**T_1 [ms]**	**T_2 [ms]**	**T_1 [ms]**	**T_2 [ms]**	**ΔT_1 [ms] (%)**	**ΔT_2 [ms] (%)**
1	M, 34	1385±83	48±11	1273±80	50±12	112 (8.1)	-2 (-4.2)
2	M, 35	1346±74	56±15	1241±73	55±14	105 (7.8)	1 (1.8)
3	F, 49	1464±84	58±18	1368±91	56±17	96 (6.6)	2 (3.5)
4	F, 31	1428±90	51±19	1301±87	52±23	127 (8.9)	-1 (-2.0)
5	M, 40	1403±79	54±15	1312±62	57±18	91 (6.5)	-3 (-5.6)
6	M, 27	1416±53	57±18	1296±64	56±18	120 (8.5)	1 (1.8)
7, scan 1	M, 29	1351±67	66±20	1244±62	64±22	107 (7.9)	2 (3.0)
7, scan 2	"	1348±75	62±16	1237±65	66±17	111 (8.2)	-4 (-6.5)
7, scan 3	"	1358±71	66±21	1252±72	65±20	106 (7.8)	1 (1.5)
7, scan 4	"	1343±77	64±20	1239±69	64±19	104 (7.7)	0 (0)
7, scan 5	"	1340±81	60±18	1231±79	58±14	109 (8.1)	2 (3.3)

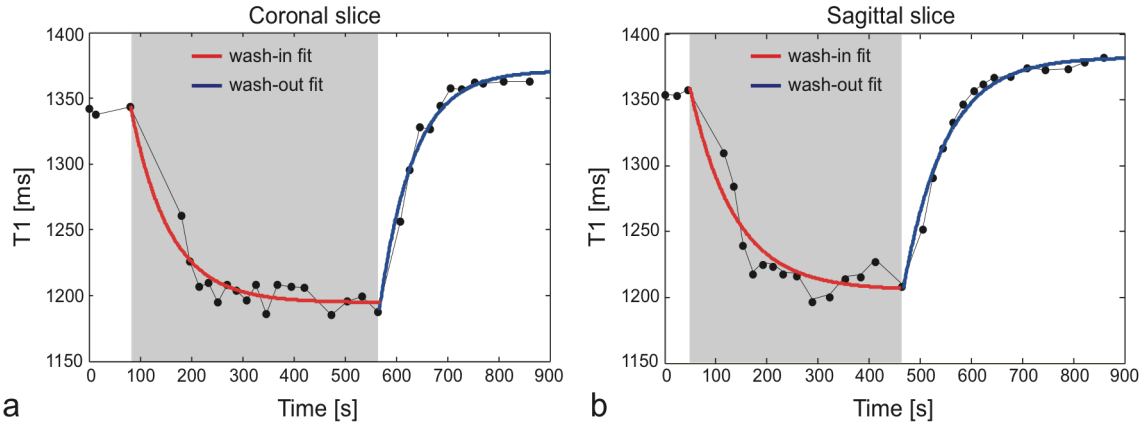

Figure 5.3. Diagrams present the oxygen-dependent change of T_1 in a region-of-interest located in the lung parenchyma measured in two separate acquisitions performed in coronal (a) and sagittal (b) orientation. T_1-related oxygen wash-in and wash-out time constants were calculated using an exponential fit model. The time period where 100% oxygen was delivered is marked as a grey area on the diagram.

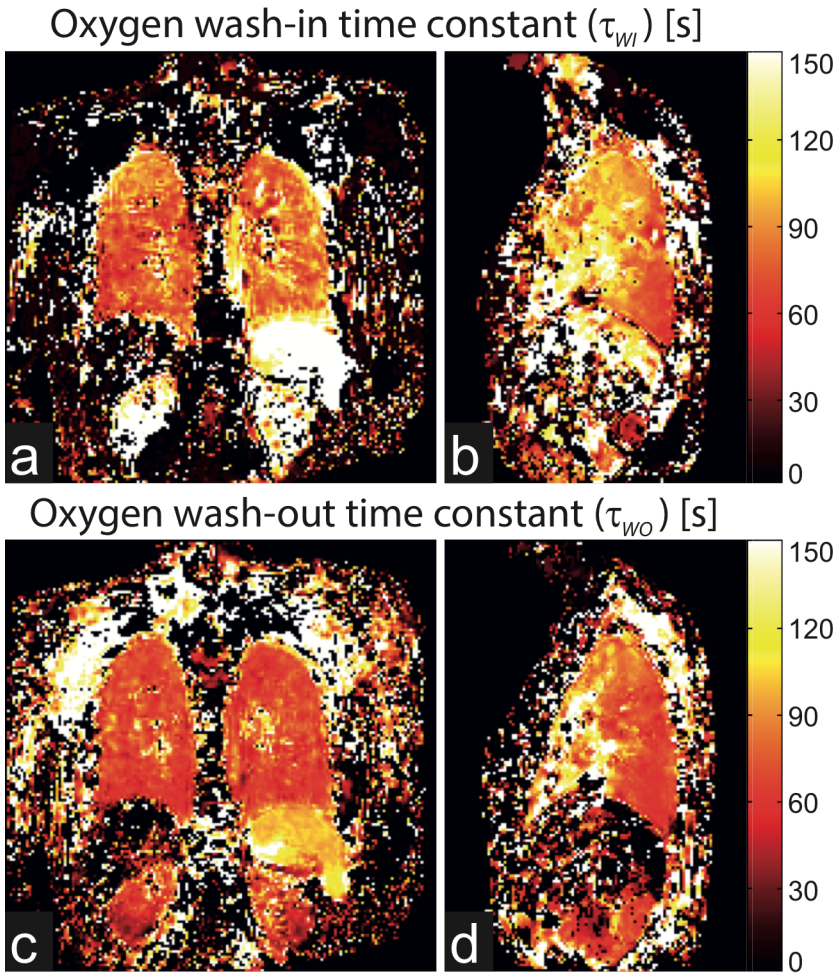

Figure 5.4. T_1 -related oxygen wash-in time constant (τ_{wi}) and wash-out time constant (τ_{wo}) calculated by voxel-wise fitting of an exponential model on a set of registered parameter maps acquired in coronal (a,c) and sagittal (b,d) orientation in Volunteer #7. Oxygen wash-in/wash-out process can be noticed in the lung, spleen and kidneys on the coronal images (a,c). Voxels located outside the body were masked-out.

5.4 Discussion

In this work, we have shown the feasibility of a novel technique for oxygen-dependent pulmonary relaxometry in human subjects at 1.5T. The technique is based on an ECG-triggered acquisition of a series of images using an inversion recovery ultra-fast steady-state free precession pulse sequence adapted for pulmonary imaging by a significant shortening of the TR. As a consequence of the TR reduction the signal-to-noise ratio in the lung parenchyma was improved, which allowed us to produce high quality relaxation time maps at good in-plane resolution of 2.8 mm^2 as for functional lung imaging.

All acquisitions in this study were conducted in expiratory breath-holding and lasted no longer than nine seconds per slice. Hence, it is possible to cover the whole volume of a subject using multiple breath-hold acquisitions, taking no more than a couple of minutes per gas condition. As expected the global T_1 values in the lung measured in all volunteers were reduced during the pulmonary hyperoxia by about 7.8%, and in agreement with expectations from literature [185]. Overall, no significant difference between T_2 values in the lung measured in all volunteers during the steady-state conditions was found.

For the calculation of the relaxation time difference maps a voxel-wise subtraction of estimated values was required. Similarly, a voxel-wise analysis on a series of parameters maps was performed to study the oxygen wash-in and wash-out dynamics. Despite the fact that the volunteers were generally able to reproduce the respiratory volume in expiratory phase, application of non-rigid image registration was mandatory to correct for the misalignments between the lung structures acquired in the normoxic and hyperoxic conditions, or during the dynamic measurements. Due to the relatively thick slices of one centimeter, possible residual through-plane misalignments should marginally affect the results and were neglected.

Dynamic measurements enabled us to observe regional T_1 change during the oxygen wash-in and wash-out phases of the experiment. We used a simple exponential model to extract voxel-wise the T_1-related wash-in and wash-out time constants from the registered T_1 parameter maps. Interestingly, the mean oxygen wash-in time constant was higher than the oxygen wash-out time constant. A similar fact was observed by Arnold et al. [186] using rapid dynamic acquisition of T_1-maps during oxygen enhancement as well as by Chon et al. [187] in a study where a mixture of xenon and oxygen was used as a gas tracer for CT in a large animal experiment. A regional difference in the wash-in/wash-out time constants along the anterior-posterior direction can be noticed on sagittal maps. The dorsal lung regions are characterized by lower τ_{wi} and τ_{wo} values than the ventral parts of the lung. This was also observed during xenon wash-out experiments using SPECT [188]. For both scan series performed in coronal and sagittal orientation the T_1 values measured after oxygen wash-out failed to return to the baseline measured before the administration of 100% O_2. This effect can be caused by an increased pulmonary perfusion due to hyperoxia and might last longer than the oxygen wash-out.

As shown recently by Similarly Zhang et al. [98]) the dynamic T_1 curves could also be converted to the dynamic changes in the partial pressure of oxygen dissolved in the tissue water and plasma of the lung by knowing the O_2 longitudinal relaxivity in water. Similarly, a rate of change of oxygen partial pressure can be estimated using an exponential model.

One of main limitations of the presented technique is the possibility of acquiring only one slice per breath-hold maneuver. Although volumetric ΔT_1 mapping can be performed in clinically feasible scan times of less than 15 minutes, dynamic relaxometry measurements during O_2 wash-in and wash-out phases would require the experiment to be repeated for every acquired slice. One of the possibilities to accelerate this process would be the implementation of multiple-slice acquisition technique [189] and image reconstruction methods taking advantage from the high spatial-temporal redundancy in the acquired datasets [190]. Another limitation was related to the lack of the direct measurement of the oxygen concentration in the gas delivered by the breathing mask and exhaled by the subject. A well-controlled experiment using the proposed MR methodology and additional hardware for on-line measurements of the gas concentration would improve the accuracy of the measurements and provide further insight into the physiology of the lung. Furthermore, our study had an exploratory nature with the main goal to show the feasibility of the proposed relaxometry technique. Hence, the study involved only a small group of healthy subjects.

5.5 Conclusion

We demonstrated the feasibility of steady-state and dynamic oxygen-dependent relaxometry of the human lung at 1.5T. Our method is based on an ECG-triggered IR-ufSSFP pulse sequence adapted for lung imaging and allows for simultaneous and automatic estimation of relaxation time parameter maps. We have employed the method for measurements of T_1 and T_2 measurements in normoxic and hyperoxic conditions in healthy subjects as well as during dynamic measurements of T_1-related oxygen wash-in and wash-out time constants. The potential of the oxygen-dependent pulmonary relaxometry using IR-ufSSFP should be evaluated in further studies on groups of patients with different pulmonary disease.

CHAPTER 6

Signal enhancement ratio imaging of the lung parenchyma with ultra-fast steady-state free precession MRI at 1.5T

A modified version of this chapter has been published as:

Pusterla O*, Sommer G*, Wiese M, Lardinois D, Tamm M, Bremerich J, Santini F, Bauman G, Bieri O. *Signal enhancement ratio imaging of the lung parenchyma with ultra-fast steady-state free precession MRI at 1.5T.* J Magn Reson Imaging, 2018, DOI: 10.1002/jmri.25928.

*Equally contributed to this work.

CHAPTER ABSTRACT

Purpose: To investigate the lung signal enhancement ratio (SER) with ultra-fast steady-state free precession (ufSSFP) after Gd-administration.

Methods: ufSSFP and volume-interpolated breath-hold examinations (VIBE) imaging of the chest was performed at 1.5T before and three minutes after i.v. Gadobenate-Dimeglumine in ten subjects with healthy lungs, and nine patients with pulmonary diseases (COPD, lung cancer, pulmonary fibrosis, lung contusion). A workflow including deformable image registration and median filtering was used to compute 3D SER maps. SER was analyzed in the lung, blood pool, liver, muscles, and fat. In the COPD patients, ufSSFP-SER was compared to ^{99m}Tc-MAA-SPECT/CT by visual scoring of lung enhancement deficits.

Results: In healthy lungs, ufSSFP-SER (99%±23%, mean±pooled intrasubject SD, cv=23%) was significantly higher ($P<10^{-3}$) and more homogeneous ($P<10^{-3}$) than VIBE (47%±26%, cv=57%). ufSSFP-SER was significantly higher ($P<10^{-3}$) for the lungs (99%±9%, mean±intersubject SD) than for the blood (81%±7%) and other tissues (liver 33%±8%, muscle 26%±5%, fat 2%±1%). In the lung ufSSFP-SER exhibits homogeneity on iso-gravitational planes, and an anterior-posterior gradient.
In COPD patients, ufSSFP-SER was reduced and less homogeneous compared to the control group (73%±33%, mean±pooled intrasubject SD, cv=42%). ufSSFP-SER had moderate intermodality agreement with SPECT/CT (Cohen's kappa $\kappa_q = 0.64$).

Conclusion: ufSSFP-SER of the lung is a rapid and simple method. Our preliminary data show plausible results in different pulmonary diseases, motivating further evaluation in larger cohorts.

6.1 Introduction

Pulmonary diseases are an important burden to public health [1, 2]. Functional information on pulmonary perfusion obtained from diagnostic imaging plays a pivotal role for patient management, both in terms of diagnosis and therapy planning [2, 4, 5]. Pulmonary perfusion is commonly assessed by scintigraphy and hybrid single photon emission tomography/computed tomography (SPECT/CT) using ^{99m}Tc-labelled macro-aggregated albumin (MAA) [5]. Alternatively, contrast-enhanced dual-energy CT [191] can be performed, but is not yet fully established in clinical practice. Similarly, magnetic resonance imaging (MRI) has been described as a promising method to assess pulmonary morphology and function [4, 28, 29, 33, 47]. Since MRI comes without an associated radiation burden [29–31], further technical development of pulmonary MRI is of interest particularly for frequently repetitive imaging investigations, where radiation protection is an issue.

Functional information about pulmonary perfusion is commonly assessed by MRI from a heavily T_1-weighted spoiled gradient echo (SPGR) in combination with the intravenous injection of a contrast agent [28]. Using rapid volumetric SPGR imaging during the wash-in, peak-enhancement, and wash-out of the contrast agent, dynamic contrast-enhanced (DCE) MRI enables to measure both blood-volume and flow [192]. Moreover, static contrast-enhanced imaging is conventionally performed with SPGR, such as volume interpolated breath-hold examinations (VIBE) [4, 30]. These contrast-enhanced MRI methods have demonstrated to correlate reasonably well with ^{99m}Tc-MAA-SPECT [193], however, with one important limitation: while ^{99m}Tc-MAA-SPECT represents tracer accumulation in the pulmonary arterioles and capillary bed, i.e., in the pulmonary parenchyma itself [194], gradient echo imaging is mainly sensitive to larger vessels, and suffers from low signal-to-noise ratio (SNR) in the lung parenchyma [195].

In contrast, balanced steady-state free precession (bSSFP) offers the highest SNR per unit of time amongst all MRI sequences [108]. Banding artifacts that typically compromise the image quality of bSSFP in the chest have been recently mitigated by the development of an ultra-fast SSFP imaging approach (ufSSFP) [45]; a variant of bSSFP with ultra-short repetition times, which has already demonstrated potential for morphological and functional assessment of the lungs [47, 144, 157, 196]. Due to their mixed contrast behavior driven by the T_2/T_1 relaxation time ratio [110], bSSFP sequences are frequently regarded as being rather insensitive to gadolinium-based contrast agents, although their potential use after contrast administration has been demonstrated and advised [116, 117]. From the theory [108], the signal enhancement for SSFP after contrast administration is expected to be higher for tissue with long T_1 and short T_2, such as the lung (T_1/T_2 ~ 1375/66 [ms/ms] at 1.5T, cf. [197]), as compared to the blood (T_1/T_2 ~ 1300/300) and fluids with comparable T_1/T_2.

The purpose of our work is to investigate the static signal enhancement ratio (SER) of ufSSFP and VIBE from two sets of volumetric scans, acquired before and after the administration of a gadolinium-based contrast agent.

6.2 Methods

This study was approved by the local institutional review board and all subjects gave written informed consent. Imaging examinations were performed between July 2015 and Dec. 2016.

6.2.1 Study subjects

Pulmonary SER imaging with ufSSFP and VIBE was retrospectively evaluated in 10 consecutive patients (4 males, 6 females; mean age 40±13 years, range 25-64) with healthy lungs who received chest MRI with contrast agent because of a suspected mediastinal mass. For structural and functional examination of the lung, both ufSSFP and VIBE sequences were part of our routine clinical MRI protocol. Mediastinal mass was excluded, through MRI in eight cases. One subject had thymic hyperplasia, another subject had an esophageal duplication cyst. Since no disease of the lung was present, these 10 patients are in the following referred to as the "control group" of the study.

Static ufSSFP-SER imaging was further assessed in nine patients with common pulmonary diseases showing a diversified spectrum of pulmonary pathologies. Seven patients (3 males, 4 females; mean age 64±10 years, range 45-74) were examined as part of an ongoing clinical trial investigating the potential of MRI in chronic obstructive pulmonary disease (COPD). Of these seven COPD patients, three patients had COPD global initiative for chronic obstructive lung disease (GOLD) stage II, one patient GOLD stage III, and three patients GOLD stage IV; three of the COPD patients had evident emphysema and four had non-small-cell lung cancer (NSCLC). In these seven COPD patients, recent ^{99m}Tc-MAA-SPECT/CT exams (delay 21±22 days, interval: 1-51 days) were available for comparison to SER imaging.

Two further patients with a different pulmonary pathology than COPD who were examined with ufSSFP-SER imaging are also included in this study for illustration purposes. The first patient, a 54-year-old female with scleroderma and non-specific interstitial pneumonia (NSIP), received the MRI exam for routine follow-up; in this patient, the morphological MR images were taken for comparison to ufSSFP-SER imaging. The second patient was a 71 years old male with traumatic lung contusion who underwent CT and MRI (interval: 8 days) after a traumatic accident.

6.2.2 MR imaging

All MRI scans were performed on a whole-body 1.5T MR scanner (MAGNETOM Avanto, Siemens Healthineers, Erlangen, Germany) using a 24-channel spine and a 12-channel thorax receive-array centered on the lungs. Both ufSSFP [45] and VIBE scans were acquired before and after intravenous injection of Gadobenate Dimeglumine (MultiHance®, Bracco Imaging S.p.A., Milan, Italy) using the standard dose of 0.2 ml per kg body-weight. In order to avoid the first pass (concentration peak) of the contrast agent, and rather have a static distribution of contrast [198], post-contrast imaging for static SER mapping was performed 3 minutes after the contrast injection: first with ufSSFP, and immediately after (ca. 30 s) with VIBE, resulting in a similar contrast agent concentration for the two imaging modalities [198].

Imaging with both volumetric sequences was performed in inspiratory breath-hold. The sequence parameters were chosen to obtain a high spatial resolution to guarantee good morphological details for the radiological diagnosis (see Heye et al. [47]) and similar acquisition times (~15 seconds). If necessary, the ufSSFP acquisitions could be shortened by the technician to 11 seconds to minimize the respiratory effort. The repetition time (TR) of the ufSSFP sequence was minimal, to avoid banding artifacts; the TR for VIBE was set as recommended elsewhere [199]. The flip angle for ufSSFP and VIBE were set for close-to-maximal lung signal intensity after contrast agent administration, following the theoretical signal-model [163] and as explained elsewhere [117]. Due to radiological image preferences, ufSSFP was acquired with coronal and VIBE with transverse image orientation. Detailed parameters for ufSSFP and VIBE are available in Table 6.1.

6.2.3 SPECT/CT

Lung perfusion SPECT/CT was performed in the seven COPD patients as part of the routine clinical workup using a standard administered dose of 111 MBq ^{99m}Tc-MAA. The scintigraphy and SPECT were acquired on a double-head SPECT/CT scanner (Symbia Intevo 16, Siemens Healthineers, Forchheim, Germany). Three-dimensional ordered subset expectation maximization (OSEM) with 4 subsets, 8 iterations and 4 mm Gaussian filtering was used for reconstruction. The voxel size was isotropic 4.8 mm. The acquisition time for SPECT was 20 min. The CT scans followed a low dose protocol with 130 kV and 30 mAs reference values resulting in a total dose-length product (DLP) of ~100 mGycm. CT-data were reconstructed using filtered back projection with a B70s convolution kernel. The slice thickness was 1.5 mm and the in-plane resolution was 0.7×0.7 mm^2.

Table 6.1. Pulse sequences parameters for ufSSFP and VIBE.

Parameter	ufSSFP	VIBE
TR / TE	1.43 / 0.61 ms	4.0 / 1.05 ms
Flip angle α	35°	10°
Bandwidth	1563 Hz/pixel	580 Hz/pixel
Acquisition plane	Coronal	Transversal
Field of View (FoV)	400×400×280 mm^3	280×400×360 mm^3
Matrix	160×160×112	112×160×112
Resolution	2.5×2.5×2.5 mm^3	2.5×2.5×3 mm^3 [a]
Slice resolution	100%	80%
Phase oversampling	30%	0
Phase partial Fourier	8/8 (6/8) [b]	6/8
Slice partial Fourier	8/8	6/8
GRAPPA factor	2	2
Acquisition time	15 s (11 s) [b]	17 s

[a] Interpolated to 1.25×1.25×3 mm^3.

[b] Acquisition time can be shortened by technicians for patient examination, if necessary.

6.2.4 MR image post-processing

Pre- and post-contrast volumetric datasets were first co-registered to spatially match lung structures, such as vessels and lung boundaries, using a mass preserving three-dimensional deformable B-spline image registration algorithm (Elastix version 4.7, University Medical Center Utrecht, The Netherlands) [145]. Subsequently, the registered datasets were median filtered (kernel radius 9×9×9 mm^3). Median filtering (see Ref. [142] for details), a common edge-preserving noise reduction filter (cf. Figs. 3.1 and 4.2), is particularly effective to remove "salt and pepper" type of noise, that is sparsely occurring white and black pixels, such as the hyperintense vasculature overlying the pulmonary tissue and small airways (up to a size of 9×9×9 mm^3 in our post-processing). Finally, SER images were calculated voxel-wise (at position $\vec{x}$) from the signal intensity before [$SI_{pre}(\vec{x})$] and after [$SI_{post}(\vec{x})$] contrast agent administration, respectively, using

$$SER(\vec{x}) = \frac{SI_{post}(\vec{x}) - SI_{pre}(\vec{x})}{SI_{pre}(\vec{x})} . \qquad (6.1)$$

Image post-processing was identical for ufSSFP and VIBE, and essentially similar to previous

works [157, 196]. Signal preservation by the image registration was analyzed by comparing the whole-lung signal before and after image registration. A schematic summary of the proposed method is shown in the Figure 6.1.

Figure 6.1. Schematic of the post-processing for signal enhancement ratio (SER) imaging. Pre-contrast (Vol1) and post-contrast (Vol2) volumetric datasets are first registered (a) to match the lung structures (e.g., diaphragm positions and vessels). Successively, the datasets are median filtered (b) to remove vasculature and to get access to the parenchymal signal. (c) Pulmonary SER-maps are finally calculated (see "Method" Section 6.2.4).

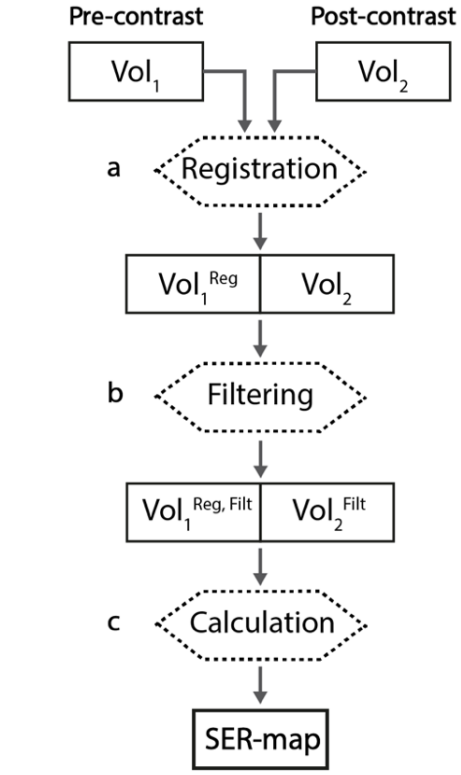

6.2.5 Visual and quantitative data analysis

To analyze the difference between VIBE and ufSSFP-SER imaging, five volumetric regions of interest (ROI) were manually segmented in every subject comprising the whole lung (excluding large vessels), the aortic-arch blood pool, the whole liver (excluding large vessels), muscles (subscapularis, pectoralis), and subcutaneous thoracic fat. Figure 6.2 shows an exemplary segmentation of these ROIs. For every ROI and every individual, the mean value and standard deviation (SD) of the SER were computed. From these, the group mean, the intersubject SD (interindividual deviation from the group mean) and pooled intrasubject SD (square root of the average variance) were calculated. The coefficient of variation (ratio of pooled intrasubject SD

and group mean) was also calculated for the lung ROI. Statistical significances were determined using Wilcoxon signed-rank paired test.

The robustness (artifact behavior) of SER imaging was assessed in the control cohort by a board certified radiologist and nuclear medicine physician (G.S., 9 years of clinical experience). The radiologist scored on the SER images, for every lung lobe, the percentage of volume affected by artifacts (score 0, no artifacts; score 1, 1-25% of lobe volume; score 2, 26-50%; score 3, 51-75 %; and score 4, 76-100%). Statistical significance between ufSSFP-SER and VIBE-SER artifact scoring was determined using Wilcoxon signed-rank paired test.

For the COPD patients, ufSSFP-SER of the lung was compared to ^{99m}Tc-MAA-SPECT/CT. To this end, a radiologist and nuclear medicine physician (G.S.) visually scored on SPECT/CT, for every lung lobe, the extent of visible perfusion deficits as percentage of the lobar volume (score 0, no defects; score 1, 1-25% of lobe volume affected; score 2, 26-50%; score 3, 51-75%; score 4, 76-100%). The same scoring was performed for the ufSSFP-SER images by a second board certified radiologist (J.B., 20 years of clinical experience). Intermodality agreement was calculated by Cohen's kappa coefficient using both linear and quadratic weighting (κ_l and κ_q, respectively) [200, 201].
For the NSIP and the trauma patients, ufSSFP-SER images were visually correlated with morphological MR and / or CT by a radiologist (G.S.).

Image post-processing and statistical analysis were performed with Matlab (Mathworks, Natick, MA, USA) by three physicists experienced in medical imaging (O.P., G.B. and F.S., with 3, 9 and 11 years of experience).

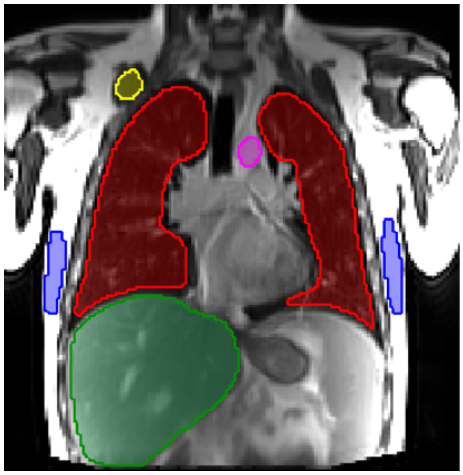

Figure 6.2. Exemplary ufSSFP coronal view indicating representative volumetric region of interests of the lung (depicted in red, volume = 2716 cm^3), aortic arch (pink, 21 cm^3), liver (green, 1322 cm^3), muscle (yellow, 174 cm^3) and fat (blue, 125 cm^3).

6.3 Results

6.3.1 Signal enhancement in the control group

In all subjects, ufSSFP and VIBE scans provided diagnostic image quality and allowed the derivation of static, volumetric, SER images. Imaging was performed in inspiratory breath-holding and thus in similar breathing phases. As a result, image registration was successful in all cases. Lung signal intensity was not affected by the registration, deviating by -2.7% to 2.9% (min, max) for ufSSFP (mean±SD = 0.8%±1.9%), and by -5.4% to 6.2% (0.3%±4.3%) for VIBE. No patient was excluded from the analysis.

A side-by-side comparison of ufSSFP and VIBE pre- and post-contrast images (maximum intensity projection) is presented in Figure 6.3 for a representative subject from the control cohort (no lung disease). As compared to non-enhanced imaging (Figs. 6.3a and c), after contrast administration both VIBE and ufSSFP show a clear signal increase in the lung parenchyma and vasculature (Figs. 6.3b and d), also yielding enhanced morphological details. In both pre- and post-contrast imaging with ufSSFP the signal of fine vessels and parenchyma is clearly caught until the very periphery of the lung (Figs. 6.3a and b); especially when compared to the dark background signal of the trachea. In contrast, with VIBE almost similar signals are registered in the lung periphery and trachea.

Figure 6.4 shows, for a subject of the healthy cohort, native ufSSFP and VIBE images pre- and post-contrast together with the resulting static SER images. The efficacy of median filtering on the same data is exemplary shown in Figure 6.5. In this subject (Fig. 6.4), the average lung SER using ufSSFP (Fig. 6.4c) was 96%±23% (mean±SD), appearing homogeneous on iso-gravitational planes (e.g., 95%±13% on the presented coronal slice in Fig. 6.4c), but revealing an increase from non-dependent (ventral, e.g., 83%±19%) to dependent areas (dorsal, e.g., 114%±19), as expected in a healthy lung. In contrast, VIBE-based SER images of the same subject (Fig. 6.4f) appear highly inhomogeneous with a considerably lower mean whole lung SER of 41%±28%. Similar results are found for all the subjects of the control group (three of them exemplarily shown in Fig. 6.6).

For the ten subjects of the control cohort, group-averaged SER values are outlined in Table 6.2 for different anatomical regions. For ufSSFP, the SER values were significantly higher in the lung parenchyma (99%±9%, mean±intersubject SD) than in the blood pool (81%±7%, $P<10^{-3}$) and in other tissues (liver 33%±8%, muscle 26%±5%, fat 2%±1%). As a consequence, ufSSFP-SER images reveal an improved depiction of the lung parenchyma (cf. Fig. 6.4c). In contrast, VIBE-based SER

of the lung was significantly lower ($P<10^{-3}$) and more inhomogeneous (mean = 47%, pooled intrasubject SD = 27%, cv = 57%, $P<10^{-3}$), as compared to ufSSFP-SER (mean = 99%, pooled intrasubject SD = 23%, cv = 23%). In the blood pool, however, VIBE-SER (164%±17%, mean±intersubject SD, $P<10^{-3}$) was twice as high (ufSSFP-SER, 81%±7%).

A schematic of the artifacts perceived on ufSSFP-SER and on VIBE-SER images is presented in Table 6.3. Generally, for the control group, ufSSFP-SER images were broadly homogeneous, revealing only limited image artifacts. Overall, for ufSSFP, none of the SER images had an artifact scoring above 2 (artifact size <50% for every lung lobe). The left lower lobe of the lung was the region most prone to artifacts caused to heart beating and partial volume effects (see e.g., Fig. 6.4c). In contrast, VIBE-SER of the lung is generally prone to artifacts and signal variations, even in the absence of parenchymal abnormalities. The average score of the artifacts per lobe was 2.3±0.6 for VIBE-SER, and 0.6±0.4 for ufSSFP-SER. The artifact scoring for ufSSFP-SER was significantly lower than for VIBE-SER ($P<10^{-12}$).

Overall, for the purpose of pulmonary SER imaging, ufSSFP outperformed VIBE, providing an accentuated signal enhancement and visually homogeneous SER images (mean = 99%, pooled intrasubject SD = 23%, cv = 23%) with a reduced intersubject standard deviation among the collective of subjects with healthy lung (mean = 99%, intersubject SD = 9%). As a result, only the static signal enhancement, as observed with ufSSFP, was investigated for SER imaging in patients. with pulmonary disease.

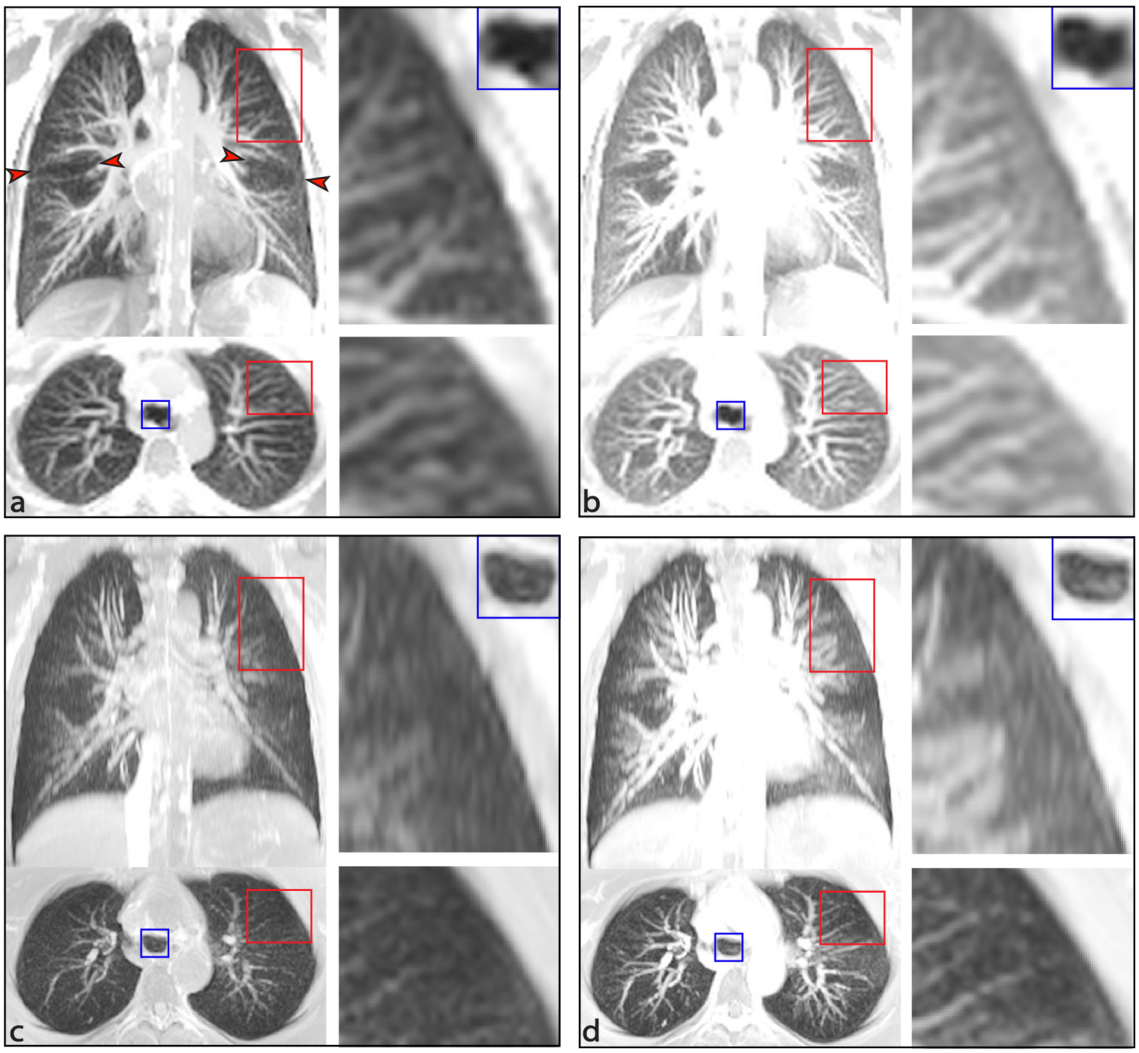

Figure 6.3. Maximum intensity projection (effective slice thickness 25 mm) of ufSSFP (a, b) and VIBE (c, d) before (a, c) and after contrast agent injection (b, d) in a 26-year-old male subject from the control group. The red rectangles indicate regions of interests in the lungs, "zoomed" on the right of the figures; in blue is marked the trachea, "zoomed" on the top-right of the figures. For visual comparison of the signal increase after contrast administration, the same windowing (logarithmic grey-scale) is used for pre- and post-contrast images [(a, b) and (c, d)]. Both sequences allow for the depiction of the pulmonary vasculature. The red arrowheads (a) indicate exemplarily the fissure between the lung lobes [observable in all images a-d].

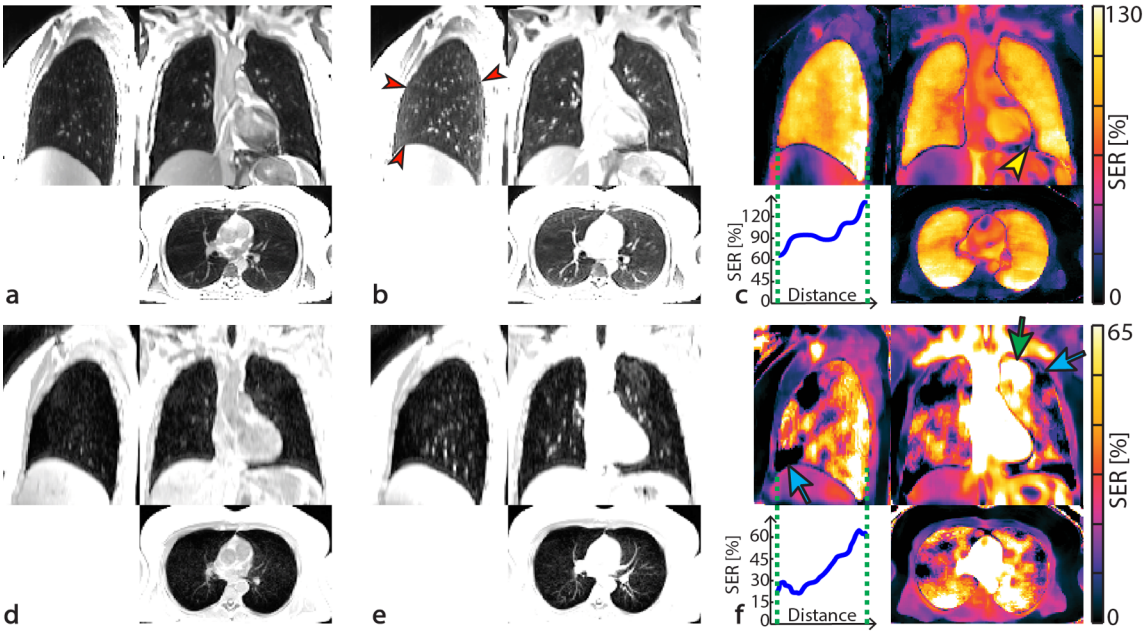

Figure 6.4. Comparison of ufSSFP (a-c) and VIBE (d-f) for a representative subject from the control group (female, 54 years old). Native (non-registered) pre-contrast (a, d) and post-contrast datasets (b, e) are co-registered and median-filtered to calculate signal enhancement ratio maps (c, f). The same windowing (grey-scale) is used for pre- and post-contrast images [(a, b) and (d, e)] for visual comparison of the signal increase after i.v. contrast administration. SER images with ufSSFP appear homogeneous in the lung [(c), SER = 96%±23%, cv = 24%], whereas VIBE-based SER images show patchy hyper- and hypo-intense artifacts (e.g., green and blue arrows) [(f), SER = 41%±28%, cv = 86%]. SER values in the lung increase from ventral to dorsal, as depicted in the plots [see left-lower panel in (c, f)] which report the mean SER in the iso-gravitational planes as a function of the ventral-to-dorsal distance. Balanced SSFP "banding" artifacts are entirely mitigated by the accelerated ufSSFP acquisition scheme (a, b). Different scaling was used for ufSSFP-SER and VIBE-SER images in (c, f); in (c), the yellow arrowhead shows exemplarily an artifact caused by heart pulsation. In both VIBE and ufSSFP images the fissures between the lung lobes are observable [e.g., sagittal view in (b), marked by red arrowheads].

Table 6.2. Comparison of the observed signal enhancement ratio (SER) for ufSSFP and VIBE for different anatomical regions and averaged over ten subjects from the control group (healthy lung).

	SER, mean ± intersubject SD (pooled intrasubject SD) [%]				
	Lung	Aorta	Liver	Muscle	Fat
ufSSFP	99 ± 9 (23)	81 ± 7 (8)	33 ± 8 (12)	26 ± 5 (6)	2 ± 1 (4)
VIBE	47 ± 12 (27)	164 ± 17 (21)	36 ± 8 (5)	22 ± 3 (5)	7 ± 4 (3)

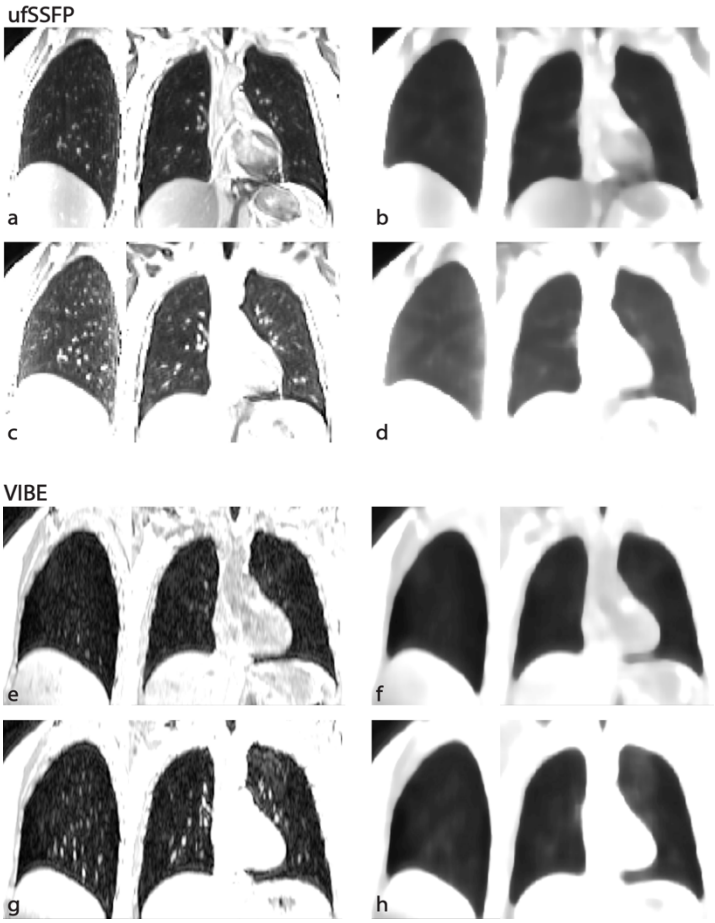

Figure 6.5. Ultra-fast SSFP (a-d) and VIBE (e-h) native images (a, c, e, g) and median filtered (b, d, f, h) before (a, b, e, f) and after contrast agent injection (c, d, g, h) in a 54-year-old female subject from the control group. Median filtering removes vasculature, small airways and noise to recover the underlying smooth parenchymal-background signal variation. The same windowing (greyscale) was used in (a-d) and (e-h).

Table 6.3. Artifact evaluation (e.g., pulsation, heart-beating, partial volume effects) per lung lobe for ufSSFP-SER and VIBE-SER in ten subjects from the control group. "No artifact" is scored 0; score 1 indicates that 1-25% of the lobe volume is affected by artifacts; score 2, 26-50%; score 3, 51-75 %; and score 4, 76-100%. No scores above 2 were found for ufSSFP; artifacts in the lower lobes and the lingula are attributable to cardiac pulsation. Average score of the artifacts: 2.3±0.6 for VIBE-SER and 0.6±0.4 for ufSSFP-SER.

Image artifacts for ufSSFP-SER and VIBE-SER divided by lung lobe (n = 10 subjects).

ufSSFP-SER

	RU	RM	RL	LU	Lin	LL
No artifacts	10	7	6	9	4	–
Score 1	–	1	4	1	4	5
Score 2	–	2	–	–	2	5
Score 3	–	–	–	–	–	–
Score 4	–	–	–	–	–	–

VIBE-SER

	RU	RM	RL	LU	Lin	LL
No artifacts	–	1	–	–	2	–
Score 1	–	–	2	–	1	2
Score 2	2	7	6	3	5	5
Score 3	5	1	2	6	2	3
Score 4	3	1	–	1	–	–

Abbreviations: RU = right-upper lobe; RM = right-middle; RL = right-lower; LU = left-upper; Lin = lingula; LL = left-lower.

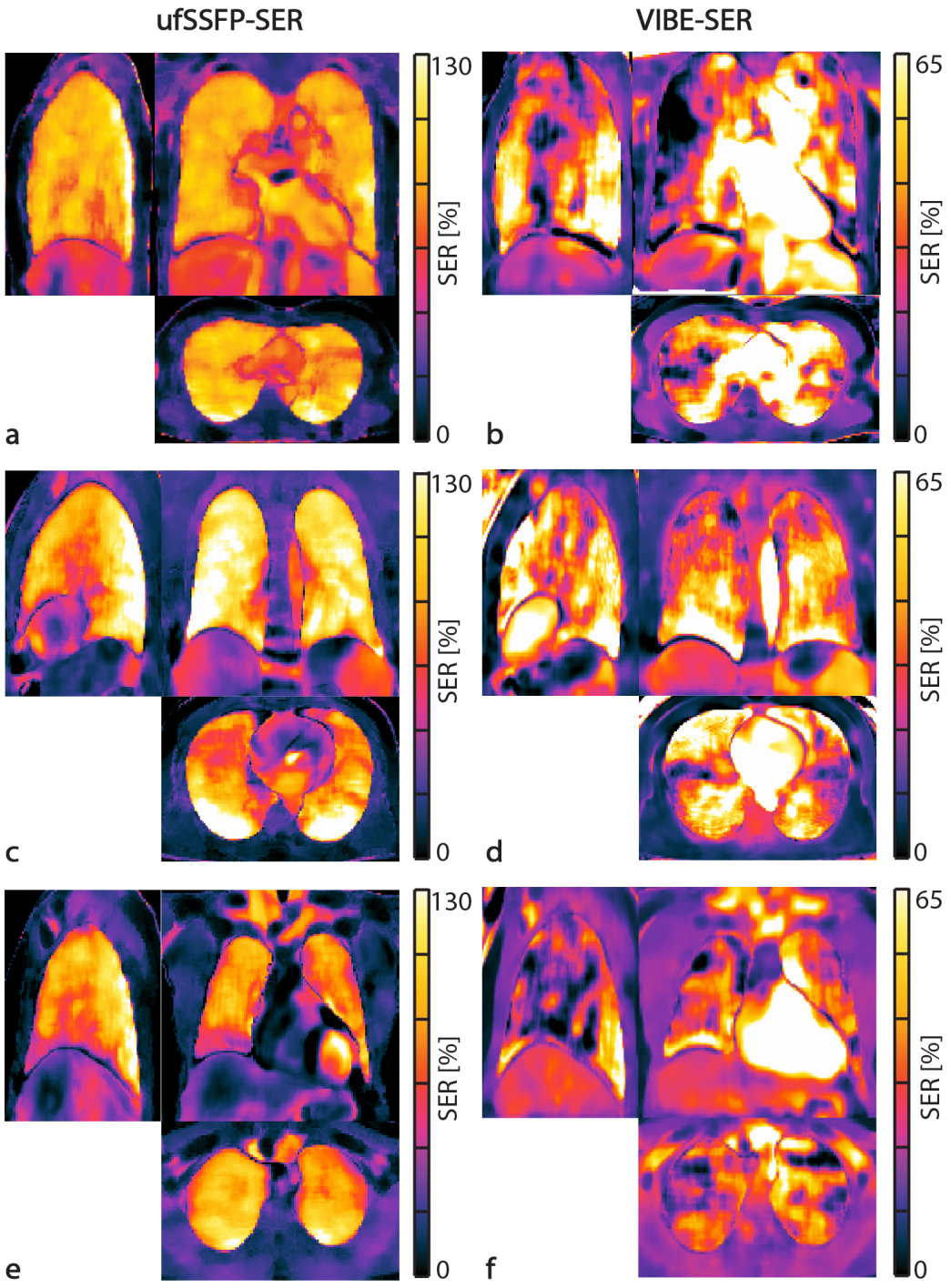

Figure 6.6. Side-by-side comparison of signal enhancement ratio imaging with ufSSFP (a, c, e) and VIBE (b, d, f) in three subjects with no lung disease from the control group [(a, b) female 52 years old, (c, d) male 28 years old, and (e, f) male 43 years old]. To note, the color maps for ufSSFP and VIBE SER are differently scaled. The SER in the lung is more homogeneous using ufSSFP than using VIBE (cf. Table 6.2). Whole lung mean SER values were 97%±20% [(a), mean±SD], 116%±27% (c), 101%±25% (e) for ufSSFP; 55%±24% (b), 61%±31% (d), and 55%±27% (f) for VIBE. To note, in the region of the heart, due to pulsation (and thus partial-volume effects in the native images) the SER values have large signal variations [cf. sagittal view in (c)].

6.3.2 Signal enhancement in pathologic lung tissue

The radiological potential of ufSSFP-SER imaging of the lung was evaluated in patients with pulmonary diseases including COPD, lung cancer, pulmonary fibrosis, and traumatic lung contusion. Imaging with ufSSFP was successful for all patients, who could perform the 15s long breath-holding maneuvers.

Side-by-side comparisons of morphological ufSSFP, ufSSFP-SER, and SPECT/CT imaging for three representative COPD patients are shown in Figure 6.7, Figure 6.8 and Figure 6.9 (COPD GOLD II, COPD GOLD IV, and COPD GOLD III with lung cancer, respectively). In contrast to ufSSFP-SER of the control group (SER = 99%±23%, mean ± pooled intrasubject SD), ufSSFP-SER of the lung in the seven COPD patients was characterized by an overall significantly ($P<10^{-3}$) lower signal enhancement and significantly ($P<10^{-3}$) larger inhomogeneities (SER = 73%±33%, mean ± pooled intrasubject SD, cv = 42%, intersubject SD = 15%). Visually, there was a moderate to strong spatial correspondence between areas of low SER and regions with low radiotracer uptake on ^{99m}Tc-MAA-SPECT (see Figs. 6.7, 6.8, and 6.9). Interestingly, in the patient with NSCLC (Figure 6.9) the SER in the tumor (43%±8%) was lower than in the lung parenchyma (68%±24%).

A comparison of the functional defects, assessed for the COPD patients, with ufSSFP-based SER imaging and with SPECT/CT is shown in Figure 6.10. The lobar scoring for the two imaging modalities shows that SER imaging tends to underestimate the size of defects in COPD compared to SPECT/CT (the mean score of defects in our cohort was 2.0±0.9% for ufSSFP-SER, and 2.5±1.0% for SPECT); Cohen's kappa coefficients indicate moderate intermodality agreement between SPECT/CT and ufSSFP-SER ($\kappa_l = 0.41$, $\kappa_q = 0.64$, fair agreement).

The clinical potential of ufSSFP-based SER imaging is further illustrated in a NSIP and a trauma patient in Figures 6.11 and 6.12. In the patient with NSIP (Fig. 6.11), the fibrotic lung regions visible on the morphological MR images exhibit a streaky decrease in SER (67%±25%) as compared to the healthy parenchyma (99%±22%; whole lung SER = 96%±23%). In the trauma patient (Fig. 6.12), a hematoma is visible inside the lung parenchyma on CT and post-contrast ufSSFP images; the lesion is also well observable on ufSSFP-based SER maps, and reveals a strongly reduced SER (34%±23%) as compared to the healthy lung (110%±27%).

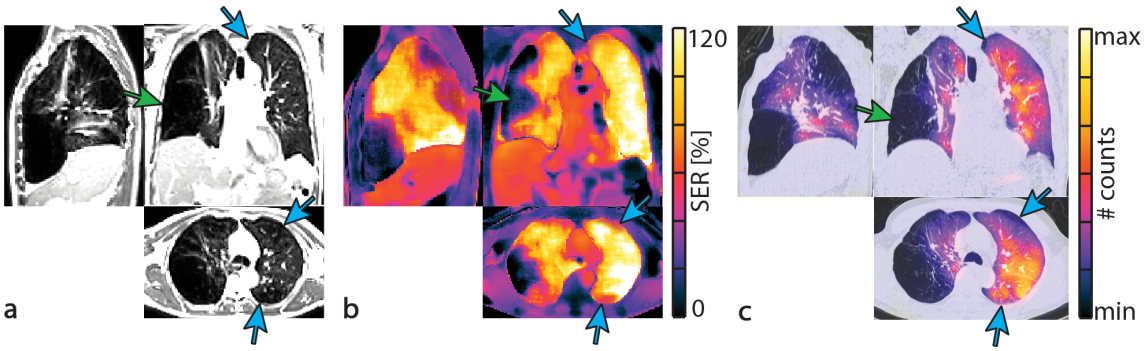

Figure 6.7. Side-by-side comparison of post-contrast ufSSFP (a), ufSSFP-SER (b), and ^{99m}Tc-MAA SPECT/CT fusion images (c) in a 61-year-old male patient with COPD GOLD II and emphysema. There is an extensive destruction of the right lung of this patient by emphysema with large confluent bullae (green arrows). Reduced SER is also seen in the emphysematous regions in the left lung (blue arrows) with apical predominance. Spatial coincidence is observed between areas of low SER in ufSSFP and areas of low radiotracer uptake in ^{99m}Tc-MAA SPECT. The whole lung SER was 75%±42% (mean±SD).

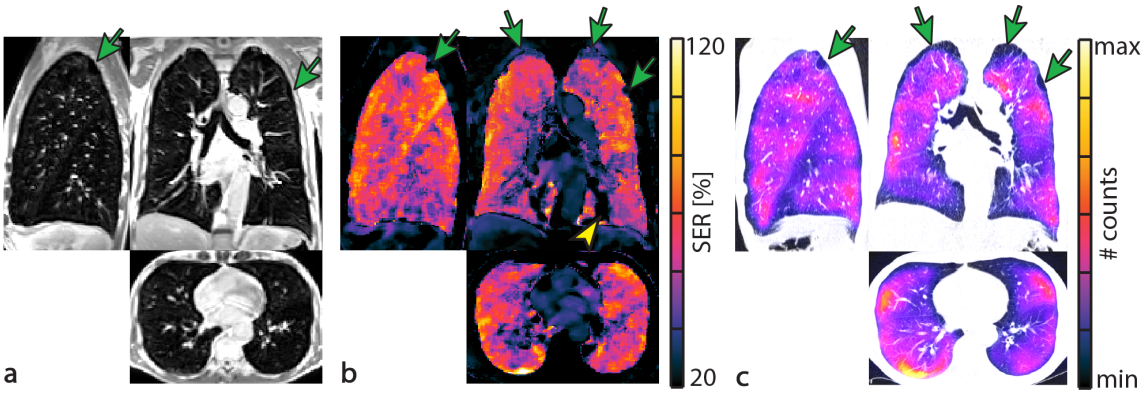

Figure 6.8. Comparison of post-contrast ufSSFP (a), ufSSFP-SER (b), and ^{99m}Tc-MAA SPECT/CT fusion images (c) in a 70-year-old male patient with COPD GOLD IV. In this patient, a more uniform distribution of emphysema compared to the patients presented in Figure 6.7 and Figure 6.9 was observed. A homogenous but still patchy decrease in SER is noted (whole lung SER = 57%±28%, mean±SD). Again there is a good visual agreement between ufSSFP-SER imaging and SPECT/CT, e.g., in the regions of bullous emphysema in the apices (green arrows). In (b), a pulsation artifact from the heart is indicated by the yellow arrowhead.

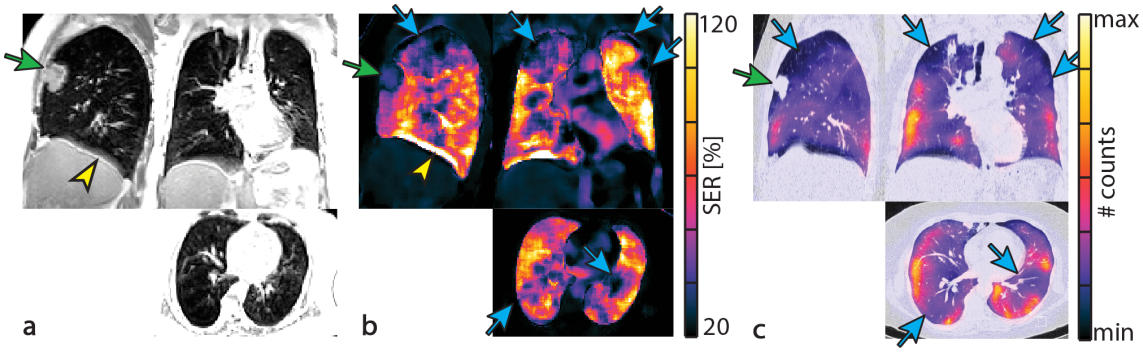

Figure 6.9. Comparison of post-contrast ufSSFP (a), ufSSFP-SER (b), and ^{99m}Tc-MAA SPECT/CT fusion images (c) in a 57-year-old female patient with COPD GOLD III and an NSCLC in the right upper lobe (green arrows). There is extensive inhomogeneity of SER in the lung parenchyma of this patient due to COPD (exemplary impairments depicted by blue arrows) with spatial coincidence of the defects observed with ufSSFP-SER and ^{99m}Tc-MAA-SPECT. The whole lung SER was 68%±24% (mean±SD). To note, the solid tumor in the right upper lobe of this patient shows lower SER than the surrounding lung parenchyma (43%±8%). In (b), the SER scale was optimized to facilitate visualizations of functional impairments. The yellow arrowheads in (a, b) indicate a blurring artifact, caused by a minute diaphragm movement due to non-perfect breath-holding during imaging.

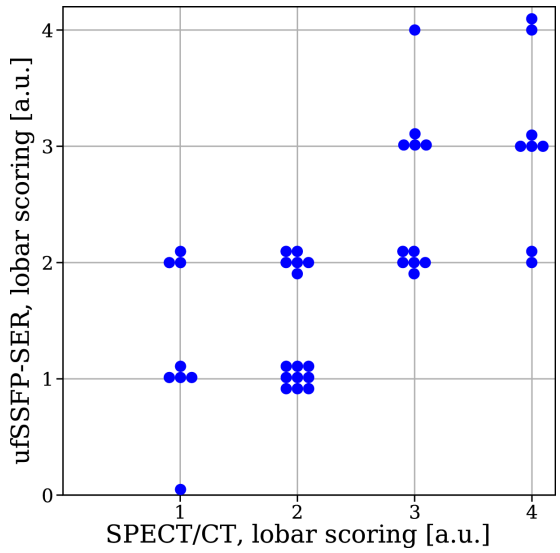

Figure 6.10. Functional defects per lung lobe in seven COPD patients evaluated with ufSSFP-SER and with ^{99m}Tc-MAA SPECT/CT. Score 0 indicates no defects; score 1, 1-25% of lobe volume is affected; score 2, 26-50%; score 3, 51-75%; score 4, 76-100%. The lobar scoring for the two imaging modalities differed up to 2 units and showed moderate intermodality agreement with SPECT/CT (Cohen's kappa $\kappa_l = 0.41$, $\kappa_q = 0.64$).

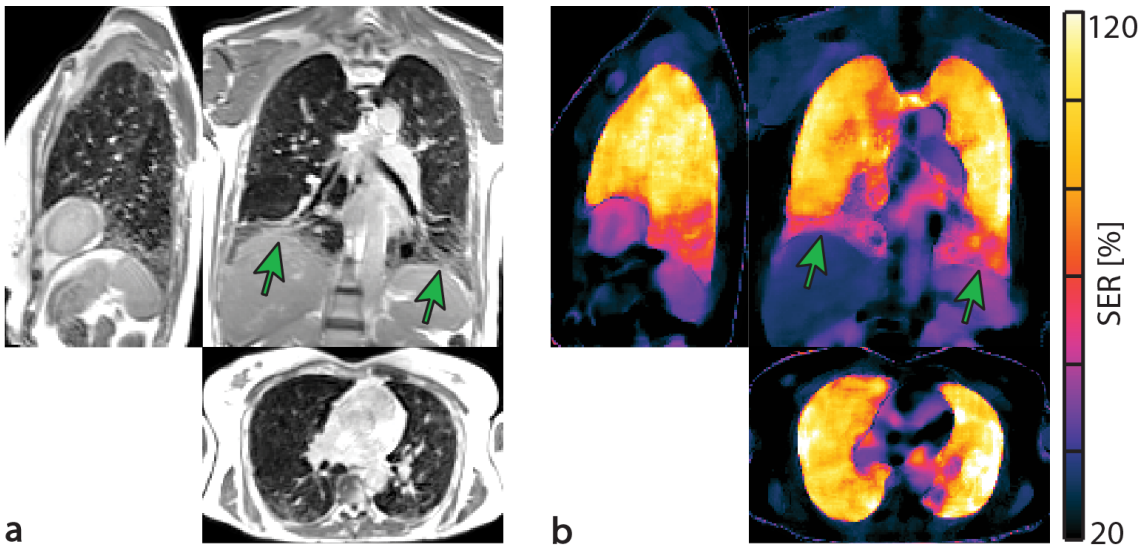

Figure 6.11. Post-contrast ufSSFP images (a), and ufSSFP-SER images (b) in a 58-year-old female patient with scleroderma and NSIP. A streaky decrease in SER is noted in both lower lobes corresponding to fibrotic changes seen on morphological MRI (green arrows).

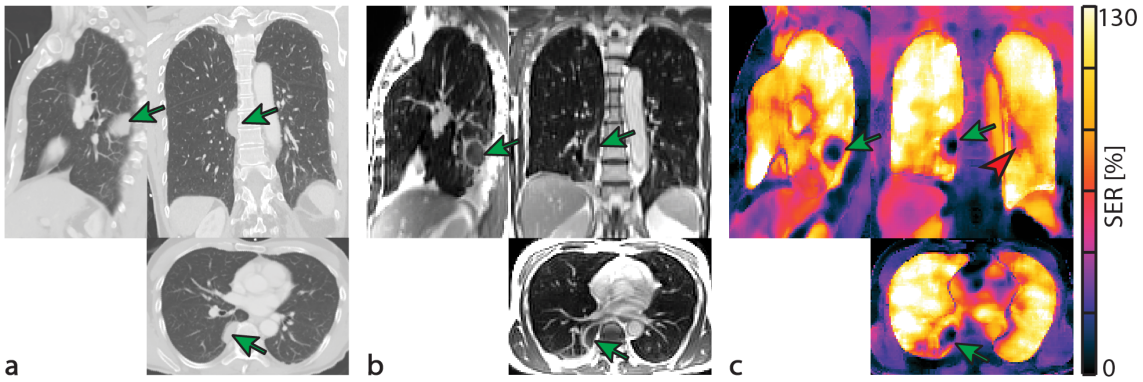

Figure 6.12. CT (a), post-contrast ufSSFP (b), and ufSSFP-SER images (c) in a 71-year-old male patient after traumatic lung injury. The green arrow indicates a subpleural hematoma in the lung parenchyma of the right lower lobe. In the SER images (c), in comparison to the normal lung (SER = 110%±27%, mean±SD) the hematoma shows a reduced enhancement (SER = 34%±23%, mean±SD). The red arrowhead on the SER map (coronal view) indicates an artifact caused by pulsation.

6.4 Discussion

From the shortened TR, as compared to contemporary bSSFP methods [108], ufSSFP [45] offers banding-free chest imaging at 1.5T and has shown promising result for morphological and functional investigations [33, 45, 47, 144, 157, 196, 197]. In this work, we have extended the prospects of ufSSFP imaging to the diagnosis of functional abnormalities of the pulmonary parenchyma in combination with the administration of an intravenous contrast agent. In contrast to the common consensus that bSSFP sequences are insensitive to contrast agents [108], the ufSSFP signal can be notably increased. In fact, in the post-contrast ufSSFP images, the signal of lung tissue doubles, revealing the highest increase amongst all captured organs and the blood pool.

It might be interesting to note that the signal of coherent SSFP, such as balanced SSFP (and thus ufSSFP), scales with T_1/T_2 [45, 108, 163], whereas the signal of incoherent SSFP, such as VIBE, is predominantly weighted by T_1. From this, especially in the limit of large T_1/T_2 as for the lung (T_1/T_2 ~ 1375/66 [ms], cf. [197]), a similar signal enhancement would be expected for both methods. Overall, ufSSFP, however, revealed to be markedly superior to VIBE. This is most likely caused by the low SNR of VIBE for lung tissue, as a result of the rather long echo time (TE) for DCE-MRI not being adapted to the short T_2^* of the lung. As a result, VIBE acquisitions with considerably shortened TE, or alternatively ultra-short echo time sequences [42, 43], might lead to an improvement for lung SER imaging; especially at higher field strength where susceptibilities effects still limit the applicability of ufSSFP [144].

Overall, ufSSFP-SER images provide a highlighted throughout depiction of the lung parenchyma. This is in contrast to SER images derived from VIBE that were flawed even in the control cohort of subjects with no pulmonary disease by prominent signal variations in the absence of parenchymal abnormalities. Moreover, ufSSFP-SER images of healthy lung tissue appeared isogravitationally homogeneous, but with a prominent gravitational-related gradient increasing the signal from ventral to dorsal lung, in accordance with literature [66, 136, 202]. In the COPD patients, ufSSFP-SER images were characterized by marked inhomogeneities, that coincided with the functional defects seen on ^{99m}Tc-MAA-SPECT (moderate intermodality agreement κ). In the NSIP patient, a decrease in SER values was noted for the fibrotic regions of the lung, corresponding well to morphological MR. Similarly, in the trauma patient, the SER images were sensitive in detecting a lung hematoma.

We observed a moderate intermodality agreement between SPECT/CT and static ufSSFP-SER in the lobe-by-lobe evaluation of the COPD patients. This result may be affected by the fact that

the methods of image acquisition for SPECT, in free breathing, and for ufSSFP, in breath-hold, differ substantially. Furthermore, while SPECT/CT is known to reflect ^{99m}Tc-MAA lodged in the capillaries (and not in the extravascular parenchyma) thanks to arterial perfusion, the exact anatomic and physiological origin of the signal enhancement observed in the lung with ufSSFP is unknown. From our preliminary data, we hypothesize that this effect is primarily related to the smaller vasculature of both the arterial and venous side of the capillary beds and may additionally include also parenchymal tissue contrast as a sort of "delayed enhancement". The final answer to this question, however, cannot be given by this feasibility study and requires further investigation.

While the obtained results with ufSSFP-SER imaging in patients appear promising, we acknowledge that the administration of contrast agent might not be indicated for some categories of subjects (e.g., in case of renal failure or allergy). Furthermore, the current approach requires short breath-holding maneuvers, which sometimes may not be feasible (e.g., in infants), but might be overcome by using self-navigated free-breathing methods [156]. Similarly, residual motion artifacts spotted on SER images can, in principle, be addressed with cardiac-triggered acquisitions, but only at the cost of scanning efficiency.

It may be perceived as a limitation of the present study that the signal enhancement of ufSSFP was not investigated dynamically at several time-points after contrast agent injection, as performed with traditional DCE-MRI. Resolving dynamic contrast enhancement with ufSSFP requires an adaptation of the sequence, e.g., using view-sharing methods [203]. This will be subject of future investigation. Another focus of ongoing development will be attempting to suitably standardize the measurement (e.g., hardware, parameters, post processing, reproducibility). In this context quantitative SER imaging might automatically identify lung defects lobe-by-lobe, for instance by using algorithms involving adaptive k-means thresholding [204] of the SER signal-distributions, and segmentation pipelines as presented by Tustison et al. [154] or using machine learning.

Another limitation of our work is that the group of patients with pulmonary pathology is small. Hence, our study only demonstrates the technical feasibility of pulmonary ufSSFP-SER imaging in some of the most common pulmonary disease conditions associated with respiratory discomfort (eight of the included patients, except the trauma patient, had impaired pulmonary function with an FEV1 of 20%-75% of normal). We cannot yet provide any validation of ufSSFP-SER imaging in terms of its diagnostic role for specific diseases. To this end, further prospective investigation of the method in a larger collective of subjects and against standard functional imaging methods, such as DCE-MRI with high temporal resolution and SPECT/CT, is required.

6.5 Conclusion

Following intravenous injection of gadolinium-based contrast agents the signal of ufSSFP is increased in the lung parenchyma. In combination with a pre-contrast native acquisition and specific post-processing, ufSSFP-based SER imaging offers an improved depiction of the pulmonary parenchyma. Preliminary findings in patients show plausible patterns of signal distribution for different pulmonary diseases. Added as a complement to common contrast-enhanced MRI protocols (e.g., DCE-MRI), ufSSFP-SER imaging may thus provide helpful complementary information about the functional abnormalities of the lung parenchyma from only two rapid breath-hold scans. Its clinical benefit, particularly in comparison to ^{99m}Tc-MAA-SPECT/CT and DCE-MRI, remains to be further investigated.

CHAPTER 7

Summary and outlook

7.1 Summary

Within the scope of this thesis, a variety of methods for improved pulmonary functional imaging using ufSSFP acquisition schemes have been developed. These techniques have been evaluated in proof-of-principle studies; in healthy subjects and patients with different pulmonary diseases. The most important results are discussed here in detail; accentuating the potential and limitations, as well as advantages and disadvantages of every method.

Chapter 2. For FD-MRI, from the shortened TR, ufSSFP yielded considerable signal increase compared to conventional bSSFP. Furthermore, the proposed protocol demonstrated mitigation of artifacts related to pulsation and off-resonance, resulting in a general improved image quality. At 1.5 Tesla, FD-MRI has reliably provided perfusion- and ventilation-related maps in healthy volunteers, strengthening the potential of this method to add diagnostic information for clinical imaging. In contrast, at 3 Tesla, residual off-resonance bandings arising from increased susceptibility effects were observed to affect the quality of the acquired images. The drawback of FD-MRI is its limitation to 2D acquisitions and as a consequence the out-of-plane organ motion might reduce the quality of the functional maps.

Along with an ameliorated algorithm to separate the signal modulations given by heart pulsation and lung ventilation, denoted Matrix Pencil (MP) decomposition [104], FD-MRI has recently shown clinical potential [33] for quantifying the ventilation and perfusion impairments in children with cystic fibrosis. FD-MRI is of special benefit for the longitudinal monitoring of young patients since it is feasible with simple free-breathing acquisitions, without contrast agent administration, and it does not require any ionizing radiation.

Chapter 3. Rapid 3D α-mapping has shown to provide quantitative information about lung ventilation with an isotropic resolution, suited for clinical diagnostic. As expected from the exploited lung model and the resulting insensitivity of the parameter α to the lung breathing phases and lung density, α-mapping showed good reproducibility in healthy volunteers. In patients with pulmonary diseases (CF and COPD), the functional impairments observed on α-maps proved to be directly associated to the defects present on FD-MRI, DCE-MRI, and CT. Furthermore, in the **Addendum to Chapter 3**, it was observed that α-mapping is feasible in children with CF (6-17 years old) and that the percentage of respiratory impairments quantified with α-mapping are strongly correlated with the lung clearing index (LCI), a nitrogen multiple-breath washout outcome parameter describing whole-lung ventilation inhomogeneity [118].

Requiring only 5 breath-hold acquisitions, α-mapping offers quantitative 3D ventilation imaging

with scan times of only 2-3 min. Nevertheless, the clinical applicability of α-mapping is hampered by the need for manual lung segmentation, which is used to retrieve the lung volume and thus required to calculate α. This limitation could possibly be eliminated by developing dedicated automatic segmentation algorithms, e.g., based on neural networks (deep learning), as currently being investigated [205].

The proposed approach for α-mapping requires short breath-holding manoeuvres (10-15 seconds), which may not always be feasible for all patients. Furthermore, in this work, α-maps were calculated from 5 volumetric datasets acquired at different lung inspiratory breath-hold levels (capacity). However, the calculation of the parameter α from even more inspiratory volumes would be statistically beneficial. Alternatively, free-breathing ufSSFP acquisitions could be adopted for α-mapping [156, 206]. However, to date, free-breathing techniques require long acquisition times exceeding 5 to 15 minutes for multi-volumetric imaging. For similar scan times, FD-MRI provides not only ventilation-weighted, but also perfusion-weighted imaging, and blood arrival time maps, and may thus be preferred over free-breathing α-mapping.

Chapter 4. Three-dimensional oxygen enhancement maps were calculated from multi-volumetric ufSSFP acquisitions in healthy volunteers. The oxygen enhancement in the whole lung using ufSSFP was found to be on average 7%. The use of the lung model proved to mitigate residual density modulations, thus offering accurate and robust oxygen enhancement quantification. Interestingly, a similar correction for residual density modulations in OE-MRI has successively been proposed for 3D OE-MRI using UTE imaging [56].

As ufSSFP OE-MRI is based on multi-volumetric breath-hold imaging, the limitations are similar to the one previously described for α-mapping (Chapter 3). In general, OE-MRI requires measurements in both normoxic and hyperoxic conditions, therefore doubling the scan time and hampering the transition to clinical settings. Moreover, oxygen is delivered with a face mask, which might not be well tolerated by some individuals. Nevertheless, the use of oxygen as an endogenous contrast agent remains appealing for specific physiological studies.

Chapter 5. Dynamic and steady-state oxygen-dependent lung relaxometry using IR-ufSSFP was evaluated in healthy subjects. On average, oxygen-breathing shortened the whole lung T_1 by 8% (statistically significant), however, no significant changes in T_2 were observed. The technique allowed to map ΔT_1 (shortening of T_1 after hyperoxia), as well as the oxygen wash-in and wash-out time constant, related to the T_1 rate of change.

A limitation of the technique is its restriction to image only one slice per breath-hold (9 seconds). Nevertheless, considering that 8 coronal slices would be sufficient to cover the majority of the

lung, it appears feasible to calculate whole-lung ΔT_1 maps in clinically acceptable times (about 10-15 min, considering 5 min of oxygen wash-in). On the other hand, for dynamic oxygen-enhanced relaxometry, continuous imaging of the same slice (~15 min) is needed. This would result in an intolerable measurement time to cover the whole lung. A considerably reduced scan time might be achieved by combining IR-ufSSFP with simultaneous multi-slice imaging.

OE-relaxometry provides maps related to a mixed pulmonary function comprising ventilation, perfusion, as well as diffusion (i.e., oxygen uptake from the alveolar air space to the pulmonary blood). It has thus the potential to add additional information to ventilation-weighted and perfusion-weighted imaging modalities such as FD-MRI. Further evaluation of OE-relaxometry in large cohorts is required to establish its radiological value, e.g., for the assessment of focal defects and the quantification of lung function impairment.

Chapter 6. Static SER-mapping of the lung with ufSSFP was found to outperform VIBE and delivered high-quality images suited for diagnostic radiology. The ufSSFP-SER in the lung (99%) was higher than in the blood and other tissues, accentuating the visualization of the lung parenchyma. In healthy lung, SER-maps were homogeneous while in patients, the impairments quantified on SER-maps coincided well with the functional defects identified on ^{99m}Tc-MAA-SPECT data (fair intermodality agreement).

Imaging for SER-mapping was performed in inspiratory breath-hold; once before and once after contrast agent administration. Since the signal increase as induced by the contrast agent (~100%) is at least one order of magnitude larger than possible density modulations (< 5-10%) caused by the non-perfect reproducibility of the breath-hold inspiratory levels, density corrections were not required (cf. Chapters 3 and 4). As many other techniques, SER-mapping is not a quantitative measurement, but a relative measurement and hence requires normative values as comparison.

Three-dimensional ufSSFP requires breath-holding manoeuvres that might be challenging or impossible to perform for some subjects (e.g., infants), but this limitation might be overcome by free-breathing acquisitions (e.g., self-navigated). Another disadvantage of SER-mapping is the need for Gadolinium-based contrast agents, which are not indicated in patients with renal failure, children, pregnant women, or when frequent follow-up imaging is desired. Furthermore, contrast agents might cause allergic reactions and deposits in the tissues, with yet unknown effects to the body [122, 207]. However, SER-mapping can easily be included into common contrast-enhanced MR protocols and has clinical potential for routine application. It allows mapping perfusion-related physiological processes of the lung parenchyma from only two breath-hold acquisitions (each taking 10-15 seconds), which in turn provide 3D morphological clinical

imaging with 2.5 mm isotropic resolution usable for the differential diagnosis and disease assessment [47].

7.2 Future work

To further advance functional lung MRI based on ufSSFP, future investigations are required with focus on the implementation of improved acquisitions schemes as well as on the clinical evaluation and validation of the proposed techniques. Particular emphasis needs to be placed on the automatization of our methods for the online quantification of functional and morpho-pathological biomarkers.

7.2.1 Implementation of new acquisition schemes

3D ufSSFP is still limited by breath-holding manoeuvres, which might not be well tolerated by some individuals. To overcome this limitation, a free-breathing multi-slice 2D ufSSFP acquisition scheme or a 3D self-navigated stack-of-stars ufSSFP sequence with parallel imaging and iterative reconstruction may be adopted for morpho-functional imaging. Preliminary results are presented in Refs. [156, 206] and exemplarily shown here in Figure 7.1 for the case of free-breathing multi-slice 2D ufSSP.

SER-mapping has proven that the signal of ufSSFP sequences can be increased considerably through gadolinium injection. It is thus appealing to develop a three-dimensional time-resolved ufSSFP sequence for dynamic contrast-enhanced imaging, e.g., using k-space undersampling and view-sharing [203].

Particularly for 3T imaging, field inhomogeneities might adversely affect ufSSFP image quality (cf. Fig. 2.4), yielding banding artifacts and reduced signal due to off-resonances. To this end, improved shimming techniques might be adopted, as well as new acquisition schemes as currently being investigated [208].

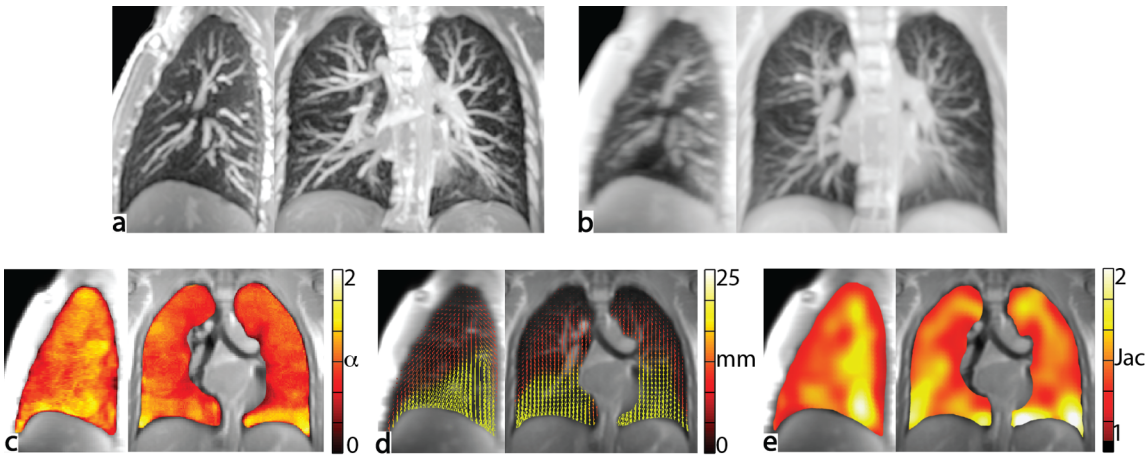

Figure 7.1. Sagittal (maximum intensity projection, MIP = 10 mm) and coronal (MIP = 20 mm) views of 3D ufSSFP (a) in breath-holding (15 seconds) and 2D multi-slice ufSSFP (b) in free-breathing (coronale orientation, 5 min scan time to obtain 48 volumetric datasets). Respiratory-maps (a), lung deformation field (b) and Jacobian expansion (c) resulting from the free-breathing imaging. The respiratory index represents the expansion of each voxel as a function of the mean lung expansion (cf. Chapter 3). The deformation field indicates the direction and strength of motion dynamic from expiration-to-inspiration phases. The determinant of the Jacobian (Jac) is a voxel-wise estimation of lung expansion/compression: if Jac>1, the local tissue expands (e.g., for Jac = 2, its size was doubled from expiration-to-inspiration), and Jac<1 represents tissue contraction.

7.2.2 Clinical evaluation and validation

FD-MRI has already been validated against ^{3}He-MRI as well as DCE-MRI, and is becoming a relevant clinical method for the longitudinal quantification of ventilation-perfusion defects in children with CF. The emphasis of future studies should therefore be on the assessment of its reproducibility and broad application across diverse patient groups. Moreover, FD-MRI may be applied to study the effects of drugs such as bronchodilators.

3D α-mapping has shown promise to quantify ventilation impairments in a small cohort of children with CF while SER mapping showed initial potential in COPD patients. Future work may thus concentrate on the investigation of their radiological outcome in large cohorts of patients and against other functional techniques such as FD-MRI or DCE-MRI. The applicability of the proposed methods can also be expanded to investigate pulmonary physiological alterations in cardiac diseases (e.g., congestive heart failure). Moreover, 3D ufSSFP OE-MRI, and OE pulmonary relaxometry may be studied in children with CF.

7.2.3 Quantification and automatization

Future work will include the quantification of the disease with the presented techniques by studying the extent of pathological pulmonary tissue and function alterations. To this end, algorithms involving adaptive k-means thresholding [204] for data clustering combined with multivariate data analysis [209] may be investigated to evaluate simultaneously many variables and patterns in the data.

Of particular importance for future studies is the development of automatized procedures using deep learning approaches with both recurrent and convolutional neural networks [210, 211]. In preliminary work, an approach involving a neural network of multi-dimensional gated recurrent units [212] is employed to automatize the process of lung segmentation (see Fig. 7.2) [205], which is required to quantify the percentage of defects in the lung with FD-MRI and to calculate α-maps. The ultimate goal for the future is to implement these post-processing steps for online evaluation of functional images (i.e., directly at the scanner). In addition, deep learning applied to pulmonary MR imaging may be extended to automatically detect and quantify functional and morphological abnormalities (e.g., ventilation and perfusion defects, mucus plugs, atelectasis, emphysema, fibrosis, and lesions).

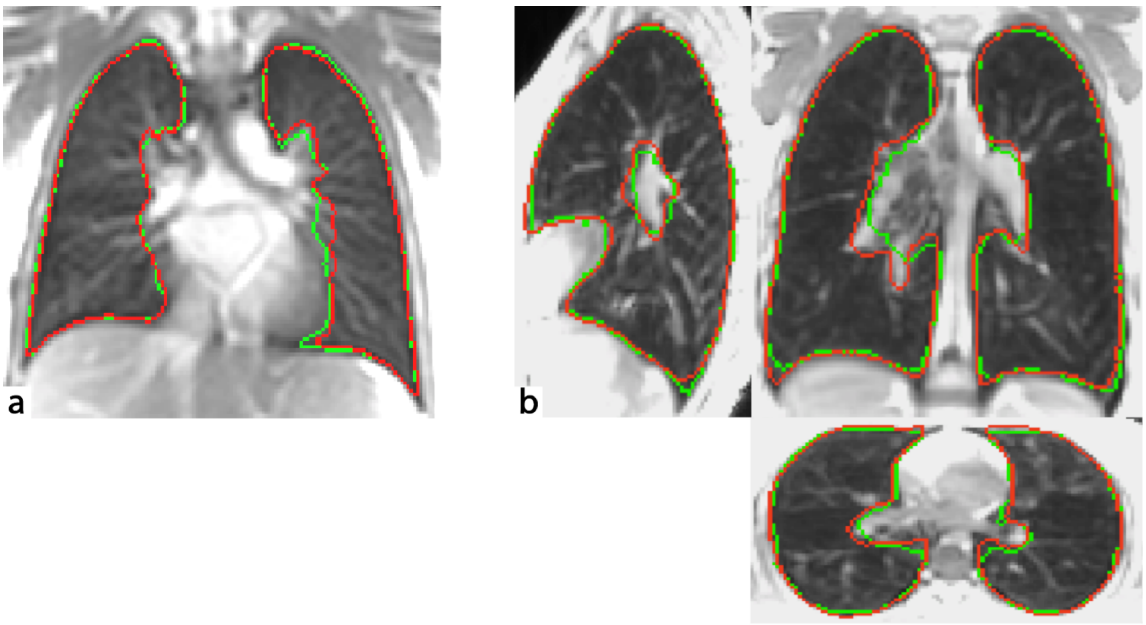

Figure 7.2. Lung segmentation of 2D ufSSFP (a) and 3D ufSSFP (b) datasets of a patient with cystic fibrosis performed manually by a human observer (green) and automatically by a trained neural network (red).

7.3 Conclusion

This thesis has shown novel and improved techniques to assess pulmonary function using proton ufSSFP MRI, which is widely available. The ufSSFP acquisition schemes have substantially increased the image quality and revealed to be a promising strategy for clinical applicability. While OE-MRI is yet hindered in a clinical context by a rather laborious setup and may be employed for specific research studies, FD-MRI, α-mapping, and SER-mapping have already demonstrated promise for clinical applications and may be used for patient monitoring.

To conclude, I hope, this work will inspire other scientists and improve the management of respiratory diseases.

References

1. Bousquet J, Khaltaev NG, Cruz AA (2007) *Global Surveillance, Prevention and Control of Chronic Respiratory Diseases: A Comprehensive Approach*. Geneva : World Health Organization.

2. Ley-Zaporozhan J, Ley S, Kauczor H-U (2008) *Morphological and functional imaging in COPD with CT and MRI: present and future*. Eur Radiol 18:510–521.

3. Beers MF, Morrisey EE (2011) *The three R's of lung health and disease: repair, remodeling, and regeneration*. J Clin Invest 121:2065–2073.

4. Wielpütz M, Kauczor HU (2012) *MRI of the lung: State of the art*. Diagnostic Interv. Radiol. 18:344–353.

5. Bajc M, Neilly JB, Miniati M, et al (2009) *EANM guidelines for ventilation/perfusion scintigraphy : Part 1. Pulmonary imaging with ventilation/perfusion single photon emission tomography.* Eur J Nucl Med Mol Imaging 36:1356–1370.

6. Sarkar M, Madabhavi I, Niranjan N, Dogra M (2015) *Auscultation of the respiratory system*. Ann Thorac Med 10:158–168.

7. Kramme R, Hoffmann KP, Pozos R (2011) *Springer Handbook of Medical Technology*. Springer Berlin Heidelberg.

8. West JB (2008) *Pulmonary Pathophysiology: The Essentials*. Lippincott Williams & Wilkins.

9. Beydon N, Pin I, Matran R, et al (2003) *Pulmonary function tests in preschool children with asthma.* Am J Respir Crit Care Med 168:640–644.

10. Mata J, Altes T, Truwit J, et al (2011) *Characterization and Detection of Physiologic Lung Changes Before and After Placement of Bronchial Valves Using Hyperpolarized Helium-3 MR Imaging. Preliminary Study*. Acad Radiol 18:1195–1199.

11. Kruger SJ, Nagle SK, Couch MJ, et al (2016) *Functional imaging of the lungs with gas agents*. J Magn Reson Imaging 43:295–315.

12. A.W.M. TH (2002) *Detecting early structural lung damage in cystic fibrosis*. Pediatr Pulmonol 34:228–231.

13. Ramsey KA, Rosenow T, Turkovic L, et al (2015) *Lung Clearance Index and Structural Lung Disease on Computed Tomography in Early Cystic Fibrosis*. Am J Respir Crit Care Med 193:60–67.

14. Kaireit TF, Sorrentino SA, Renne J, et al (2017) *Functional lung MRI for regional monitoring of patients with cystic fibrosis.* PLoS One 12:e0187483.

15. Wielpütz MO, Heußel CP, Herth FJF, Kauczor H-U (2014) *Radiological Diagnosis in Lung Disease: Factoring Treatment Options Into the Choice of Diagnostic Modality*. Dtsch Arztebl Int 111:181–187.

16. van Beek EJR, Hoffman EA (2008) *Functional Imaging: CT and MRI*. Clin. Chest Med. 29:195–216.

17. Bajc M, Neilly JB, Miniati M, et al (2009) *EANM guidelines for ventilation/perfusion scintigraphy : Part 2. Algorithms and clinical considerations for diagnosis of pulmonary emboli with V/P(SPECT) and MDCT.* Eur J Nucl Med Mol Imaging 36:1528–1538.

18. Capitanio S, Nordin AJ, Noraini AR, Rossetti C (2016) *PET/CT in nononcological lung diseases: current applications and future perspectives*. Eur Respir Rev 25:247 LP-258.

19. Roach PJ, Bailey DL, Harris BE (2008) *Enhancing Lung Scintigraphy With Single-Photon Emission Computed Tomography*. Semin. Nucl. Med. 38:441–449.

20. Patz EF, Coleman RE (2005) *Nuclear medicine techniques*. In: Mason RJ, Murray J, Broaddus VC, Nadel J, editors. Textbook of respiratory medicine. Philadelphia: Saunders Elsevier; 2005. p 594–599.

21. Bailey DL, Willowson KP (2013) *An evidence-based review of quantitative SPECT imaging and potential clinical applications.* J Nucl Med 54:83–89.

22. Pearce MS, Salotti JA, Little MP, et al (2012) *Radiation exposure from CT scans in childhood and subsequent risk of leukaemia and brain tumours: A retrospective cohort study*. Lancet 380:499–505.

23. Sodickson A, Baeyens PF, Andriole KP, et al (2009) *Recurrent CT, cumulative radiation exposure, and associated radiation-induced cancer risks from CT of adults.* Radiology 251:175–184.

24. Kuo W, Ciet P, Tiddens HAWM, et al (2014) *Monitoring Cystic Fibrosis Lung Disease by Computed Tomography. Radiation Risk in Perspective*. Am J Respir Crit Care Med 189:1328–1336.

25. De Jong PA, Mayo JR, Golmohammadi K, et al (2006) *Estimation of cancer mortality associated with repetitive computed tomography scanning*. Am J Respir Crit Care Med 173:199–203.

26. Hartwig V, Giovannetti G, Vanello N, et al (2009) *Biological Effects and Safety in Magnetic Resonance Imaging: A Review*. Int J Environ Res Public Health 6:1778–1798.

27. Formica D, Silvestri S (2004) *Biological effects of exposure to magnetic resonance imaging: an overview*. Biomed Eng Online 3:11.

28. Kauczor HU, Wielpütz MO (2017) *MRI of the Lung*, Second Ed. Springer Berlin Heidelberg.

29. Wild JM, Marshall H, Bock M, et al (2012) *MRI of the lung (1/3): Methods*. Insights Imaging 3:345–353.

30. Biederer J, Beer M, Hirsch W, et al (2012) *MRI of the lung (2/3). Why ... when ... how?* Insights Imaging 3:355–371.

31. Biederer J, Mirsadraee S, Beer M, et al (2012) *MRI of the lung (3/3)—current applications and future perspectives*. Insights Imaging 3:373–386.

32. Ley-Zaporozhan J, Puderbach M, Kauczor H-U (2008) *MR for the Evaluation of Obstructive Pulmonary Disease*. Magn Reson Imaging Clin N Am 16:291–308.

33. Nyilas S, Bauman G, Sommer G, et al (2017) *Novel magnetic resonance technique for functional imaging of cystic fibrosis lung disease.* Eur Respir J. doi:10.1183/ 13993003.01464-2017.

34. Mulkern R, Haker S, Mamata H, et al (2014) *Lung parenchymal signal intensity in MRI: A technical review with educational aspirations regarding reversible versus irreversible transverse relaxation effects in common pulse sequences*. Concepts Magn Reson Part A 43A:29–53.

35. Walkup LL, Woods JC (2014) *Translational applications of hyperpolarized 3He and 129Xe*. NMR Biomed 27:1429–1438.

36. Couch MJ, Ball IK, Li T, et al (2014) *Inert fluorinated gas MRI: a new pulmonary imaging modality*. NMR Biomed. 27:1525–1534.

37. Roos JE, McAdams HP, Kaushik SS, Driehuys B (2015) *Hyperpolarized Gas MR Imaging: Technique and Applications.* Magn Reson Imaging Clin N Am 23:217–229.

38. Fain S, Schiebler ML, McCormack DG, Parraga G (2010) *Imaging of lung function using hyperpolarized helium-3 magnetic resonance imaging: Review of current and emerging translational methods and applications.* J Magn Reson Imaging 32:1398–408.

39. Salerno M, Altes TA, Mugler JPIII, et al (2001) *Hyperpolarized noble gas MR imaging of the lung: potential clinical applications*. Eur J Radiol 40:347-353.

40. Yablonskiy D, Sukstanskii A, Quirk J (2015) *Diffusion lung imaging with hyperpolarized gas MRI*. NMR Biomed 30:p3448.

41. Stewart N, Ho-Fung C, Hughes P, et al (2018) *Comparison of 3He and 129Xe MRI for evaluation of lung microstructure and ventilation at 1.5T*. J Magn Reson Imaging. doi: 10.1002/jmri.25992.

42. Johnson KM, Fain SB, Schiebler ML, Nagle S (2013) *Optimized 3D Ultrashort Echo Time Pulmonary MRI*. Magn Reson Med 70:1241–1250.

43. Mugler III JP, Meyer C, Pfeuffer J, et al (2017) *Accelerated Stack-of-Spirals Breath-hold UTE Lung Imaging*. Proc. Intl. Soc. Mag. Reson. Med. 25, p 4904.

44. Delacoste J, Chaptinel J, Beigelman-Aubry C, et al (2018) *A double echo ultra short echo time (UTE) acquisition for respiratory motion-suppressed high resolution imaging of the lung.* Magn Reson Med 79:2297–2305.

45. Bieri O (2013) *Ultra-fast steady state free precession and its application to in vivo 1H morphological and functional lung imaging at 1.5 tesla*. Magn Reson Med 70:657–663.

46. Bauman G, Santini F, Pusterla O, Bieri O (2017) *Pulmonary relaxometry with inversion recovery ultra-fast steady-state free precession at 1.5T*. Magn Reson Med 77:74–82.

47. Heye T, Sommer G, Miedinger D, et al (2015) *Ultrafast 3D balanced steady-state free precession MRI of the lung: Assessment of anatomic details in comparison to low-dose CT.* J Magn Reson Imaging 42:602–609.

48. Tsao J, Kozerke S (2012) *MRI temporal acceleration techniques.* J Magn Reson Imaging 36:543–560.

49. Zhu Y, Gao S, Cheng L, Bao S (2013) *Review: K-space trajectory development*. In: 2013 IEEE International Conference on Medical Imaging Physics and Engineering. pp 356–360.

50. Tsao J (2010) *Ultrafast imaging: principles, pitfalls, solutions, and applications.* J Magn Reson Imaging 32:252–266.

51. Buschle LR, Kurz FT, Kampf T, et al (2017) *Dephasing and diffusion on the alveolar surface.* Phys Rev E 95:22415.

52. Wielputz MO, Mall MA (2015) *Imaging modalities in cystic fibrosis: emerging role of MRI.* Curr Opin Pulm Med 21:609–616.

53. Voskrebenzev A, Greer M, Gutberlet M, et al (2018) *Detection of Chronic Lung Allograft Dysfunction Using Ventilation-Weighted Fourier Decomposition MRI.* Am J Transplant. doi: 10.1111/ajt.14759.

54. Capaldi DPI, Eddy RL, Svenningsen S, et al (2018) *Free-Breathing Pulmonary MR Imaging to Quantify Regional Ventilation*. Radiology 171993.

55. Higano NS, Fleck RJ, Spielberg DR, et al (2017) *Quantification of neonatal lung parenchymal density via ultrashort echo time MRI with comparison to CT.* J Magn Reson Imaging 46:992–1000.

56. Zha W, Kruger SJ, Johnson KM, et al (2017) *Pulmonary ventilation imaging in asthma and cystic fibrosis using oxygen-enhanced 3D radial ultrashort echo time MRI.* J Magn Reson Imaging. doi: 10.1002/jmri.25877.

57. West JB (2012) *Respiratory Physiology: The Essentials*. Wolters Kluwer Health/Lippincott Williams & Wilkins.

58. Barrett KE, Barman SM, Boitano S, Brooks HL (2009) *Ganong's Review of Medical Physiology* (Enhanced EB). McGraw-Hill Education.

59. Levitzky MG (2013) *Pulmonary Physiology*, Eighth Edition. McGraw-Hill Education.

60. Ruiz Villarreal M (2007) *Respiratory system complete, https://commons.wikimedia.org/wiki/File:Respiratory_system_complete_en.svg, Accessed 24 Apr 2018.*

61. Hsia CCW, Hyde DM, Weibel ER (2016) *Lung Structure and the Intrinsic Challenges of Gas Exchange*. Compr Physiol 6:827–895.

62. Weibel ER (1963) *Morphometry of the human lung*. Academic Press.

63. Weibel ER (2009) *What makes a good lung?* Swiss Med Wkly 139:375–386.

64. Lynch PJ, Jaffe CC (2006) *Thoracic Anatomy, Yale University Center for Advanced Instructional Media, https://commons.wikimedia.org/wiki/File:Thoracic_anatomy.jpg, Accessed 24 Apr 2018.*

65. Bieri O (2014) *MR Gravimetry (MRG) of the Lung*. Proc. Intl. Soc. Mag. Reson. Med. 22, p 2306.

66. Hopkins SR, Henderson a C, Levin DL, et al (2007) *Vertical gradients in regional lung density and perfusion in the supine human lung: the Slinky effect.* J Appl Physiol 103:240–248.

67. Petersson J, Sánchez-Crespo A, Larsson SA, Mure M (2007) *Physiological imaging of the lung: single-photon-emission computed tomography (SPECT).* J Appl Physiol 102:468–476.

68. Horn FC, Deppe MH, Marshall H, et al (2014) *Quantification of regional fractional ventilation in human subjects by measurement of hyperpolarized 3He washout with 2D and 3D MRI.* J Appl Physiol 116:129–39.

69. Musch G, Layfield JD, Harris RS, et al (2002) *Topographical distribution of pulmonary perfusion and ventilation, assessed by PET in supine and prone humans*. J Appl Physiol 93:1841–1851.

70. Sá RC, Cronin M V, Cortney Henderson A, et al (2010) *Vertical distribution of specific ventilation in normal supine humans measured by oxygen-enhanced proton MRI*. J Appl Physiol 109:1950–1959.

71. Arai TJ, Theilmann RJ, Sá RC, et al (2016) *The effect of lung deformation on the spatial distribution of pulmonary blood flow*. J Physiol. doi: 10.1113/JP272030.

72. Hopkins SR, Prisk GK (2010) *Lung Perfusion Measured Using Magnetic Resonance Imaging: New Tools for Physiological Insights Into the Pulmonary Circulation*. J Magn Reson Imaging 32:1287–1301.

73. Fichele S, Woodhouse N, Swift AJ, et al (2004) *MRI of helium-3 gas in healthy lungs: posture related variations of alveolar size.* J Magn Reson Imaging 20:331–335.

74. Kjørstad Å, Corteville DMR, Henzler T, et al (2015) *Non-invasive quantitative pulmonary V/Q imaging using Fourier decomposition MRI at 1.5T*. Z Med Phys 25:326–332.

75. Euler US v., Liljestrand G (1946) *Observations on the Pulmonary Arterial Blood Pressure in the Cat*. Acta Physiol Scand 12:301–320.

76. Allgood RJ, Wolfe WG, Ebert PA, DC S (1968) *Effects of carbon dioxide on bronchoconstriction after pulmonary artery occlusion*. Am J Physiol Content 214:772–775.

77. Lele EE, Hantos Z, Bitay M, et al (2011) *Bronchoconstriction during alveolar hypocapnia and systemic hypercapnia in dogs with a cardiopulmonary bypass*. Respir Physiol Neurobiol 175:140–145.

78. Schenk J (1998) *The role of magnetic susceptibility in magnetic resonance imaging: MRI magnetic compatibility of the first and second kinds*. Med Phys 23:815–850.

79. Hatabu H, Alsop DC, Listerud J, et al (1999) *T2* and proton density measurement of normal human lung parenchyma using submillisecond echo time gradient echo magnetic resonance imaging.* Eur J Radiol 29:245–252.

80. Puderbach M, Hintze C, Ley S, et al (2007) *MR imaging of the chest: a practical approach at 1.5T.* Eur J Radiol 64:345–355.

81. Patel MR, Klufas RA, Alberico RA, Edelman RR (1997) *Half-fourier acquisition single-shot turbo spin-echo (HASTE) MR: comparison with fast spin-echo MR in diseases of the brain.* Am J Neuroradiol 18:1635 LP-1640.

82. Pipe J (1999) *Motion correction with PROPELLER MRI: Application to head motion and free-breathing cardiac imaging*. Magn Reson Med 42:963–969.

83. Bydder GM, Young IR (1985) *MR imaging: clinical use of the inversion recovery sequence.* J Comput Assist Tomogr 9:659–675.

84. Carr HY (1958) *Steady-State Free Precession in Nuclear Magnetic Resonance*. Phys Rev 112:1693–1701.

85. Rofsky NM, Lee VS, Laub G, et al (1999) *Abdominal MR Imaging with a Volumetric Interpolated Breath-hold Examination*. Radiology 212:876–884.

86. Bergin CJ, Pauly JM, Macovski A (1991) *Lung parenchyma: projection reconstruction MR imaging.* Radiology 179:777–781.

87. Wielputz MO, Lee HY, Koyama H, et al (2018) *Morphological Characterization of Pulmonary Nodules With Ultrashort TE MRI at 3T.* AJR Am J Roentgenol 1–10.

88. Dournes G, Menut F, Macey J, et al (2016) *Lung morphology assessment of cystic fibrosis using MRI with ultra-short echo time at submillimeter spatial resolution*. Eur Radiol 26:3811–3820.

89. Robson MD, Gatehouse PD, Bydder M, Bydder GM (2003) *Magnetic Resonance: An Introduction to Ultrashort TE (UTE) Imaging*. J Comput Assist Tomogr 27:6.

90. Tyler D, Robson M, Henkelman R, et al (2007) *Magnetic resonance imaging with ultrashort TE (UTE) PULSE sequences: Technical considerations*. J Magn Reson Imaging 25:279–289.

91. Cheng H-LM, Stikov N, Ghugre NR, Wright GA (2012) *Practical medical applications of quantitative MR relaxometry.* J Magn Reson Imaging 36:805–824.

92. Hatabu H, Gaa J, Tadamura E, et al (1999) *MR imaging of pulmonary parenchyma with a half-Fourier single-shot turbo spin-echo (HASTE) sequence*. Eur J Radiol 29:152–159.

93. Arnold JFT, Kotas M, Fidler F, et al (2007) *Quantitative regional oxygen transfer imaging of the human lung*. J Magn Reson Imaging 26:637–645.

94. Gai N, Malayeri A, Bluemke D (2016) *Three-dimensional T1 and T2* mapping of human lung parenchyma using interleaved saturation recovery with dual echo ultrashort echo time imaging (ITSR-DUTE)*. J Magn Reson Imaging 45:1097–1104.

95. Edelman RR, Hatabu H, Tadamura E, et al (1996) *Noninvasive assessment of regional ventilation in the human lung using oxygen-enhanced magnetic resonance imaging.* Nat Med 2:1236–1239.

96. Löffler R, Müller CJ, Peller M, et al (2000) *Optimization and evaluation of the signal intensity change in multisection oxygen-enhanced MR lung imaging.* Magn Reson Med 43:860–6.

97. Ohno Y, Hatabu H, Higashino T, et al (2018) *Centrically reordered inversion recovery half-Fourier single-shot turbo spin-echo sequence: improvement of the image quality of oxygen-enhanced MRI*. Eur J Radiol 52:200–205.

98. Zhang W-J, Niven RM, Young SS, et al (2015) *Dynamic oxygen-enhanced magnetic resonance imaging of the lung in asthma-initial experience.* Eur J Radiol 84:318–326.

99. Triphan SMF, Breuer FA, Gensler D, et al (2015) *Oxygen enhanced lung MRI by simultaneous measurement of T1 and T2 * during free breathing using ultrashort TE.* J Magn Reson Imaging 41:1708–1714.

100. Yoshiharu O, Hiroto H, Daisuke T, et al (2002) *Dynamic oxygen-enhanced MRI reflects diffusing capacity of the lung*. Magn Reson Med 47:1139–1144.

101. Pracht ED, Arnold JFT, Wang T, Jakob PM (2005) *Oxygen-enhanced proton imaging of the human lung using T2**. Magn Reson Med 53:1193–1196.

102. Bauman G, Puderbach M, Deimling M, et al (2009) *Non-contrast-enhanced perfusion and ventilation assessment of the human lung by means of Fourier decomposition in proton MRI*. Magn Reson Med 62:656–664.

103. Scheffler K (2003) *On the transient phase of balanced SSFP sequences.* Magn Reson Med 49:781–783.

104. Bauman G, Bieri O (2017) *Matrix pencil decomposition of time-resolved proton MRI for robust and improved assessment of pulmonary ventilation and perfusion.* Magn Reson Med 77:336–342.

105. Bauman G, Lützen U, Ullrich M, et al (2011) *Pulmonary Functional Imaging: Qualitative Comparison of Fourier Decomposition MR Imaging with SPECT/CT in Porcine Lung*. Radiology 260:551–559.

106. Bauman G, Puderbach M, Heimann T, et al (2013) *Validation of Fourier decomposition MRI with dynamic contrast-enhanced MRI using visual and automated scoring of pulmonary perfusion in young cystic fibrosis patients*. Eur J Radiol 82:2371–2377.

107. Haacke EM, Brown RW, Thompson MR, Venkatesan R (1999) *Haacke - Magnetic Resonance Imaging - Physical Principles and Sequence Design.pdf*. J. Appl. Phys. 109:914

108. Scheffler K, Lehnhardt S (2003) *Principles and applications of balanced SSFP techniques*. Eur Radiol 13:2409–2418.

109. Bieri O, Scheffler K (2013) *Fundamentals of balanced steady state free precession MRI*. J. Magn. Reson. Imaging 38:2–11.

110. Huang T-Y, Huang I-J, Chen C-Y, et al (2002) *Are TrueFISP images T2/T1-weighted?* Magn Reson Med 48:684–688.

111. Scheffler K, Hennig J (2003) *Is TrueFISP a gradient-echo or a spin-echo sequence?* Magn Reson Med 49:395–397.

112. Pennati F, Quirk JD, Yablonskiy DA, et al (2014) *Assessment of regional lung function with multivolume (1)H MR imaging in health and obstructive lung disease: comparison with (3)He MR imaging.* Radiology 273:580–590.

113. Khadija S, Fumin G, P.I. CD, et al (2016) *Ultrashort echo time MRI biomarkers of asthma*. J Magn Reson Imaging 45:1204–1215.

114. Jobst BJ, Triphan SMF, Sedlaczek O, et al (2015) *Functional Lung MRI in Chronic Obstructive Pulmonary Disease: Comparison of T1 Mapping, Oxygen-Enhanced T1 Mapping and Dynamic Contrast Enhanced Perfusion*. PLoS One 10:e0121520.

115. Jakob PM, Wang T, Schultz G, et al (2004) *Assessment of human pulmonary function using oxygen-enhanced T(1) imaging in patients with cystic fibrosis*. Magn Reson Med 51:1009–1016.

116. Jung B, Krombach GA, Gunther RW, Buecker A (2004) *Is postcontrast trueFISP imaging advantageous?* Invest Radiol 39:517–523.

117. Pusterla O, Bauman G, Bieri O (2016) *Balanced SSFP pulmonary signal enhancement after contrast agent injection*. Proc. Intl. Soc. Mag. Reson. Med. 24, p 2916.

118. Usemann J, Yammine S, Singer F, Latzin P (2017) *Inert gas washout: background and application in various lung diseases.* Swiss Med Wkly 147:w14483.

119. Mugler JP, Altes TA (2013) *Hyperpolarized 129Xe MRI of the human lung*. J. Magn. Reson. Imaging 37:313–331.

120. Hatabu H, Tadamura E, Levin DL, et al (1999) *Quantitative assessment of pulmonary perfusion with dynamic contrast-enhanced MRI.* Magn Reson Med 42:1033–1038.

121. Ley S, Ley-Zaporozhan J (2012) *Pulmonary perfusion imaging using MRI: clinical application*. Insights Imaging 3:61–71.

122. Grobner T (2006) *Gadolinium – a specific trigger for the development of nephrogenic fibrosing dermopathy and nephrogenic systemic fibrosis?* Nephrol Dial Transplant 21:1104–1108.

123. Bauman G, Scholz A, Rivoire J, et al (2013) *Lung ventilation- and perfusion-weighted Fourier decomposition magnetic resonance imaging: In vivo validation with hyperpolarized 3He and dynamic contrast-enhanced MRI*. Magn Reson Med 69:229–237.

124. Sommer G, Bauman G, Koenigkam-Santos M, et al (2013) *Non-contrast-enhanced preoperative assessment of lung perfusion in patients with non-small-cell lung cancer using Fourier decomposition magnetic resonance imaging*. Eur J Radiol 82:e879–e887.

125. McGibney G, Smith M, Nichols S, Crawley A (2005) *Quantitative evaluation of several partial fourier reconstruction algorithms used in mri*. Magn Reson Med 30:51–59.

126. Deshpande V, Yiu-Cho C, Qiang Z, et al (2002) *Reduction of transient signal oscillations in true-FISP using a linear flip angle series magnetization preparation*. Magn Reson Med 49:151–157.

127. Bieri O, Markl M, Scheffler K (2005) *Analysis and compensation of eddy currents in balanced SSFP*. Magn Reson Med 54:129–137.

128. Griswold MA, Jakob PM, Heidemann RM, et al (2002) *Generalized autocalibrating partially parallel acquisitions (GRAPPA)*. Magn Reson Med 47:1202–1210.

129. Hargreaves B, Vasanawala S, Pauly J, Nishimura D (2001) *Characterization and reduction of the transient response in steady-state MR imaging*. Magn Reson Med 46:149–158.

130. Chefdhotel C, Hermosillo G, Faugeras O (2002) *Flows of diffeomorphisms for multimodal image registration*. In: Proc. IEEE Int. Symp. Biomed. Imaging. Washington, DC, USA, July 2002., p p 753–756.

131. Maleike D, Nolden M, Meinzer HP, Wolf I (2009) *Interactive segmentation framework of the Medical Imaging Interaction Toolkit*. Comput Methods Programs Biomed 96:72–83.

132. Christian S, Serghei C, Andreas V, et al (2014) *Performance of perfusion-weighted Fourier decomposition MRI for detection of chronic pulmonary emboli*. J Magn Reson Imaging 42:72–79.

133. Kong X, Sheng HX, Lu GM, et al (2014) *Xenon-enhanced dual-energy CT lung ventilation imaging: Techniques and clinical applications*. Am. J. Roentgenol. 202:309–317.

134. Guerrero, Sanders K, Castillo E, Zhang Y, Bidaut L, Pan T KR (2006) *Dynamic ventilation imaging from four-dimensional computed tomography*. Phys Med Biol 51:777.

135. Simon BA *Non-Invasive Imaging of Regional Lung Function using X-Ray Computed Tomography*. J Clin Monit Comput 16:433–442.

136. Hopkins SR, Wielpütz MO, Kauczor H-U (2012) *Imaging lung perfusion.* J Appl Physiol 113:328–39.

137. Pusterla O, Bauman G, Wielpütz MO, et al (2016) *Fast 3D quantitative 1H ventilation imaging of the human lung at 1.5T with SSFP*. Proc. Intl. Soc. Mag. Reson. Med. 24, p 2917.

138. Staring M, Bakker ME, Stolk J, et al (2014) *Towards local progression estimation of pulmonary emphysema using CT.* Med Phys 41:21905.

139. Stoel BC, Putter H, Bakker ME, et al (2008) *Volume correction in computed tomography densitometry for follow-up studies on pulmonary emphysema.* Proc Am Thorac Soc 5:919–924.

140. Zapke M, Topf H-G, Zenker M, et al (2006) *Magnetic resonance lung function – a breakthrough for lung imaging and functional assessment? A phantom study and clinical trial*. Respir Res 7:1–9.

141. Hopkins SR, Arai TJ, Henderson AC, et al (2010) *Lung volume does not alter the distribution of pulmonary perfusion in dependent lung in supine humans*. J Physiol 588:4759–4768.

142. Bieri O (2014) *A Method for Visualization of Parenchyma and Airspaces from 3D Ultra-Fast Balanced SSFP Imaging of the Lung at 1.5T*. Proc. Intl. Soc. Mag. Reson. Med. 22, p 2300.

143. Achenbach T, Weinheimer O, Buschsieweke C, et al (2004) *Fully automatic detection and quantification of emphysema on thin section MD-CT of the chest by a new and dedicated software*. Rofo 176:1409–1415.

144. Bauman G, Pusterla O, Bieri O (2015) *Ultra-fast Steady-State Free Precession Pulse Sequence for Fourier Decomposition Pulmonary MRI*. Magn. Reson. Med. 75:1647-53.

145. Klein S, Staring M, Murphy K, et al (2010) *Elastix: A toolbox for intensity-based medical image registration*. IEEE Trans Med Imaging 29:196–205.

146. Low DA, Harms WB, Mutic S, Purdy J a (1998) *A technique for the quantitative evaluation of dose distributions.* Med Phys 25:656–61.

147. Eichinger M, Optazaite D-E, Kopp-Schneider A, et al (2012) *Morphologic and functional scoring of cystic fibrosis lung disease using MRI*. Eur J Radiol 81:1321–1329.

148. Ley-Zaporozhan J, Ley S, Eberhardt R, et al (2007) *Assessment of the relationship between lung parenchymal destruction and impaired pulmonary perfusion on a lobar level in patients with emphysema*. Eur J Radiol 63:76–83.

149. Sergiacomi G, Sodani G, Fabiano S, et al (2003) *MRI lung perfusion 2D dynamic breath-hold technique in patients with severe emphysema.* In Vivo 17:319–324.

150. Zaporozhan J, Ley S, Gast KK, et al (2004) *Functional Analysis in Single-Lung Transplant Recipients: A Comparative Study of High-Resolution CT, 3He-MRI, and Pulmonary Function Tests*. Chest 125:173–181.

151. Voskrebenzev A, Gutberlet M, Becker L, et al (2016) *Reproducibility of fractional ventilation derived by Fourier decomposition after adjusting for tidal volume with and without an MRI compatible spirometer*. Magn Reson Med. 76(5):1542-1550.

152. Stadler A, Jakob PM, Griswold M, et al (2005) *T1 mapping of the entire lung parenchyma: Influence of the respiratory phase in healthy individuals*. J Magn Reson Imaging 21:759–764.

153. Kohlmann P, Strehlow J, Jobst B, et al (2015) *Automatic lung segmentation method for MRI-based lung perfusion studies of patients with chronic obstructive pulmonary disease*. Int J Comput Assist Radiol Surg 10:403–417.

154. Tustison NJ, Qing K, Wang C, et al (2015) *Atlas-based estimation of lung and lobar anatomy in proton MRI*. Magn. Reson. Med.

155. Coppo S, Piccini D, Bonanno G, et al (2015) *Free-running 4D whole-heart self-navigated golden angle MRI: Initial results*. Magn. Reson. Med. 74:1306–1316.

156. Bauman G, Bieri O (2015) *Respiratory self-gating using 3D half-echo stack-of-stars TrueFISP (TrueSTAR)*. Proc. Intl. Soc. Mag. Reson. Med. 23, p 1467.

157. Pusterla O, Bauman G, Wielpütz MO, et al (2017) *Rapid 3D in vivo 1H human lung respiratory imaging at 1.5 T using ultra-fast balanced steady-state free precession*. Magn. Reson. Med. 78:1059–1069.

158. Kruger SJ, Fain SB, Johnson KM, et al (2014) *Oxygen-enhanced 3D radial ultrashort echo time magnetic resonance imaging in the healthy human lung*. NMR Biomed 27:1535–1541.

159. Nakagawa T, Sakuma H, Murashima S, et al (2001) *Pulmonary ventilation-perfusion MR imaging in clinical patients*. J Magn Reson Imaging 14:419–424.

160. Morgan AR, Parker GJM, Roberts C, et al (2014) *Feasibility assessment of using oxygen-enhanced magnetic resonance imaging for evaluating the effect of pharmacological treatment in COPD*. Eur J Radiol 83:2093–2101.

161. Ohno Y, Nishio M, Koyama H, et al (2012) *Oxygen-Enhanced MRI, Thin-Section MDCT, and Perfusion SPECT/CT: Comparison of Clinical Implications to Patient Care for Lung Volume Reduction Surgery*. Am J Roentgenol 199:794–802.

162. Pusterla O, Bauman G, Sommer G, et al (2015) *Three-dimensional oxygen-enhanced human lung MRI using ultra-fast balanced Steady-State Free Precession*. Proc. Intl. Soc. Mag. Reson. Med. 23, p 3978.

163. Haacke E, Brown R, Thompson M, Venkatesan R (1999) *Magnetic resonance imaging: physical principles and sequence design. 1999*. New York A John Wiley Sons.

164. Tadamura E, Hatabu H, Li W, et al (1997) *Effect of oxygen inhalation on relaxation times in various tissues*. J Magn Reson Imaging 7:220–225.

165. Jakob PM, Hillenbrand CM, Wang TT, et al (2001) *Rapid quantitative lung H-1 T-1 mapping*. J Magn Reson Imaging 14:795–799.

166. Staring M, Bakker ME, Shamonin DP, et al (2009) *Towards local estimation of emphysema progression using image registration*. Proc. SPIE 7259:72590O–9.

167. Pusterla O, Bauman G, Sommer G, Bieri O (2015) *How volume affects the pulmonary MRI signal: Investigations with 3D ultra-fast balanced Steady-State Free Precession*. Proc. Intl. Soc. Mag. Reson. Med. 23, p 1481.

168. Kanai T, Kadoya N, Ito K, et al (2014) *Evaluation of accuracy of B-spline transformation-based deformable image registration with different parameter settings for thoracic images*. J Radiat Res 55:1163–1170.

169. Petersson J, Glenny RW (2012) *Imaging regional PAO2 and gas exchange*. J Appl Physiol 113:340–352.

170. Robertson HT, Buxton RB (2012) *Imaging for lung physiology: What do we wish we could measure?* J Appl Physiol 113:317–327.

171. Hemberger KRF, Jakob PM, Breuer FA (2015) *Multiparametric oxygen-enhanced functional lung imaging in 3D.* MAGMA 28:217–26.

172. M. JP, Tungte W, Georg S, et al (2004) *Assessment of human pulmonary function using oxygen-enhanced T1 imaging in patients with cystic fibrosis*. Magn Reson Med 51:1009–1016.

173. Renne J, Lauermann P, Hinrichs JB, et al (2015) *Chronic Lung Allograft Dysfunction: Oxygen-enhanced T1-Mapping MR Imaging of the Lung*. Radiology 276:266–273.

174. Oppelt A, Graumann R, Barfuss H, et al (1986) *FISP: A new Fast Imaging Sequence*. Electromedica vol 3.

175. Failo R, Wielopolski PA, Tiddens HAWM, et al (2009) *Lung morphology assessment using MRI: A robust ultra-short TR/TE 2D steady state free precession sequence used in cystic fibrosis patients*. Magn Reson Med 61:299–306.

176. Bauman G, Bieri O (2016) *Reversed half-echo stack-of-stars TrueFISP (TrueSTAR)*. Magn Reson Med 76:583–590.

177. Rajaram S, Swift AJ, Capener D, et al (2012) *Lung morphology assessment with balanced steady-state free precession MR imaging compared with CT*. Radiology 263:569–577.

178. Schmitt P, Griswold MA, Jakob PM, et al (2004) *Inversion recovery TrueFISP: quantification of T1, T2, and spin density*. Magn Reson Med 51:661–667.

179. Pusterla O, Bauman G, Bieri O (2018) *Three-dimensional oxygen-enhanced MRI of the human lung at 1.5T with ultra-fast balanced steady-state free precession*. Magn Reson Med 79:246–255.

180. Ehses P, Seiberlich N, Ma D, et al (2013) *IR TrueFISP with a golden-ratio-based radial readout: Fast quantification of T1, T2, and proton density*. Magn Reson Med 69:71–81.

181. Santini F, Kawel-Boehm N, Greiser A, et al (2015) *Simultaneous T1 and T2 quantification of the myocardium using cardiac balanced-SSFP inversion recovery with interleaved sampling acquisition (CABIRIA)*. Magn Reson Med 74:365–371.

182. Kellman P, Herzka DA, Hansen MS (2014) *Adiabatic inversion pulses for myocardial T1 mapping*. Magn Reson Med 71:1428–1434.

183. Santini F, Patil S, Scheffler K (2011) *IceLuva: a scripting framework for MR image reconstruction based on free software*. Concepts Magn Reson Part B Magn Reson Eng 39:1–10.

184. Avants BB, Tustison NJ, Song G, et al (2011) *A reproducible evaluation of ANTs similarity metric performance in brain image registration*. Neuroimage 54:2033–2044.

185. Dietrich O, Gaass T, Reiser MF (2017) *T1 relaxation time constants, influence of oxygen, and the oxygen transfer function of the human lung at 1.5 T—A meta-analysis*. Eur J Radiol 86:252–260.

186. Arnold JFT, Fidler F, Wang T, et al (2004) *Imaging lung function using rapid dynamic acquisition of T 1-maps during oxygen enhancement*. Magn Reson Mater Physics, Biol Med 16:246–253.

187. Chon D, Simon BA, Beck KC, et al (2005) *Differences in regional wash-in and wash-out time constants for xenon-CT ventilation studies*. Respir Physiol Neurobiol 148:65–83.

188. Suga K, Nishigauchi K, Kume N, et al (1996) *Dynamic pulmonary SPECT of xenon-133 gas washout*. J Nucl Med 37:807–814.

189. Feinberg DA, Setsompop K (2013) *Ultra-fast MRI of the human brain with simultaneous multi-slice imaging*. J Magn Reson 229:90–100.

190. Pedersen H, Kozerke S, Ringgaard S, et al (2009) *k-t PCA: Temporally constrained k-t BLAST reconstruction using principal component analysis*. Magn Reson Med 62:706–716.

191. Thieme SF, Hoegl S, Nikolaou K, et al (2010) *Pulmonary ventilation and perfusion imaging with dual-energy CT*. Eur Radiol 20:2882–2889.

192. Semelka RC, Balci NC, Wilber KP, et al (2000) *Breath-hold 3D gradient-echo MR imaging of the lung parenchyma: Evaluation of reproducibility of image quality in normals and preliminary observations in patients with disease*. J Magn Reson Imaging 11:195–200.

193. Ohno Y, Murase K, Higashino T, et al (2007) *Assessment of bolus injection protocol with appropriate concentration for quantitative assessment of pulmonary perfusion by dynamic contrast-enhanced MR imaging*. J Magn Reson Imaging 25:55–65.

194. Mortensen J, Gutte H (2014) *SPECT/CT and pulmonary embolism*. Eur J Nucl Med Mol Imaging 41:81–90.

195. Biederer J, Both M, Graessner J, et al (2003) *Lung morphology: fast MR imaging assessment with a volumetric interpolated breath-hold technique: initial experience with patients.* Radiology 226:242–249.

196. Pusterla O, Bauman G, Bieri O (2017) *Three-dimensional oxygen-enhanced MRI of the human lung at 1.5T with ultra-fast balanced steady-state free precession*. Magn Reson Med. doi: 10.1002/mrm.26665.

197. Bauman G, Santini F, Pusterla O, Bieri O (2017) *Pulmonary relaxometry with inversion recovery ultra-fast steady-state free precession at 1.5T*. Magn Reson Med 77:74–82.

198. Hatabu H, Gaa J, Kim D, et al (1996) *Pulmonary perfusion: Qualitative assessment with dynamic contrast-enhanced MRI using ultra-short TE and inversion recovery turbo FLASH*. Magn Reson Med 36:503–508.

199. Biederer J, Graessner J, Heller M (2001) *Magnetic resonance imaging of the lung with a volumetric interpolated 3D-Gradient echo sequence - Magnetresonanztomographie der Lunge mit einer volumeninterpolierten 3D-Gradientenechosequenz*. Fortschr Röntgenstr 173:883–887.

200. Watson PF, Petrie A (2010) *Method agreement analysis: A review of correct methodology*. Theriogenology 73:1167–1179.

201. Vanbelle S (2016) *A New Interpretation of the Weighted Kappa Coefficients*. Psychometrika 81:399–410.

202. Almquist HM, Palmer J, Jonson B, Wollmer P (1997) *Pulmonary perfusion and density gradients in healthy volunteers.* J Nucl Med 38:962–966.

203. Song T, Laine AF, Chen Q, et al (2009) *Optimal k-Space Sampling for Dynamic Contrast-Enhanced MRI with an Application to MR Renography*. Magn Reson Med 61:1242–1248.

204. Otsu N (1979) *A Threshold Selection Method from Gray-Level Histograms*. IEEE Trans Syst Man Cybern 9:62–66.

205. Pusterla O, Andermatt S, Bauman G, et al (2018) *Deep Learning Lung Segmentation in Paediatric Patients*. Proc. Intl. Soc. Mag. Reson. Med. 26, p 4355.

206. Pusterla O, Bauman G, Bieri O (2017) *Free-Breathing Multi-Slice Ultra-Fast SSFP Acquisitions for Multi-Volumetric Morphological and Functional Lung Imaging*. Proc. Intl. Soc. Mag. Reson. Med. 25, p 4907.

207. Gulani V, Calamante F, Shellock FG, et al (2017) *Gadolinium deposition in the brain: summary of evidence and recommendations.* Lancet Neurol 16:564–570.

208. Bauman G, Pusterla O, Bieri O (2018) *Functional lung imaging with partially spoiled ultra-fast steady-state free precession at 1.5T and 3T*. Proc. Intl. Soc. Mag. Reson. Med. 26, p 4346.

209. Coubard OA (2013) *A method for processing multivariate data in medical studies*. Stat Med 32:3436–3448.

210. LeCun Y, Bengio Y, Hinton G (2015) *Deep learning*. Nature 521:436–444.

211. Krizhevsky A, Sutskever I, Hinton GE (2012) *ImageNet Classification with Deep Convolutional Neural Networks*. In: Pereira F, Burges CJC, Bottou L, Weinberger KQ (eds) Advances in Neural Information Processing Systems 25. Curran Associates, Inc., pp 1097–1105.

212. Andermatt S, Pezold S, Cattin P (2016) *Multi-dimensional Gated Recurrent Units for the Segmentation of Biomedical 3D-Data BT - Deep Learning and Data Labeling for Medical Applications.* First International Workshop, LABELS 2016, and Second International Workshop, DLMIA 2016, Held in Conjunction with MICCAI 2016, Athens, Greece, October 21, 2016, Proceedings. In: Carneiro G, Mateus D, Peter L, et al (eds). Springer International Publishing, Cham, pp 142–151.

Acknowledgments

Finally, the ultimate chapter of my PhD Thesis – the acknowledgments to my colleagues, friends, and family for their continuous support, and without whom my studies and PhD would not have been possible.

First, I would like to thank my supervisor Prof. Oliver Bieri for giving me the unique opportunity to work in his group on an exciting subject such as lung MRI. Oliver was every time confident and open-minded to my ideas, and always had time for discussion, constructive criticisms, and he had endless patience. I will always remember being very impressed by the many detailed and meticulous comments on my first paper drafts. His supervision, knowledge, clever proposals, and guiding suggestions were fundamental for my projects. Also his mountaineering recommendations and life advice have been precious to me. Thank you, Oliver!

I am much grateful to Prof. Matthias Stuber to be my thesis co-examiner and for evaluating my work. I owe my gratitude also to my faculty representative Prof. Bernd Krusche, enabling me to fulfill my thesis at the Faculty of Science, University of Basel.

I would like to acknowledge all the help, the effort, the support, and the advice that Dr. Grzegorz Bauman has provided for me throughout the whole duration of my PhD studies: his assistance, supervision, and experience in the field of lung MRI were extremely valuable. I owe much of the success of my PhD to Grzegorz, and I am very grateful to him: we had fun while collaborating and investigating novel lung MR methodologies, and moreover, we became good colleagues, friends, and even diving buddies. A great MR “lung” team! Thanks a lot, Grzegorz!

I am also much thankful to Dr. Francesco Santini for the thousands of explanations (so many!) he gave me during our meetings, and for his continuous guidance during my PhD studies. Francesco always had time for me, inside or outside the office, to encourage me or to cheer me up; he became a good friend. Thank you, Francesco!

A special thanks also to Dr. Rahel Heule for her insightful critiques to my manuscripts, for carefully double checking my equations and for the several MR experiments late in the night. I am much indebted to her: her help was invaluable, crucial, and of importance for my research. I also have to thank her for her optimistic heart, encouragements, for bringing me out of the office and making me enjoy life. Thank you very much, Rahel!

I would like to thank Dr. Xeni Deligianni for her assistance with statistical analysis and her sunny-natured presence in the office. I will always remember small and friendly gestures such as offering breakfast, coffee-filled chocolates, or an invitation to get a real powerful Italian / Greek coffee. Thank you Xeni for being so nice!

I am much grateful to Damien Nguyen who always invested time to fix computer-related issues. I will never forget, once, as a joke and without telling me, Damien had hacked my laptop: as a result, the words that he was typing on his computer were transformed on my laptop into a robotic voice, which I could hear through my headphones. For a moment, I thought aliens contacted me or that my artificial intelligence algorithms took possession of my computer. Damien was, of course, rolling on the floor laughing (…). Beside the pranks, Damien was really supportive during my PhD studies, and together we had much fun, especially while freeriding in our Swiss Alps. Thank you, Damien, for all the powder-snow we got and all your help!

I would also like to thank Dr. Matthias Weigel for the multitude of fruitful discussions we had about MR sequences and physics, sometimes while eating fabulous Indian dinners or simple pizzas. He also encouraged my passion for office-gardening and nature. Thank you, Matthias!

I am much grateful to Dr. Markus Klarhöfer who provided many work-in-process MR sequences and know-how, as well as several exquisite breakfasts at the office. Furthermore, he organized some high-level dinners at the conferences (…). Thank you, Markus!

I would like to express my gratitude to Tanja Haas for the long time she spent at the scanner with me, the MR imaging tricks that she taught, and all the data processing. I also had some awesome freeride skiing adventures with her. Thank you, Tanja!

I would like to thank Philipp Madörin for all the post-processing and coding. His assistance with data segmentation was relevant for some projects. Thank you, Philipp!

I am very grateful for the effort on study ethics and bureaucratic work of Dr. Seline Schellenberg and Dr. Sabine Tanner. Thank you, Seline and Sabine!

I would like to thank Dr. Gregor Sommer for the excellent collaboration, the many medical explanations, and for pushing our lung MRI studies into the clinics. Thank you, Gregor!

I owe my gratitude to Prof. Philipp Latzin and Dr. Sylvia Nyilas for the fruitful collaboration. They were enthusiastic to hear about our new methodological MR techniques, and always willing to

explain some pulmonary physiological processes, or to propose new clinical studies. Furthermore, their clinical know-how and constructive critics to my writing was very much appreciated. Thank you, Philipp and Sylvia!

I would like to acknowledge the assistance of Prof. Philippe Cattin, Robin Sandkühler, Simon Andermatt, Dr. Simon Pezold, and Dr. Christoph Jud with image registration and deep learning algorithms. Thank you all!

I am very grateful to Dr. Mark Wielpütz and Prof. Claus Heussel for their aid, assistance, and great cooperation. Thank you, Mark and Claus!

I would like to further extend my acknowledgments to physicians and physicists that collaborated and supported me during my PhD studies: Prof. Jens Bremerich, Dr. Nicolin Hainc, Dr. Monika Gloor, Dr. Zarko Celicanin, Dr. Claudia Lenz, Dr. Claudia Weidensteiner, Dr. Michael Amann, Dr. Julia Reinhard, Dr. Bram Stieltjes, Dr. Florian Singer, Dr. Enno Stranzinger, Dr. Dr. Michael Ith, Dr. Bernd Jung, Dr. Mark Wiese, Prof. Didier Lardinois, Prof. Michael Tamm, and Prof. Urs Frey. Thanks to everyone!

In general, thanks to all the colleagues of the radiological physics group for the good atmosphere at the office and the lovely times we had.

I appreciated the hospitality and cordiality of the whole radiology department (medical doctors, MTRA, administrative staff) at the University Hospital Basel. Thank you all!

I am much grateful to the Swiss National Science Foundation (SNF) for the financial support.

Finally, I would like to thank all my friends (and colleagues) for reminding me that there is a life beyond research. They always supported me, and brought me back from my science-related thoughts to the planet earth (if possible). Thank you for the amazing moments!

Last but not least, I would like to thank my whole family, my parents, and my brother with all my heart. They gave me the occasion to grow up in a stimulating environment. They showed unconditional interest and enthusiasm in what I was doing, and they were always there to help me. Without them, I would not be the person who I am, and my academic results, as well as this work, would not have ever been possible! Thank you, my family!

Curriculum Vitae

Personal Data

Name:	Orso Andrea Pusterla
Date of birth:	February 13, 1987
Place of birth:	Lugano, TI
Place of citizenship:	Breggia, TI

Education

Mar. 2014 – May 2018	PhD in Biophysics, University of Basel. Supervisors Prof. Dr. Oliver Bieri and Prof. Dr. Bernd Krusche. Thesis title: *Functional pulmonary MRI with ultra-fast steady-state free precession*.
Sept. 2011 – Sept. 2013	Master of Science in Physics, ETH Zürich. Master's thesis in Medical Physics, supervisors Prof. Dr. Marco Stampanoni and PD Dr. Michael Fix. Thesis title: *Accounting for the Multi Leaf Collimator (MLC) impact in a beamlet based Direct Aperture Optimization (DAO) for modulated electron radiotherapy*.
Sept. 2007 – Sept. 2011	Bachelor of Science in Physics, ETH Zürich. Bachelor thesis in Particle Physics, supervisor Prof. Dr. Christoph Grab. Thesis Title: *Electron-positron annihilation: measuring the picoseconds positronium's lifetime in air*.